Dynamic transcoding properties of NF-κB signaling

by

Chaitanya Sudhir Mokashi

B.Tech., Indian Institute of Technology Bombay, 2015

Submitted to the Graduate Faculty of the

School of Medicine in partial fulfillment

of the requirements for the degree of

Doctor of Philosophy

University of Pittsburgh

2022

UNIVERSITY OF PITTSBURGH

SCHOOL OF MEDICINE

This dissertation was presented

by

Chaitanya Sudhir Mokashi

It was defended on

July 20, 2022

and approved by

S. Chakra Chennubhotla, PhD, Associate Professor, Department of Computational and Systems Biology, University of Pittsburgh

James R. Faeder, PhD, Associate Professor, Department of Computational and Systems Biology, University of Pittsburgh

Philip R. LeDuc, PhD, William J. Brown Professor, Department of Mechanical Engineering, Carnegie Mellon University

Zachary Z. Freyberg, PhD, Assistant Professor, Department of Psychiatry, University of Pittsburgh

Dissertation Director: Robin E.C. Lee, PhD, Associate Professor, Department of Computational and System Biology, University of Pittsburgh

Dynamic transcoding properties of NF-κB signaling

Chaitanya Sudhir Mokashi, PhD

University of Pittsburgh, 2022

All biological systems constantly receive, process and respond to external signals. Cells, although being the basic unit of life, show remarkable ability to decipher the environmental cues and produce appropriate responses. This signal transduction is achieved by intricate cascades of signaling molecules which carry out the calculations needed to encode, process, decode and transfer (i.e. 'transcode') the external signals to responses such as various cell fate decisions. Dysregulation of cellular signal transduction is therefore the underlying cause of many diseases.

As it happens in real-time, the dynamics of both signals and the processing machinery play a crucial role in signal transduction. Microfluidic systems enable probing of signal transduction with dynamic stimuli but remain largely inaccessible. Particularly, such ability could prove useful in studying the signal processing in the NF-κB pathway, dynamics of which is pertinent to many disease pathologies. Computational approaches such as statistical and mechanistic modeling could help in formalizing the signal processing mechanisms and making useful predictions.

The overarching theme of this dissertation is to study the signal processing and control mechanisms used by cells in the context of the NF-κB signaling pathway. This includes the mechanisms and functions of specific parts of the pathway as well as their dynamics, and how they fit together to achieve the final response output. First, we develop an accessible microfluidic system to study the cellular responses to dynamic stimuli. Second, we characterize the encoding and decoding of cytokine signals in the NF-κB pathway. Third, we alter the signal encoding by leveraging the microfluidic system to maximize NF-κB responses. Finally, we consolidate our findings and put forward a framework for a comprehensive model of the NF-κB pathway.

Keywords: cell signaling, microfluidics, NF-κB pathway, computational modeling, dynamic stimulation, stochastic pooling.

Table of Contents

List of Tables

List of Figures

Preface

I would first like to thank my adviser Dr. Robin Lee, without whose constant guidance and support this dissertation would not have been possible. I had the opportunity to learn many skills from him, scientific, communication, problem-solving and many more, that will be greatly helpful in my future career. His approach of learning from and leveraging many diverse fields in pursuit of scientific discovery and innovation has markedly shaped me as a scientist. His mentorship will have a lasting impact on all my future endeavors.

My current and former lab mates have been immensely helpful throughout my PhD journey and without their help this dissertation would not have taken shape as it is today. I would like to especially thank David Schipper, Gabriel Kowalczyk, Steven Smeal, Dr Yue Guo, Dr J. Agustin Cruz and Dr Sanjana Gupta for their help, friendship and many interesting conversations and discussions, scientific and otherwise. I am lucky to have worked with you all over these years.

I would like to thank my committee members, Dr Chennubhotla, Dr Faeder, Dr LeDuc and Dr Freyberg, for their continuous guidance and helpful suggestions throughout my PhD work. I would additionally like to thank Dr Freyberg for giving me an opportunity to contribute to another interesting project which is not part of this dissertation. I would also like to thank many current and former students of the CPCB program for their friendship over the years. Especially, I would like to thank Jonathan King, Jennifer Williams, Dr Easwaran Ramamurthy, Dr Raghavendran Partha, Dr Bentley Wingert, Dr Cihan Kaya, Dr Michael Kleyman and Dr Marta Wells for helpful scientific and career discussions. I would also like to thank our CPCB program administrators, Kelly Gentille and Nancy Linderman, for their constant help that made my PhD experience much smoother.

No personal endeavor can be successful without support from friends and I am lucky have many! First, I would like to thank my Pittsburgh-friends: Saif Rahman, Kunal Aggarwal, Pratik Khandagale, Parul Chauhan, Deepak Dilipkumar, Pranay Mohanty, Kshitij Deshmukh, Shruti Nanivadekar, Devdeep Ray, Eyan Noronha, Bhagyashree Lele, Swapnil Keshari, and many more; due to their friendship my last few years in Pittsburgh were wonderful and fabulous! Next, I would like to thank all my undergraduate friends from IITB, especially the MKD juntaa, who will always have a special place in my life. I would also like to thank my school friend Pratik Aghor for his friendship, and for great scientific and philosophical discussions over the last many years.

Finally, I would like to convey my biggest thanks to my family, especially my parents, Dr Sudhir Mokashi and Dr Anuradha Mokashi, and my brother Shriniwas Mokashi. You have made innumerable sacrifices over the years to support me and your love and caring has helped me survive the worst of times. This dissertation is dedicated to you!

1.0 Introduction

1.1 Use of microfluidics to control the cellular microenvironment

A cell is constantly exposed to myriad of signaling molecules such as growth factors, cytokines, hormones and neurotransmitters which activate dynamic signal transduction pathways within the cell that govern pivotal cell fate decisions [1-6]. These pathways play a crucial part in cell functionality and viability, and their deregulation leads to various diseases [7-9]. Although cellular signaling has been studied for many decades, there is a major disconnect between *in vitro* experiments and *in vivo* activity of cells. Most experiments characterize these pathways with persistent stimulation with signaling molecules. Whereas in vivo, the cellular microenvironment is dynamic and the stimulation is often transient and time-varying, response to which may be different and more relevant [2, 10-13]. The ability to precisely control the dynamic cellular microenvironment is, therefore, necessary to study the capabilities and identify the control mechanisms of signaling pathways.

Microfluidic devices alleviate these challenges by enabling control of cellular microenvironment [14, 15]. Several microfluidic devices and control systems have been developed to broadly provide this ability [14, 16-22]. Typically, a microfluidic device consists of a Polydimethylsiloxane (PDMS) based structure with etched micrometer-scale features bonded with a glass cover slip. The features on the device serve various functionalities such as channels to allow the flow of culture media, chambers to trap and grow cells, and modules that can mix and dilute different treatments. The device can have several inlets and outlets that connect it to an external pressure or flow modulating system. Once cells are loaded in such devices, the flow of

media in the device is controlled by changing inlet and outlet pressures or flow rates. Depending on the device architecture and the pressure and flow manipulation, user-defined temporal patterns of stimuli can be presented in the cell containing chambers. Cellular responses to such stimuli can either be measured with a microscope or the cells can be harvested for other readouts like gene expression and protein abundance [23]. See methods section of chapter 2 of this dissertation for more details about design, fabrication and operation of a custom microfluidic device.

The features and architecture of microfluidic devices are designed in computer-aided design (CAD) software such as Autodesk and SolidWorks. The design is then realized in the form of a mold that can act as a negative relief to PDMS. The molds are typically fabricated using photo lithography but many other techniques such as soft and stereo lithography can also be used [24]. PDMS mixed with its hardening agent is poured on the fabricated molds so that the features on the mold get etched on the solidified PDMS structure. Methods to control fluid flow in microfluidic devices range from simple pneumatic switches to precision pressure or flow control systems such as syringe and peristaltic pumps. The pressure or flow through these systems is controlled by custom or commercially available software.

Although microfluidic devices and corresponding control systems can be useful in probing cellular responses in complex microenvironments, there are a few limitations in their widespread adoption in terms of cost, expertise and utility. The photolithographic microfabrication along with the pressure and flow control systems, and their operating software, are expensive. Additionally, the design, fabrication and operation of microfluidic devices requires specialized expertise. Furthermore, the existing microfluidic systems may not provide all the desired functionalities, such as high dynamic range and ability to control multiple stimuli. Because of these challenges, use of microfluidics remains limited to a few labs with relevant resources and expertise.

In chapter 2, we report the development of a cost-effective and accessible microfluidic dynamic stimulation system using stereolithographic 3D printing and gravity-driven flow. We demonstrate its functionality by quantifying the responses of the signaling pathways as described in the following section, to ramp stimuli of cytokine concentration. In chapters 3 and 4, we further use this system to expose cells with dynamic stimuli such as single and repeat pulses to characterize the dynamics of network components and to demonstrate how dynamic stimuli can maximize the signaling pathway responses.

1.2 The NF-κB signaling pathway and its dynamics

The NF-κB (nuclear factor kappa-light-chain-enhancer of activated B cells) is a transcription factor complex involved in inflammatory signaling and is implicated in many disease pathologies including cancer [7, 25, 26]. In a resting cell, NF-κB is sequestered in the cytoplasm by its inhibitor proteins IκB (Inhibitors of κB), by masking the nuclear localization signals (NLS) of the NF-κB proteins [27, 28]. When cells are stimulated with cytokines such as Tumor Necrosis Factor α (TNFα) or Interleukin-1 β (IL-1β), the cytokine ligands bind with their corresponding receptors on plasma membrane [29, 30]. The bound receptors initiate recruitment of adapter proteins resulting in formation of a multi-protein signaling complex [30-33]. In the canonical branch of the NF-κB pathway, which is the focus of this dissertation, such signaling complexes initiate Ubiquitin polymerization resulting in large scaffold-like structures containing linear, branched or mixed Ubiquitin chains [34-36]. The NF-κB essential modulator (NEMO or IKKγ) protein then binds to the Ubiquitin scaffolds through its Ubiquitin binding domain [36, 37]. NEMO can interact with two other kinase proteins called IκB kinase α and β (IKKα and IKKβ) [38]. The

protein complex consisting of NEMO along with the kinase subunits IKKα and IKKβ is called the IKK complex. When multiple such IKK complexes are recruited to the Ubiquitin scaffolds, the IKK kinase subunits get activated by phosphorylation due to induced proximity [38, 39]. The activated IKK kinases then phosphorylate IκB proteins which tags them for degradation, thereby unmasking the NLS of NF-κB proteins [25]. The free NF-κB proteins then translocate to the nucleus where they act as transcription factors by binding to DNA at the corresponding κB sequence motifs and activating the corresponding genes [40-42]. The target genes of NF-κB fall in a wide functional range including control of cell survival, division, and proliferation; secretion of signaling molecules; and apoptosis and cell death [43].

Among the target genes of NF-κB are the inhibitor IκB proteins [27, 44]. Therefore, the pathway activation also induces a negative feedback via the newly produced IκB, which binds to the NF-κB in the nucleus and sequesters it back in the cytoplasm. Another key target gene of NF-κB is a gene that encodes the deubiquitinating enzyme A20 (or TNFAIP3) [10, 42]. The NF-κB induced A20 promotes destabilization of the Ubiquitin scaffolds which reduces the IKK complex recruitment and thereby prevents further signal propagation [45]. Due to this two-phased negative feedback, cellular responses in terms of nuclear localization of NF-κB show highly dynamic and pulsatile behavior with initial rapid increase followed by slower adaptation [10]. Depending on the cell type and molecular composition, the response can show full adaptation after first pulse [2, 46], or multiple pulses with varying amplitudes and durations [23, 47].

The dynamics of NF-κB response plays a crucial role in the regulation of the target genes and corresponding cell fate decisions [48]. Various dynamic features such as pulse number, frequency, and fold change detection have been reported to control the target gene expression [10, 42, 49, 50]. Depending on the NF-κB response dynamics, the pathway can drive expression of

early, intermediate or late responding genes [10, 42, 47]. The NF-κB dynamics is also known to encode and transmit most information about the extracellular environment such as cytokine concentration [51-53]. It therefore becomes important to identify and characterize the dynamics of key nodes in the NF-κB signaling network that control the pathway dynamics.

The dynamics of NF-κB nuclear translocation is typically studied using live-cell microscopy [46, 54]. A fluorescent protein (FP) fused with NF-κB is expressed in cells either by overexpression [42] or expression through endogenous locus [54]. The cells are imaged using the appropriate wavelength filters and fluorescence intensity of such protein is measured as a readout of its spatial abundance. The dynamics of nuclear translocation of FP-fused NF-κB can therefore be quantified by measuring the nuclear intensity in a cell over time in response to stimuli. Cell segmentation and tracking tools are often used to automate collection of such single-cell response data [55].

Variability and heterogeneity are common properties of biological systems [56] and the NF-κB pathway is no exception. Even genetically identical cells can produce substantially different NF-κB responses to identical stimuli [46, 52]. Many factors, such as intrinsic noise in gene expression, protein abundances, and cell cycle state contribute to the cell-to-cell variability [57, 58]. Such variability affects the ability of cells to correctly decode the information about the microenvironment [51, 52]. As dysregulation of the NF-κB pathway is implicated in many diseases, considering and quantifying the variability among cells is imperative to the design of optimal treatment strategies to manipulate cell responses.

Although the NF-κB pathway has been widely studied over the past decades, several key unanswered questions remain regarding its signing mechanisms. As alluded in the previous section, the cellular microenvironment is highly dynamic and the NF-κB pathway responses to

such dynamic stimuli are still not well understood. Furthermore, although interactions of several nodes in the NF-κB signaling network has been characterized, the mechanisms of many key nodes, such as the transmembrane receptors and the corresponding cytoplasmic signaling complexes (e.g. the IKK complex), still remains unknown. Due to its dynamics and complexity, mechanistic modeling approaches (as further described in the following section) are highly valuable for delineating mechanisms and making predictions in the context of the NF-κB pathway. Due to lack of knowledge about key mechanisms in the pathway, such models are either specific to some pathway components or make assumptions and abstractions about the unknown mechanisms. A comprehensive model of the NF-κB pathway could therefore be highly useful in consolidating the current knowledge of the field, and to make effective predictions.

In chapter 2, we show how time-varying stimuli can produce atypical NF-κB responses and that such responses can be explained by variability in the rates of negative feedback. In chapter 3, we characterize the dynamics of the IKK complex in response to cytokine stimuli and reveal how it mediates the downstream NF-κB response. We also propose a novel mechanism of IKK activation, called a Variable-Gain Stochastic Pooling Network (VG-SPN). In chapter 4, we further characterize the NF-κB responses to dynamic stimuli and demonstrate how repeat pulse stimulations increase the pathway response compared to a bolus. We finally put forth a framework for a comprehensive mechanistic model of the NF-κB pathway.

1.3 Mechanistic modeling and its applications to study the NF-κB signaling pathway

Cells, as the fundamental units of life [59], constantly interact with their environment and communicate with other cells in order to function effectively in complex multicellular organisms

[60, 61]. Dysregulation of this signaling ability of cells is the underlying cause of many diseases [61, 62] and therefore increased understanding of cellular signaling is needed to develop better treatment strategies [63]. Cellular signaling pathways usually involve intricate networks of interacting molecules making them complex and nonlinear [64]. Cellular signaling is therefore usually studied with the lens of Systems Biology, a discipline that studies the behavior of complex biological systems by considering the many interactions between system components [65]. Systems Biology approaches enable mathematical representations of the interacting molecules and allow us to build computational models of signaling pathways [66, 67].

Computational models of signaling pathways can be either statistical or mechanistic in nature. Statistical models characterize the input-output relationships in the biological data whereas mechanistic models involve explicit mechanisms of biological interactions [68-71]. While we use both statistical and mechanistic modeling techniques in this dissertation, our focus is on mechanistic modeling as it allows better representation of known and hypothesized biological mechanisms and the dynamical nature of the available data. A mechanistic model typically consists of Ordinary Differential Equations (ODEs) for each molecule in the signaling network. The ODEs describe the evolution of the corresponding molecules over time depending upon the rates of reactions that the molecules are involved in [72]. Such ODE models are associated with several parameters such as rate constants of reactions and the initial abundances of the molecules. Numerical values of such parameters need to be estimated in order to 'fit' the mechanistic model to the biological data. While several techniques exist to determine the optimal parameters that fit the model to the data, parameter estimation remains a key challenge for large mechanistic models with limited data availability [73, 74].

Mechanistic modeling is particularly useful in the context of NF-κB signaling pathway as it allows characterization and prediction of NF-κB response dynamics, which is crucial for cell fate decisions as alluded to in the previous section. Since its discovery, many mechanistic models have been developed for the NF-κB pathway [67, 75]. Some of these models were specifically developed to study particular modules of the pathway, such as the feedback mediated by IκB proteins [27, 28, 76]. Some models are more general and contain many of the relevant molecules and interactions while making a few abstractions and assumptions [77, 78]. Some models introduce stochasticity in order to account for the heterogeneity in single-cell NF-κB responses [23, 47, 79]. In this dissertation we build upon the mechanistic model first developed by Ashall et al [40] called the 'Deterministic Two Feedback' or D2F model. This model was developed with the two-pronged IκB and A20 mediated negative feedback to characterize the dynamics of pathway in response to repeat pulse stimuli. REC Lee et al [42] modified this model to include the effects of competition on NF-κB mediated gene expression and proposed a revised 'Deterministic Two Feedback with Competition' or D2FC model. We use the D2FC model in this dissertation as baseline and modify it according to the available experimental data.

In chapter 2, we use to D2FC model to show how heterogeneity in negative feedback rates can give rise to atypical patterns of NF-κB responses. In chapter 3, we develop a statistical and stochastic model, called VG-SPN, of IKK activation by cytokine stimuli. Finally, in chapter 4, we consolidate our models and findings in chapter 2 and 3 and put forward a framework of the comprehensive mechanistic model of the NF-κB pathway and present preliminary results.

1.4 Dissertation goals

Overall this dissertation presents several experimental and computational approaches to probe the signaling dynamics of the NF-κB pathway. In chapter 2, we present a low-cost and accessible microfluidic system to generate dynamic stimuli in cellular microenvironments. In chapter 3, we characterize the cytokine mediated activation of the IKK complex and its relationship with the downstream NF-κB response, and propose a novel signaling motif called Variable-Gain Stochastic Pooling Network. In chapter 4, we demonstrate that dynamic stimuli, such as repeat pulses of cytokines, can maximize the NF-κB response and put forward a framework for a comprehensive model of the NF-κB pathway. Finally, in chapter 5, we summarize our conclusions and suggest future steps that could be taken to build upon this dissertation work.

The work presented in chapters 2 and 3 has been published in articles [46] and [54] respectively. The work in chapter 4 is still ongoing and will be continued by other members of the Lee lab. Additional graduate work regarding bioinformatic analyses of the Wnt signaling pathway, not included in this dissertation, is published in article [80].

2.0 Development of a microfluidic dynamic stimulation platform to probe cellular signaling

This chapter is taken from **Mokashi CS***, Schipper DL*, Qasaimeh MA & Lee REC. "A system for analog control of cell culture dynamics to reveal capabilities of signaling networks", iScience, 2019, *co-first authors [46]. Details of author contributions can be found in Section 2.5.

2.1 Introduction

The microenvironment of a cell is multifarious, with a constantly changing composition of extracellular molecules. When cells are exposed to extracellular cues, such as changes in the concentration of inflammatory cytokines or drugs, they activate dynamic signal transduction pathways within the cell that govern pivotal cell fate decisions [1-6]. Although deregulation of these pathways contributes to human disease, most experiments characterize cells exposed to constant stimulation which contrast the transient and time-varying properties of cues *in vivo*.

Biomedical micro-electro-mechanical systems such as microfluidic devices broadly enable studies of cell behavior in precisely controlled microenvironments [14, 16]. Microfluidic flow systems that operate by switching between multiple inlets, each with discrete concentrations or different stimuli, can generate time-varying changes of medium composition in a cell culture [17, 21, 81-84]. However, due to their digital design, switch-based approaches often have limited operating ranges (usually under 10-fold dynamic range of concentration dilutions) and rely on specialized expertise and equipment to make and use. Other approaches that dilute fluids between reservoir pairs to alter the composition of a cell culture medium [85, 86] require high precision

flow control systems that are not available in most biology labs. Because of these challenges, signal transduction networks are rarely investigated in the context of dynamic microenvironments.

We set out to address these challenges by first developing a minimal dynamic stimulation system that provides time-varying control over cell culture composition and then we establish proof-of-concept by using the system with in live-cell imaging experiments. The modular dynamic stimulation system consists of a gravity pump controller, which can be built from commonly available low-cost parts, to coordinate gravity-driven flow [2] and laminar fluid streams in a cell culture device [18, 19, 87]. Cell culture devices under control of the gravity pump are assembled from 3D-printed molds and can be interchanged to provide different functions. By automating flow rates in the cell culture device, the system provides independent control over time-varying concentrations for multiple stimuli over a broad dynamic range. To demonstrate use of the system, we compare activation of the NF-κB signaling pathway in live cells exposed to tumor necrosis factor (TNF) either as a step up to a continuous concentration or as a slow ramp of increasing concentration. Although the characteristic response of the NF-κB pathway is adaptive, we find alternative patterns of pathway activation when cells are exposed to a TNF ramp. We also find pathway activation is greater in response to ramp stimuli even though cells are exposed to significantly less TNF over the duration of the experiment. Using computational models, we show that cell-to-cell variability for negative feedback within the NF-κB signaling network explain observed patterns of nuclear NF-κB dynamics in response to step and ramp stimuli. Our results demonstrate that dynamic stimulation can be achieved under gravity-controlled flow and can be used to reveal hidden capabilities of signal transduction networks.

2.2 Results

2.2.1 Development of a dynamic stimulation system for live-cell imaging

We designed a microfluidic dynamic stimulation device with architectural features in the order of 10's of microns or larger to be compatible with resolutions of common stereolithography 3D printers (Figure A1). When used as a negative relief for PDMS device fabrication, 3D-printed molds circumvent the need for specialized photolithography and microfabrication facilities [88] and allow for high aspect ratio integrated devices that are otherwise very challenging to fabricate [89]. The device design consists of three control inlets (I1, I2, and I3), cell seeding ports (SP1 and SP2), a mixer region, a cell culture channel, and an outlet (Figure 1A). Continuous flow is established when fluid-containing reservoirs (R1, R2, and R3) are attached via tubing to the device, and at least one of the inlet reservoirs is positioned above the outlet. Flow rates from each of R1, R2, and R3 are controlled by moving their vertical positions with respect to each other and the outlet.

Taking advantage of variable microchannel heights that can be produced by 3D printing, we designed a raised micro-mixing channel downstream of I1 and I2 and before the cell culture channel (Figure 2.1 A, inset), which would permit efficient diffusive mixing between the two streams. Downstream of the mixer, we found that fluorescence from Alexa488-conjugated BSA added to cell culture medium in R1 was diluted by non-fluorescent 'Medium only' from R2 with a homogenous spatial distribution that indicates efficient mixing (Figures 2.1 B and A2). Differences between combined driving pressures from reservoirs R1 and R2 and that from reservoir R3 are used to move the laminar interface position (LP) of the mixer stream within the cell culture channel. The cell culture channel can be divided into distinct parallel bands of user-

defined width along the direction of flow (Figure 2.1 B). In the default reservoir operating position (Figure 2.1 B, left), a narrow band of the cell culture channel is continuously exposed to the output from the mixer (M) and the rest of the channel is exposed to 'Medium only'. During the experiment, the LP of the mixer stream is moved to include the experimental band (E) of the channel, leaving a negative 'Control' (C) that is exposed to 'Medium only' throughout the experiment (Figure 2.1 B, middle and right). During the experiment, the volume fraction (Xc), which establishes the concentration of the solute flowing from R1 over the 'E' and 'M' bands of the device, is determined by the relative positions of R1 and R2.

To reliably control flow rates from R1, R2, and R3, we developed a gravity pump consisting of an assembly of eight vertically-oriented stepper motors attached to a chassis (Figure 2.1 C). Each stepper motor is individually addressed by an Arduino microcontroller and rapidly controls the height of reservoir platforms (Figure 2.1 C). When R1, R2, R3, in addition to an outlet reservoir are attached to the platforms and connected to the dynamic stimulation device, relative changes between heights of inlet reservoirs can be used to alter their respective flow rates into the cell culture device.

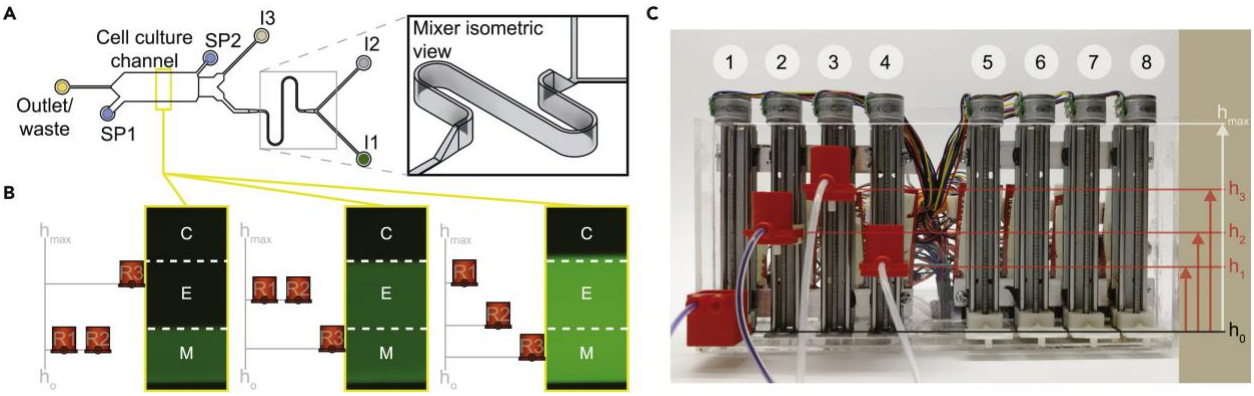

Figure 2.1 Gravity Pump and Cell Culture Chamber for Dynamic Stimulation

(A) Top view of the dynamic stimulation device with three inlets (I1, I2, I3), two cell-seeding ports (SP1 and SP2), and an outlet. Inlets I1 and I2 are followed by a raised mixer (inset) that dilutes stimulus to desired concentrations according to flow rates from I1 and I2. I3 controls the laminar interface position (LP) of the experimental band in the cell culture channel. Cells are seeded from SP2 into the cell culture channel and observed by time-lapse imaging. See also Figure A1. (B) Flow rates through the inlets (I1, I2 and I3) are controlled by hydrostatic pressure differences between corresponding reservoirs (R1, R2, and R3) and the outlet. In the default position (left), R3 is positioned higher such that the stimulus from the mixer is confined only to the mixer band ("M"). During experiment (center and right), R1 and R2 are positioned higher to move the LP over the experimental band ("E"). Volume fraction (Xc) of stimulus in the experimental band is determined by the relative positions of R1 and R2. Control band ("C") is not exposed to stimulus during the experiment. (C) The "gravity pump" consists of eight vertically mounted stepper motors with screw-nut platforms and an Arduino microcontroller to control platform heights; 3D printed reservoirs on platforms 1–4 are connected to corresponding inlets via tubing. Differences between inlet (h1, h2, and h3) and outlet (h0) reservoir heights determine the hydrostatic driving pressure at each inlet.

2.2.2 Gravity-driven control and modularity of the dynamic stimulation system

A physical model of the system was calibrated to experiments and used to determine Xc and LP in the device for combinations of reservoir positions (Figure 1C; heights h1, h2, and h3).

Using Alexa488-conjugated BSA in reservoir R1 and fluorescent tracer beads suspended in medium in all inlet reservoirs, we found that Xc and the volume flow rate (Qc) in the cell culture region can be independently varied (Figure S2). Qc was set ($Qc = 5 \times 10^{-11}\ m^3/s$) such that shear stress on cells is constant (< 0.05 Pa, based on simulations) throughout subsequent experiments. Cells grown in the dynamic stimulation system therefore experience shear forces that are orders of magnitude smaller than endothelial cells in vasculature [90] and do not activate shear stress response signaling via mechanotransduction [2, 91].

In principle, the system is fully analog and capable of producing arbitrarily complex patterns of stimulation in the 'E' band of the cell culture channel. By adding Alexa488-conjugated BSA in reservoir R1 as a surrogate for dilution of a stimulus, we set out to demonstrate basic capabilities of the system. In the first experiments (left-side graphs of Figure 2.2 A and B) we used the system to generate sharp laminar pulses of varied duration or concentration. By defining the time varying functions of Xc and LP at a fixed flow rate, the calibrated model generated time-varying profiles for h1, h2, and h3 (Figure 2.2 A, bottom left). The predicted experimental profile (Figure 2.2 A, green panel) agreed strongly with the fluorescence time course measured in the device (Figure 2.2 B). Next, we used the system to generate linear and exponential ramps in concentration with a fixed Qc and LP. Although in extreme positions for h1 and h2 we occasionally observed cross-flow between the channels connecting I1 and I2 to the mixer, the system robustly produced linear and exponential ramps between Xc= 0.05 and Xc = 1.0 (Figure 2.2 A and B, right side), a 20-fold dynamic range. Our results show that hydrostatic pressures achieved with the gravity pump are sufficient to precisely control the dynamics of medium composition in the cell culture channel.

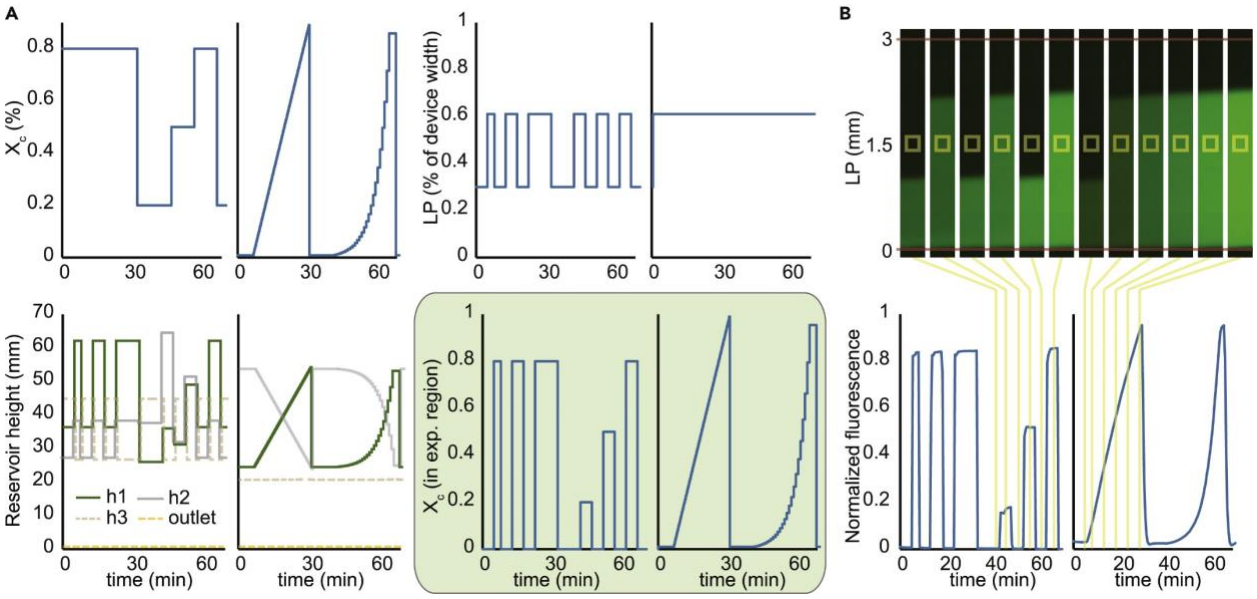

Figure 2.2 Gravity Pump and Cell Culture Chamber for Dynamic Stimulation

(A) Experiments are user defined by temporal profiles of volume fraction of cytokine (Xc; top left), laminar position (LP; top right), and flow rate (Qc; set to a constant value of Qc = 5 × 10−11 m3/s throughout each experiment). Using a physical model, the user-defined profiles for Xc, LP, and Qc are converted to time-varying reservoir heights (bottom left). Temporal profiles for reservoir heights are loaded on the gravity pump and run during the experiment. Green panel (bottom right) shows the predicted time-varying profile for Xc in the "E" band of the dynamic stimulation device. (B) Fluorescence intensity of Alexa 448-conjugated BSA (top) measured across the cell culture channel (yellow box in Figure 1A). Observed fluorescence in the "E" band matches predicted Xc within 5% error (bottom).

Modifications to the system or the architecture of the cell culture device can provide additional functionality. For example, the stable range of dilutions can be further increased by incorporating inexpensive capillary resistors [92] to precisely limit flow in the tubing upstream of the device and prevent cross-flow at even lower Xc values. Similarly, altering architectural

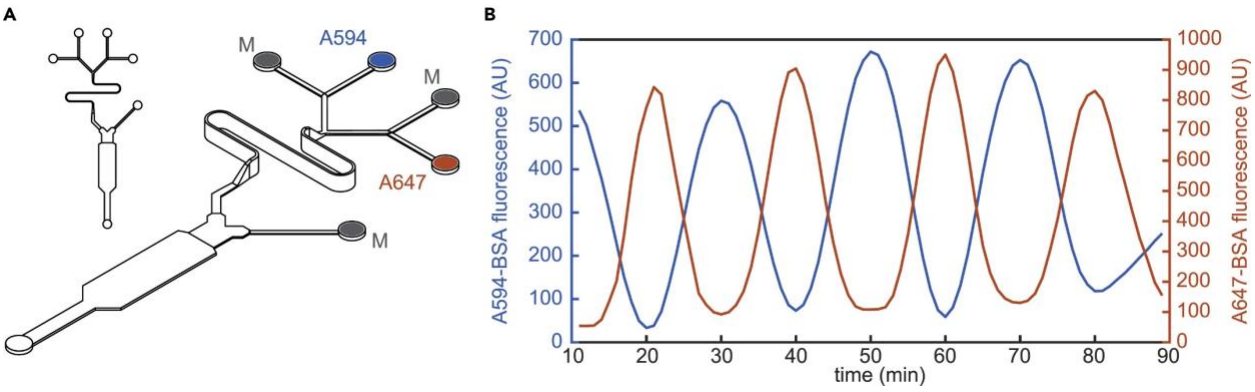

Figure 2.3 Modularity of the Dynamic Stimulation System

(A) A variant device with four inlets to the mixer for simultaneous control of multiple distinct stimuli. Each inlet is connected to reservoirs containing growth medium or different stimuli. (B) Example experiment using reservoirs with Alexa 594- and Alexa 647-conjugated BSA (A594 or A647, respectively, in A) connected to two of the mixer inlets. The other inlets are connected to reservoirs with Medium only (M). Resulting fluorescence measured at the same point in the "E" band of the cell culture device shows that out-of-phase oscillations can be achieved.

properties of the device by adding additional inlet channels to the mixer (Figure 2.3 A) broadens the stable operating range of Xc multiplicatively by over 20-fold per inlet. Theoretically, a mixer with three inlets should be stable over a 400-fold dynamic range ($0.0025 \leq Xc \leq 1.0$), and 8000-fold for a mixer with 4 inlets. Alternatively, by taking advantage of several inlets to the mixer, independent control of time-varying profiles for multiple stimuli can be achieved in a single device (Figure 2.3 A and B). For a given experiment, the cell culture device attached to the gravity pump can be selected to provide stable control over a specific range of operating conditions or to address biological questions with increased complexity.

2.2.3 Ramp stimulation reveals distinct modes of NF-κB pathway activation

The acute inflammatory response to injury and infectious agents is dynamic. Time-varying expression of pro-inflammatory and anti-inflammatory cytokines from infiltrating leukocytes, macrophages, T-cells, in addition to tissue-resident cells, determine whether inflammatory conditions are resolved and can lead to disease or sepsis when deregulated [93-95]. At the cellular level, inflammatory cytokines such as TNF induce translocation of the NF-κB transcription factor from the cytoplasm into the nucleus, encoding a dynamic master signal for transcription of gene families [2, 42, 50, 96]. When in the nucleus, NF-κB regulates several pathways of negative feedback that promote its nuclear export and retention in the cytoplasm [27, 40]. Consequently, during persistent stimulation with high concentrations of TNF, nuclear NF-κB often adapts back to pre-stimulus subcellular distributions.

To demonstrate proof-of-concept for the dynamic stimulation system with living cells, we asked whether cells exposed to dynamic stimulation with TNF will alter the characteristic NF-κB response. HeLa cells that express a fluorescent protein fused to the NF-κB RelA subunit (FP-RelA) were seeded into the device and observed via time-lapse imaging within 3 days. The nuclear fluorescence of FP-RelA was measured in single cells exposed to either a step-like change in TNF concentration from 0 to 5 ng/ml or a slow ramp in concentration from 0 to 5 ng/mL over an 8-hour period (Figures 2.4 A and B). Consistent with our previous observations in HeLa cells [2], flow conditions did not have appreciable effects on nuclear NF-κB dynamics (Figure A4). Bioactivity of TNF also remained stable throughout the duration of experiments (Figure A5).

Previously we characterized adaptive and non-responsive classes of nuclear NF-κB dynamics in cells exposed to TNF as a step or a pulse [96, 97]. For ramp-stimulated cells we

observed qualitatively different single-cell responses where NF-κB remained in the nucleus during stimulus and also where NF-κB slowly accumulated in the nucleus over time (Figure 2.4 B and C). We refer to these respectively as sustained and increasing response classes. Based on quantitative descriptors for time-varying properties of nuclear FP-RelA (Figures A3, and A6; see also the Methods section), the response mode for each cell trajectory was classified as either Non-responsive (NR), Adaptive (A), Sustained (S), or Increasing (I) for step and ramp stimulation conditions (Figure 2.4 C). Although additional response classes may exist, the four response modes were robustly detected using an automated classifier (Figure A3 C, D, and E). Response classes found using the automated classifier were also consistent with those identified by manual inspection of data. For cells exposed to step stimulation, the clear majority showed 'Adaptive' behavior followed by a subpopulation of 'Non-responsive' cells and only smaller fractions of cells in the other modes. By contrast, most cells exposed to ramp stimulation showed a predominantly 'Increasing' response pattern (Figure 2.4 D). Enrichment of the 'Increasing' followed by 'Sustained' cellular response modes in response to a TNF ramp was at the expense of adaptive responses. 'Increasing' responses were also consistently enriched in experiments where cells were exposed to a more rapid ramp to 5 ng/mL over a 5-hour period (Figure A7). In both experiments, distributions of response modes when comparing step and ramp stimulation were statistically significant (Pearson's chi-squared test). These data demonstrate that modes of pathway activation are modulated by dynamic TNF stimulation, suggesting the classical 'Adaptive' response may be a consequence of step-like stimulation and not a defining characteristic of the signaling network.

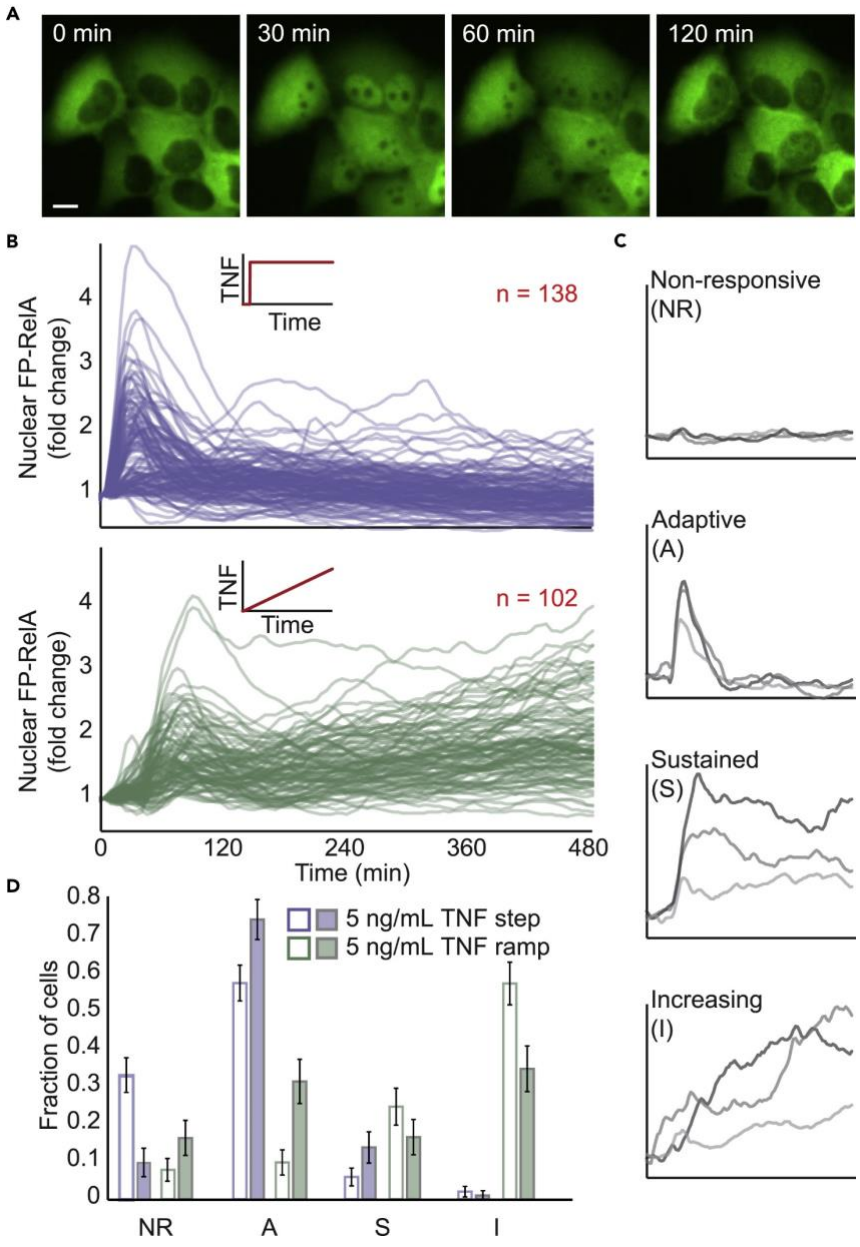

Figure 2.4 NF-κB Pathway Responses to Step and Ramp Stimulation in Single Cells

(A) Time-lapse images of FP-RelA-expressing HeLa cells exposed to TNF stimulation as a step-up to continuous 5 ng/mL at the 0-min time point. Scale bar, 10 μm. (B) Time courses of nuclear FP-RelA fold change measured in single cells exposed to TNF stimulation as a 5-ng/mL TNF step (top, see also Video S3) or a concentration ramp from 0 to 5 ng/mL (bottom) over an 8-h period for a representative experiment. Raw unprocessed time courses are shown in Figure A3. Inset numbers indicate the total number of cells per condition. (C) Time courses in (A) are classified into four cellular response modes: Non-responsive, Adaptive, Sustained, and Increasing. Representative

single-cell responses are depicted for each. See also Figure S3. (D) Fraction of single cells in each response mode for step and ramp stimulation show statistically significant differences in their distributions (p value < 0.00001; Pearson's chi-squared test). Independent biological replicates are shown as open and closed bars (Replicate 1: 138 cells step and 102 cells ramp; Replicate 2: 87 cells step and 80 cells ramp). Error bars represent standard deviation of 5,000 bootstrap samples.

2.2.4 Aggregate responses of cells to ramps are greater than step stimulation

The 'area under the fold change curve' (AUC) is a descriptor of nuclear FP-RelA dynamics that represents the accumulated response of a single cell to cytokine stimulation [96]. Comparisons of nuclear NF-κB dynamics in cells exposed to a pulse of TNF or lipopolysaccharide showed that cellular responses are well-determined by the product of stimulus duration and concentration [2, 23, 98]. We therefore asked whether the AUC of nuclear FP-RelA dynamics also integrate the concentration and duration of stimulus in response to a TNF ramp.

Contrary to expectations, AUC values for single cell responses were significantly greater during stimulation with an 8-hour TNF ramp versus step based on sampled permutation test ($p < 10^{-4}$; Figure A8), a statistic that shuffles data to generate distributions for the null hypothesis. Because Alexa647-conjugated BSA was combined with TNF in the same reservoir, its time-varying fluorescence was used to measure dynamics of TNF concentration experienced by each cell. Scatterplots for the AUCs of Alexa647 (total TNF input) and nuclear FP-RelA (total response) in the same cell showed that ramp stimulation generates stronger responses despite much smaller aggregate TNF exposure (Figure 2.5). Taken together, our data suggest that inflammatory pathway activation may be enhanced through dynamic properties of a stimulus, such as rate of change for cytokine concentration.

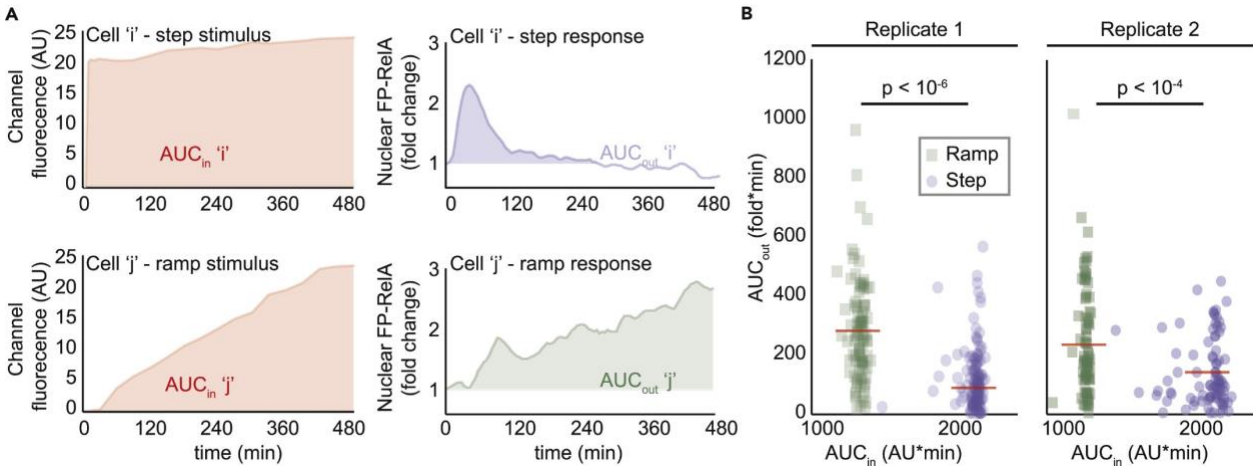

Figure 2.5 Ramp Stimulation Produces Greater Responses Despite Smaller Aggregate TNF Exposure

(A) For each cell, AUC of TNF exposure (AUCin, left column) and fold change AUC of nuclear FP-RelA response (AUCout, right column) are calculated. (B) Scatterplots for independent biological replicate experiments of AUCin (x axis) and AUCout (y axis) for both 8-h experiments (Replicate 1: 138 cells step and 102 cells ramp; Replicate 2: 87 cells step and 80 cells ramp; see also Figure 4) show that although ramp stimulus has less AUCin, it produces a greater cellular response. Differences between distributions for step and ramp stimuli are statistically significant based on permutation test.

2.2.5 Model predicts that rates of negative feedback determine modes of NF-κB activation

The NF-κB signaling network has been modeled as a system with two pathways of negative feedback (Figure 2.6 A) mediated through expression of IκBα and A20 [40, 42, 47]. Because transcription and translation are noisy biological processes that lead to variability in protein abundances [99], we reasoned that variability of single cell response classes to dynamic stimuli may be a consequence of cell-to-cell variability (CCV) in negative feedback strength. Using the D2FC model which was previously parameterized to HeLa cells [42], we simulated NF-κB responses while sweeping across a broad range of parameter values for both pathways of negative

feedback. For each pair of IκBα and A20 feedback parameters, single cells were simulated in response to step and ramp TNF exposure, and the resulting nuclear NF-κB time-courses were classified as described for live-cell data. Although both parameter sweeps produced a non-linear response landscape, simulation results for a TNF ramp showed greater complexity and uniquely contained the 'Increasing' response class in contrast with simulations for step TNF exposure (Figure 2.6 B).

Next, to simulate the effect of variability within a population of cells, we selected a region of parameter space that allowed variation over two orders of magnitude along each axis of negative feedback, and containing the original D2FC parameterization (Figure 2.6 B, red box 'CCV'; See also Methods section). Although simulated NF-κB time-courses displayed long-term oscillations that are less pronounced in human cancer cell lines [37, 96, 100], and non-responsive time-courses did not appear in deterministic simulations, simulated responses were otherwise qualitatively similar to live-cell data (Figures 2.4 B, 2.6 C). Consistent with living cells, simulated responses to step stimulation were almost exclusively 'Adaptive', whereas ramp stimulation was enriched for 'Increasing' followed by 'Sustained' modes of pathway activation (Figure 2.6 D, left). However, in contrast with live-cell results, nuclear NF-κB fold-change responses to a simulated ramp were smaller than step-stimulated cells (Figure 2.6 C). AUC values comparing simulated step and ramp stimulation also show significant differences ($p < 10^{-6}$; permutation test), but with opposite trends to experimental observations (Figure A8 C), suggesting that additional differences exist between the architecture of the D2FC and mechanisms in living cells. Taken together, simulations identify rates of transcription or protein translation as determinants for different response modes in single

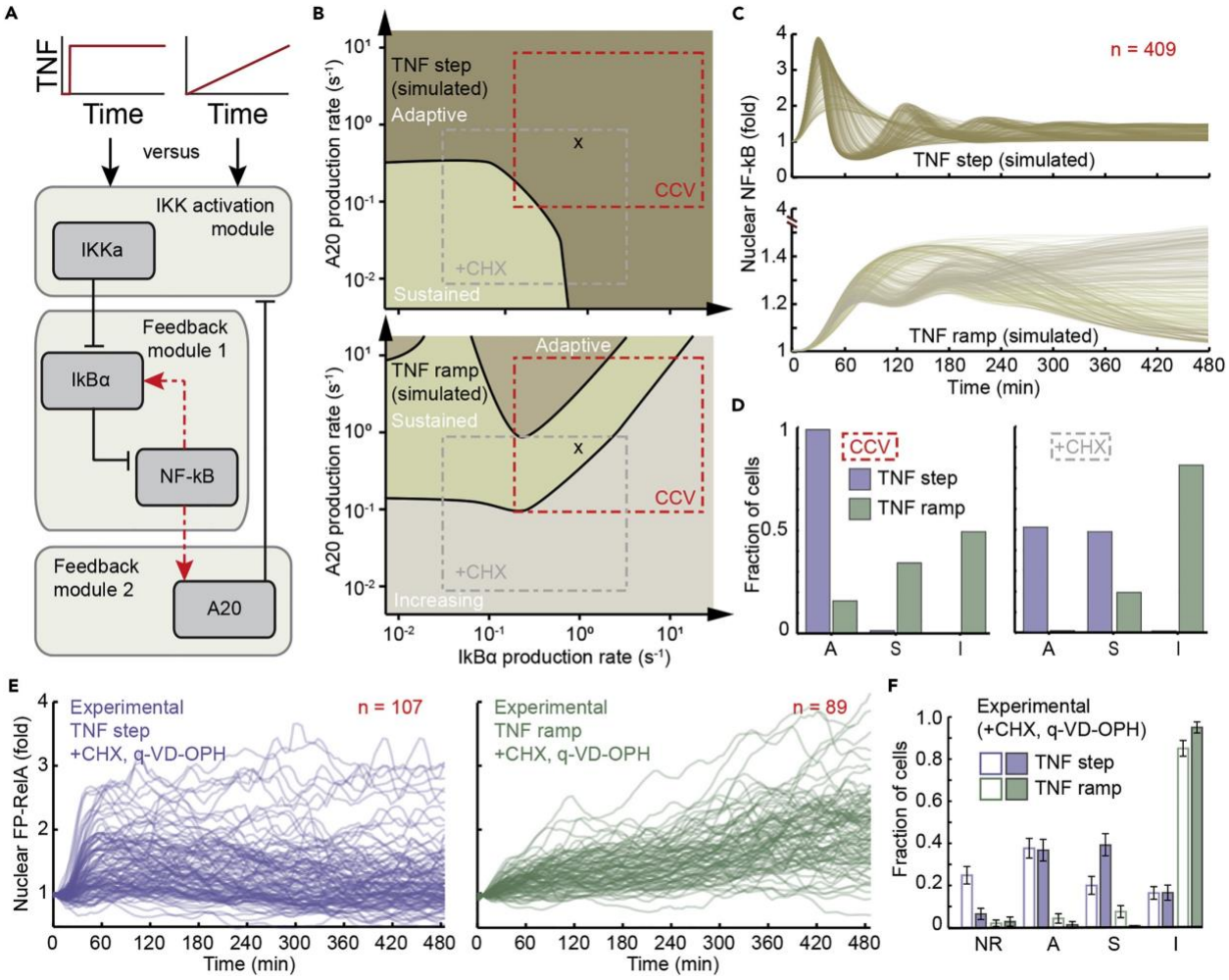

Figure 2.6 Cell-to-Cell Variability in Negative Feedback Recapitulates Response Modes

(A) Schematic of negative feedback modules within the D2FC computational model (Lee et al., 2014) of the NF-κB signaling network (see also Data S3). NF-κB-driven expression of genes that encode for IkBα and A20, respectively, acts to sequester NF-κB in the cytoplasm and to limit upstream kinase activity of IKK. The activated species is denoted as IKKa in the model. (B) Simulated single-cell responses to a TNF step (top) or TNF ramp (bottom) are classified into response modes across a range of production rates for IkBα and A20 to simulate cell-to-cell variability. Although variability was modeled by simulating different translation rates for negative feedback mediators, numerically identical results can be achieved by modeling variability in transcription. The default translation rates for IkBα and A20 in the D2FC are marked with an "x." (C) Cell-to-cell variability (CCV) is simulated by sampling values for IkBα and A20 translation rates across a range of values (red box in B; see also Transparent Methods). For each sampled pair of translation rates single-cell time course responses for a TNF step

(top) or TNF ramp (bottom) are simulated. Inset number indicates number of simulated single-cell trajectories. The y axis for the simulated TNF ramp (bottom) is scaled to assist with visualization of simulated time course responses. (D) Quantification of the fraction of single cells in Adaptive (A), Sustained (S), and Increasing (I) categories for simulated single-cell trajectories in boxes marked "CCV" (left) and "+CHX" (right) in (B) (see also Transparent Methods). The +CHX box simulates cell-to-cell variability in the presence of cycloheximide to inhibit protein translation. (E) Time courses of nuclear FP-RelA fold change measured in single cells exposed to TNF stimulation as a 5-ng/mL TNF step (left) or a concentration ramp from 0 to 5 ng/mL (right) over an 8-h period for a representative experiment. CHX (640 ng/mL) and caspase inhibitor (5 μM; q-VD-OPH) are introduced to the cell culture 30 min before TNF stimulation. Inset numbers indicate the total number of cells per condition. See also Figure S9. (F) Fraction of single cells in each response class for step and ramp stimulation are enriched for sustained and increasing responses, respectively, in the presence of CHX and q-VD-OPH (c.f. Figure 4D). Independent biological replicates are shown as open and closed bars (90 and 65 cells for step and ramp conditions, respectively, in replicate 2). Distributions for step and ramp stimulation in the presence of inhibitors show statistically significant changes when compared with step and ramp distributions, respectively, in the absence of inhibitors (Figure 4D; p value < 0.00001; Pearson's chi-squared test). Error bars represent standard deviation of 5,000 bootstrap samples.

cells exposed to dynamic stimuli.

Comparing simulations for step and ramp stimulation suggests a perturbation such as cycloheximide (CHX) that reduces rates for protein translation will respectively enrich for 'Sustained' and 'Increasing' response modes (boxes marked +CHX in Figures 2.6 B and D, right panel; See also Methods section). To test this model prediction, we exposed cells to a TNF step in a 96-well plate. Although combined TNF and CHX stimulation induces death in a fraction of cells, surviving cells showed increasingly sustained nuclear FP-RelA responses to TNF over a 5-hour window in proportion with CHX concentration (Figure A9). Based on the calibration experiment, cells were exposed to a TNF step or ramp in the dynamic stimulation system in the presence 640

ng/mL CHX in addition to q-VD-OPH, a pan-caspase inhibitor that prevents apoptotic cell death (Figure 2.6 E). While caspase inhibition is immunosuppressive and prevents nuclear RelA accumulation in human T cells [101], caspase inhibition showed only a partial effect and nuclear FP-RelA mobilization was still observed in HeLa cells. Consistent with model predictions, the response to a TNF step switched from predominantly 'Adaptive' to a nearly equal combination of 'Adaptive' and 'Sustained' in the presence of inhibitors (Figure 2.6 F, c.f. Figure 2.4 D). Similarly, after inhibition of protein translation nearly all cells exposed to a TNF ramp showed 'Increasing' behavior with a reduced fraction of cells with 'Adaptive' and 'Sustained' responses as predicted by simulations (Figure 2.6 F). Overall, by taking advantage of live-cell data and models, cell-to-cell variability in rates for expression of negative feedback mediators is identified as a likely contributor to behavioral diversity in cells exposed to dynamic stimuli.

2.3 Discussion

Dynamic patterns of stimulation are necessary to probe the capabilities of signal transduction pathways and to understand how dynamic biological events modulate cellular behaviors in vivo. In this work, we have developed a microfluidic dynamic stimulation system for user-defined control of extracellular microenvironments. Circumventing the conventional pumping and control apparatus, our system uses gravity alone to provide precise control of stimulus dynamics. Furthermore, the system can be built from inexpensive and commonly available parts. The low operating pressures in our gravity-driven system result in minimal shear forces in the cell culture channel and are compatible with long-term cell viability during imaging experiments. Because the system's design is modular, the attached device for an experiment can

be selected to provide particular capabilities such as broad dynamic range or independent control for multiple stimuli among other possibilities. Complementary to optogenetic approaches that isolate and perturb spatiotemporal dynamics of molecular signals [102, 103], our system probes the spatiotemporal dynamics of receptor-ligand interactions or drug-response mechanisms in single cells.

Device fabrication in addition to the presence of cells and cell culture reagents can all lead to subtle variability between predicted and actual experimental results. Fluorescent dyes are useful tools to evaluate the quality of an experiment within the dynamic stimulation system. In our case, the bioactive form of TNF is trimeric with a molecular weight of 55kDa [104] and Alexa647-conjugated BSA was selected to mark the TNF-containing laminar stream because it has a similar molecular weight and diffusive properties. Although TNF slowly dissociates into monomers over a timescale of days when stored at low concentrations [105, 106], this is not expected to affect our results. Inside the dynamic stimulation system, TNF is stored at high concentrations and diluted within minutes of exposure to cells, effectively minimizing dissociation of TNF at low concentrations. Monomers that dissociate within this timescale will extend beyond the Alexa647-BSA laminar boundary (Figure A2 C) due to its increased diffusivity; However, monomeric TNF denatures rapidly [106, 107] and will not have biological activity in these regions of the device. Subsequent studies using similar dynamic stimulation should carefully choose tracer dyes that appropriately reproduce characteristics of ligands or molecules in the flow chamber.

When compared with step stimulation, dynamic stimulation revealed novel response classes and enhanced activation of NF-κB signaling despite smaller TNF exposure in the proof-of-concept live cell experiments. Our computational model suggests that distributions of NF-κB response modes culminate from biological noise that influences the strength of negative feedback

pathways in each cell. Production and decay rates for mRNA and protein govern their abundance within a cell and are subject to varying amounts of gene-specific noise [99, 108]. Age, stress, and cell cycle phase are a few of many contextual factors of single cells that affect reaction rates within the central dogma [109, 110], and are likely to contribute to cell-to-cell variability of response modes to dynamic stimuli. Although our model did not show enhanced activation of NF-κB signaling in ramp-stimulated cells, we surmise that a molecular circuit upstream of IKK activation is missing from the D2FC and other models. Indeed, studies of cytokine-dependent refractory states continue to uncover molecular determinants that are required to capture the behavior of mammalian cells [111, 112]. Subsequent studies may reconcile these observations by investigating the molecular architecture and parametric constraints in the signaling network that reconstitute these missing capabilities. We expect other well-studied signaling systems will also benefit from characterization under the lens of dynamic stimuli, using the dynamic stimulation system developed here to probe signaling networks with detailed experiments.

2.4 Methods

See full text online for additional data, tables design files, and videos:

https://doi.org/10.1016/j.isci.2019.08.010

2.4.1 Gravity pump overview

The gravity pump is controlled by a programmable Arduino mega 2560 microcontroller (Arduino). The stepper motors (generic DC 4-9V Drive Stepper Motor Screw with Nut Slider 2-Phase 4-Wire), Arduino controller, and stepper drivers (A3967 Easydriver V44) are mounted on a custom-made acrylic frame with machined holes to ensure level mounting. Each stepper motor is controlled by its own stepper driver board powered by a 9V 5A power supply. The stepper driver logic pins are connected to and controlled by the Arduino digital I/O pins. Each stepper motor assembly has a screw-nut drive platform that moves up or down vertically as per the direction of rotation of the motor. We designed and 3D-printed basins with a base allowing them to attach stably to the stepper platforms and an internal volume of 1.64ml. The basins contained ports with sufficient tolerances to allow friction fit with tygon tubes (Fisher Scientific 1471139).

2.4.2 Design and microfabrication of the dynamic stimulation device

Autodesk Fusion 360 CAD software (Autodesk) was used to design the molds and produce the corresponding STL design files for 3D printing. Molds were printed with Solus Proto resin using a SOLUS DLP 3D printer (Junction3D) in the high-resolution (25 μm X/Y) setting and 25

μm Z axis step size. Freshly printed molds were washed with ethanol and exposed face up to UV light for 30 minutes while submerged in ddH2O. Cured molds were adhered to a 10 cm cell culture dish with double sided tape.

PDMS (Sylgard) was prepared at a ratio of 10:1 PDMS to hardening agent and poured over the mold. Vacuum was applied to remove bubbles and the device was placed in incubator at 70 0C to cure for approximately 2 hours. Alternatively, lower temperature can be used which results in longer curing time. The hardened PDMS around the base of the mold was cut with a box cutter and the device carefully peeled from the mold. The edges of the device were trimmed with razor blade and 1.25mm holes were punched into the inlets, outlet, and loading channels. Devices were then soaked in 70% EtOH for 30 minutes and let dry for an additional 30 minutes. The base of each device was cleaned using scotch tape to remove any dust and debris. The device was plasma bonded (Harrick Plasma, PDC001) to 45mmx50mm glass cover slip at 800mtorr pressure on the high setting for 1 min. Due to the low pressures during operation, we expect the dynamic stimulation device should be compatible with other non-plasma approaches that reversibly bond PDMS and glass [113]. Cell cultures exposed to solidified resin from the 3D printer (UV-treated) continued to survive and grow with the same rates and morphology as untreated cells, suggesting that any trace residues from the fabrication process are compatible with cellular assays.

2.4.3 Device preparation and cell seeding

Dynamic stimulation devices made in PDMS were autoclaved and treated with UV light for disinfection. Devices were washed with ethanol and then with a solution of 0.002 v/v fibronectin in phosphate buffer saline (PBS). The devices were then incubated with the fibronectin solution for 24 hours by using 200μl pipette tips inserted in the inlets.

For cell seeding, devices coated with the fibronectin solution for 24 hours were flushed with media multiple times. All the inlets except the cell seeding ports were plugged with PDMS plugs made by hardening PDMS in 200 µl pipette tips, and a 200 µl pipette tip filled with media was inserted in the wider seeding port. Cells suspended in media between $3*10^6$ and $8*10^6$ cells/ml density were seeded through the narrower seeding port while observing under a microscope. After reaching a cell density for approximately 60% confluence, the narrower cell-seeding port was plugged with a PDMS plug and the device is incubated for at least 24 hours, allowing cells to attach and spread out on the glass surface. The PDMS plugs at the inlets and outlet were then replaced with a 200 µl pipette tip filled with medium and further incubated until the time of experiment with daily medium changes.

2.4.4 Control model for the dynamic stimulation system

The three controlled variables in the model are the volume fraction of drug (Xc), the laminar interface position of the treatment stream (LP) and the total volumetric flow rate (Qc):

$$Xc = \frac{Q1}{Q1 + Q2}$$

$$LP = \frac{Q1 + Q2}{Q1 + Q2 + Q3}$$

Qc = set by the user

Where Q1, Q2 and Q3 are the inlet flow rates corresponding to the inlets I1, I2 and I3 (Figure 2.1 A).

A linear model between the hydrostatic pressures (P1, P2 and P3) and the inlet flow rates (Q1, Q2 and Q3) is used to determine reservoir heights corresponding to the desired values of controlled variables (Xc, Lp and Qc):

$$Q = R * P$$

$$h(mm) = \frac{P}{9.8 * 1000}$$

Where Q is the 3x1 vector of inlet flow rates, P is the 3x1 vector of driving pressures, h is the 3x1 height vector corresponding to the hydrostatic pressures, and R is the 3x3 fluidic resistance matrix. Multiple CFD simulations corresponding to different combinations of the three driving pressures were carried out in ANSYS-Fluent to calculate the corresponding inlet flow rates. The linear model was then fitted to these data to estimate the resistance matrix R. A calibration experiment was run with the model output and compared with the desired input. The model was then adjusted accordingly, and the calibration was repeated until the desired accuracy was achieved.

The system was controlled via an open loop control mechanism. The experimental protocol in terms of controlled variables Xc, LP and Qc was input into an Arduino code printer Python script, which outputs the corresponding Arduino code according to the calibrated model. The code was then uploaded to the Arduino microcontroller on the pump. Qc was set to a very low value ($Qc = 5 * 10^{-11} \frac{m^3}{s}$) in order to lower the shear stress on cells, which results in time delay of about 4-5 minutes before Xc reflects the changes in heights h1 and h2. This delay introduces a short time lag before changes in input Xc are detected in the cell culture region of the device. Greater flow rate can reduce this delay at the expense of higher shear stress on cells. In contrast with Xc, control over LP through h3 responds in under 10 seconds and is used to generate sharp pulses.

2.4.5 Experimental setup

Autoclaved Tygon tubes (Fisher Scientific 1471139) were washed with ethanol and PBS before multiple washes with DMEM medium. Tubes were inserted in the outlets of basins and media was again flushed through the tubes while carefully avoiding bubbles. Alexa647-conjugated BSA (0.0025 v/v; Invitrogen) solution in DMEM was used to prepare the TNF treatment which would later be used to quantify TNF concentration. For calibration experiments, mixtures of Alexa488-conjugated BSA and FluoSpheres (580/605, 2μm, Invitrogen) were used. This solution was flushed through the corresponding basin and attached tube. Basins with media and TNF treatment were placed on corresponding platforms on the pump with attached Tygon tubes. The other ends of the tubes were inserted in the corresponding inlets on the device. The tubes were clamped with plastic pinch clamps immediately after connection to the device to avoid pre-treatment. The device was then fitted to a custom adapter and placed under the microscope for imaging. The clamps were removed at the beginning of the experiment. In experiments with translational inhibition, CHX (640 ng/mL, Sigma) and pan-caspase inhibitor q-VD-OPH (5μM, Thermo Fisher) were introduced to the dynamic stimulation device approximately 30 minutes before step and ramp stimulation.

2.4.6 Cell lines and culture

Hela cells stably expressing of EGFP-RelA as described previously [42] were cultured in Dulbecco's Modified Eagle Medium (DMEM) supplemented with 10% Fetal Bovine Serum (Corning), 100 μg/ml Streptomycin and 100 U/ml Penicillin (Corning, 30-002-Cl), and 0.2 mM L-glutamine (Corning, 25-005-Cl) at 37 °C and 5% CO2.

2.4.7 Microscope and live-cell imaging

Cells in the dynamic stimulation devices were imaged at 20X (0.45NA; Olympus) resolution with the climate controlled (37 °C, 5% CO2) DeltaVision Elite microscope (GE). Constant flow rate of Qc = 5x10-11 m3/s was used for all experiments as the model input. Cells continue to grow and divide in the device at these conditions for more than 12 hours. Time-lapse images were collected at 5-minute intervals using FITC and Cy5 filters.

2.4.8 Data analysis and trajectory classification

Trajectories of nuclear mean fluorescence intensity (MFI) in both EGFP-RelA (FITC channel) and Alexa647-conjugated BSA (Cy5 channel) were collected with custom ImageJ scripts. The EGFP-RelA trajectories were normalized to the average nuclear MFI of the two frames prior to the introduction of TNF to establish the baseline for fold-change transformed trajectories. Alexa 647 BSA trajectories were normalized with the maximum intensity (final intensity in case of ramps) to get the fractions intensity at each time point. These normalized trajectories were then used as a proxy for volume fraction (Xc) to determine TNF concentration for each cell as C = Cmax*Xc. Every trajectory was smoothened by a 3-frame moving average to remove high-frequency noise. Cells undergoing division, cell death, or that left the viewing area over the duration of the experiment were excluded from analysis. In addition, for experiments with CHX cells that underwent significant morphological changes or changes in overall expression of EGFP-RelA were not considered further.

The EGFP-RelA fold change trajectories were sorted into four categories: adaptive, sustained, increasing, and non-responding. First, the non-responders were filtered by comparing

the fold change over the rolling window of 3 hours. Cells having more than 1.25-fold change for more than three time points within a rolling 3-hour window were considered responding. Cells in the responding category were further divided as adaptive and non-adaptive by examining the fold-change values at the end points. Responding cells having end-point values comparable to unstimulated cells (between 1- and 1.3-fold) were classified as adaptive, and cells with higher end-point values were considered non-adaptive. Finally, the non-adaptive cells were split into sustained and increasing categories by comparing the maximum fold change between 0 and 150 minutes and during the rest of the experiment. If the max between the first 150 minutes was more than 1.1 times higher than the max in the rest of the experiment, the trajectory was considered sustained, otherwise it was considered increasing. Finally, trajectories were manually inspected and curated to correct misclassifications.

2.4.9 AUC of nuclear FP-RelA calculation

The area under the curve for nuclear FP-RelA was calculated as described previously [96]. Here, the area bounded positively by the fold change of nuclear FP-RelA (FC) and the initial FP-RelA value of 1 after the time of stimulus i.e. defined by:

$$\sum_{i=time\ stimulus\ begins}^{i=end\ of\ experiment} (\max(1, FC(i)) - 1)$$

2.4.10 Permutation test

For permutation tests, the AUC of FP-RelA from cells exposed to step and ramp

stimulation conditions were combined and randomly distributed into 'Permuted step' and 'Permuted ramp' bins without replacement, preserving the size of the original step and ramp data sets. 10^6 permutations were performed and the difference between the means of 'Permuted step' and 'Permuted ramp' data was calculated to generate a histogram. Two-tailed p-values were determined by computing the fraction of permuted data sets where $\Delta\text{mean}_{\text{permuted}} \geq \Delta\text{mean}_{unpermuted}$ (Figure A4).

2.4.11 Simulated single-cell trajectories

The "Deterministic 2-Feedback with Competition" (D2FC) model [42] was used to investigate the role of negative feedbacks in producing the novel response modes. All parameters were used at default as described previously except for IKK activation (ka), used as proxy for TNF concentration in the D2FC, in addition to IkBα and A20 translation rates (ca and c1a, respectively). to simulate ramp stimuli, we modified the D2FC model with variable IKK activation rate defined as:

$$\frac{dKa}{dt} = \frac{Ka\ corresponding\ to\ continuous\ stimulus}{Total\ time\ (\text{sec})}$$

Therefore, for continuous stimulation, Ka is set to a constant value (Ka = 0.00025) at time t=0, and for ramp stimulation, Ka increases linearly from 0 up to its final value (Ka_{final} = 0.00025) over the duration of simulation.

2D parameter sweeps for IkBα and A20 translation rates (parameters ca and c1a) were performed across several orders of magnitude around their default D2FC values using latin-hypercube sampling. For each parameter combination responses to step and ramp stimulation was simulated. Each trajectory was classified as Adaptive, Sustained, or Increasing as described for the

live-cell data and used to define the parameter response space (Figure 6B). Because the simulations are deterministic and cells are exposed to the same TNF step or ramp, simulations did not produce any non-responsive trajectories. All single cell simulations were performed in MATLAB (Mathworks) using the ode45s solver.

2.5 Author contributions

Conceptualization, R.E.C.L.; Methodology, R.E.C.L., C.S.M., D.L.S., and M.A.Q.; Investigation, C.S.M. and D.L.S.; Formal Analysis, C.S.M., D.L.S., and R.E.C.L.; Writing – Original Draft, R.E.C.L., C.S.M. and D.L.S.; Writing – Review & Editing, R.E.C.L, C.S.M, D.L.S., and M.A.Q. Visualization R.E.C.L.; Funding Acquisition, R.E.C.L.; Supervision, R.E.C.L.

3.0 Dynamics of IKK-mediated transmission of cytokine signals in the NF-κB pathway

This chapter is taken from Cruz JA*, **Mokashi CS***, Kowalczyk GJ, Guo Y, Zhang Q, Gupta S, Schipper DL, Smeal SW, Lee REC. "A variable-gain stochastic pooling motif mediates information transfer from receptor assemblies into NF-κB", Science Advances, 2021 *co-first authors [54]. Details of author contributions can be found in Section 3.5.

3.1 Introduction

A limited number of transmembrane receptors expressed on the cell surface mediate crucial transmission of information between extracellular and intracellular signaling molecules. Key questions are understanding the mechanisms and limitations that underlie signal transmission, in particular for cytokine receptor signaling that is often deregulated in disease. The nuclear-factor kappa-B (NF-κB) signaling pathway is an archetypal molecular communication channel that transmits information about extracellular cytokines to regulate cellular adaptation through activation of the RelA transcription factor [51, 52, 114]. When ligated with inflammatory molecules, such as tumor necrosis factor (TNF), interleukin-1-β (IL-1), among others, many activated receptors converge on NF-κB signaling [25, 115].

Ligation of TNF to the TNF receptor (TNFR1) recruits adaptor proteins and enzymes to form a large multiprotein complex near the plasma membrane [29, 31, 32, 116]. Ubiquitin

modifying enzymes are critical components that assemble linear, branched, and mixed polyubiquitin scaffolds around the multiprotein complex [34, 35, 117, 118]. The NEMO subunit of the cytoplasmic IκB-kinase (IKK) complex is rapidly recruited via direct interaction with the polyubiquitin scaffold and accessory proteins, where IKK is activated through induced proximity with regulatory kinases [25, 119-121]. The fully assembled TNFR1 complex, referred to as 'Complex I' (CI; [29]), is a master regulator of inflammation-dependent NF-κB signaling. Although other inflammatory molecules such as IL-1 signal through CI-like complexes using different receptors, adaptor proteins [30, 33], and varying compositions of ubiquitin chain scaffolds [36, 122], all regulate NF-κB through IKK activation mediated by induced-proximity with other signaling mediators that reside on CI [38].

When observed in single cells exposed to inflammatory stimuli, the RelA subunit of NF-κB encodes a dynamic transcriptional signal by translocating from the cytoplasm into the nucleus [10, 41, 42, 51, 52]. Models calibrated to single-cell RelA data [10, 27, 42, 49] have revealed numerous transcriptional mechanisms and emergent properties that place the NF-κB pathway among exemplars of dynamical biological systems [5, 123]. Key to these findings are two mediators of negative feedback, IκBα and A20, which are transcriptionally regulated by NF-κB. IκBα restores NF-κB to its baseline cytoplasmic localization through nuclear export and sequestration, whereas A20 diminishes kinase activation upstream of NF-κB through disassembly of CI-like structures in addition to non-catalytic mechanisms [10, 27, 34, 45, 49]. Dynamical regulation of transcription and feedback via NF-κB is strongly recapitulated between models and experiments; however, there is a dearth of quantitative single-cell data at the level of cytokine detection and dynamical properties of CI-like complexes to substantiate our understanding of upstream signal transmission.

Here, we develop genetically modified cells that endogenously express fluorescent protein fusions of NEMO and RelA, allowing same-cell measurements of CI-like structures and canonical NF-κB signaling from live-cell images. We establish differences between TNF and IL-1 responses in biophysical properties of NEMO complexes and demonstrate a continuum relating CI-like structures and downstream NF-κB responses in the same cell. By tracking single complexes, we demonstrate that: (i) cytokine dosage and time-varying presentation modulates the timing and numbers of CI-like structures; (ii) single complexes have switch-like activation profiles where the aggregate of NEMO recruitment and time-varying properties of each complex are cytokine-specific; and, (iii) that dynamics of formation and dissolution for single complexes during the primary cytokine response are independent of transcriptional feedback. Finally, we characterize a signaling motif called a variable-gain stochastic pooling network (SPN) that encompasses our experimental observations. The variable-gain SPN motif has beneficial noise-mitigation properties and provides a trade-off between information fidelity, ligand specificity, and resource allocation for intracellular signaling molecules. We propose that the variable-gain SPN architecture, and its associated benefits to signal transmission, are common mechanisms for receptor-mediated signal transduction.

3.2 Results

3.2.1 Surface receptor expression is limiting for numbers of cytokine-induced signaling complexes

IKK activity is a convergence point for pro-inflammatory signals that regulate NF-κB downstream of many cytokine receptors [49, 124]. Ligands that bind to multiple receptors with differing kinetics [125], and decoy receptors that sequester or antagonize signaling complexes [126], layer additional complexity to signal initiation at the plasma membrane. To establish expectations for numbers and types of IKK-activating complexes, we measured surface receptor expression in U2OS cells that were previously shown to form dynamic IKK puncta in response to TNF and IL-1 [36, 37]. Using flow cytometry with reference beads for absolute quantification, we estimated the number of surface receptors per cell for TNFR1, TNFR2, IL-1R1, IL-1R2, and IL-1-R3 (Figures 3.1 and B1). On average, each U2OS cell presented approximately 1300 TNFR1, 700 IL-1R1, and an abundance of IL-1R3 surface receptors. Only a small number of TNFR2 and IL-1R2 were detected on the cell surface. For reference, we measured surface receptors on HeLa and KYM1 cells (Figure B1) and found results consistent with previous reports for TNFRs [127-129], and agreement with surface receptor expression in other cell lines [130-133]

Although activated TNFR1 and TNFR2 both form TNF-induced homotrimeric complexes, the TNFR2 subtype binds with lower affinity to soluble TNF and shows enhanced activation by membrane-bound TNF [125, 134]. In contrast, ligand-activated IL-1 receptor (IL-1R1) forms a heterodimer with the IL-1R3 accessory protein and dimerization can be inhibited through competitive sequestration by the IL-1R2 decoy [126] (Figure 3.1 A). Because surface expression

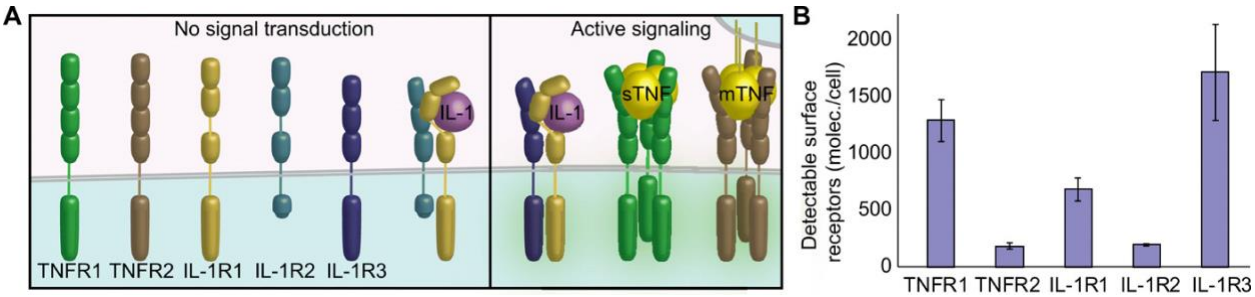

of TNFR2 and IL-1R2 are comparably low in U2OS, receptor composition of TNF and IL-1-induced

Figure 3.1 Differential expression of cytokine receptors enables cells to selectively respond to their environment

(A) Schematic of cognate receptors for TNF and IL-1 cytokines. Monomeric receptors and receptors that engage with decoy receptors (IL-1R2) are inactive and do not transmit signals into the cytoplasm (left). Activated receptor complexes (right), consisting of a TNFR homotrimer bound to TNF or an IL-1R1–IL-1R3 heterodimer bound to IL-1, are capable of seeding CI-like complexes in the cytoplasm. (B) Quantification of surface receptor expression on single U2OS cells. The average of three to seven biological replicates is shown for each condition. Error bars represent SEM.

oligomers will consist predominantly of TNFR1 trimers and IL-1R1-1R3 respectively. Together with known receptor-ligand stoichiometry (Figure 3.1 A), our results predict that single cells can simultaneously form a maximum of hundreds of IKK-recruiting complexes for saturating cytokine concentrations (approximately 400 and 700 for TNF and IL-1 respectively). Remarkably, surface receptor expression is significantly lower than numbers for downstream signaling molecules such as NEMO that are expressed in orders of a million per cell [135].

3.2.2 Cytokine-specific and dose-specific modulation of NEMO complex features

We set out to investigate how cytokine receptors engage NEMO as an integration hub to regulate NF-κB signaling. To counteract effects of NEMO overexpression, which can significantly inhibit NF-κB activation (Figure B2, and [135]), we used CRISPR/Cas9 for targeted insertion of coding sequences for fluorescent proteins into the U2OS cell line. The resulting cells co-express N-terminal fusions of EGFP-NEMO and mCh-RelA from their endogenous loci which can be used to monitor dynamic signaling events by live-cell imaging [37].

In response to TNF or IL-1, EGFP-NEMO transiently localizes to punctate structures near the plasma membrane [36, 37, 122] that are distinct from endosomal structures (Figures 3.2 and B3). To further characterize the role of cytokine identity and dose on NEMO recruitment at CI-like puncta, we compared descriptive features such as their size and intensity across different cytokines and concentrations. Although properties of IL-1 and TNF-induced puncta did not show a clear trend across doses, IL-1-induced spots were significantly larger and brighter than their TNF-induced CI counterparts (Figure 3.2 C; for all comparisons p-value $<< 10^{-10}$, student's t-test). To estimate the expected number of NEMO molecules in each complex, we evaluated intensity values for each fluorescent spot in terms of a reference live-cell reporter that recruits a known number of EGFP molecules into a diffraction-limited space [136]. By comparing cells in identical imaging conditions, our analysis suggests that each of the larger IL-1-induced spots recruit approximately 300 NEMO molecules whereas TNF-induced spots recruit around 80 (Figures 3.2 D and B4).

Time-courses for NEMO complexes in single cells showed a peak in spot numbers between 10-20 minutes and a rapid falloff thereafter (Figure 3.2 E), consistent with previous results from cytokine-induced IKK kinase assays [49, 137]. Numbers of NEMO spots per cell increased with

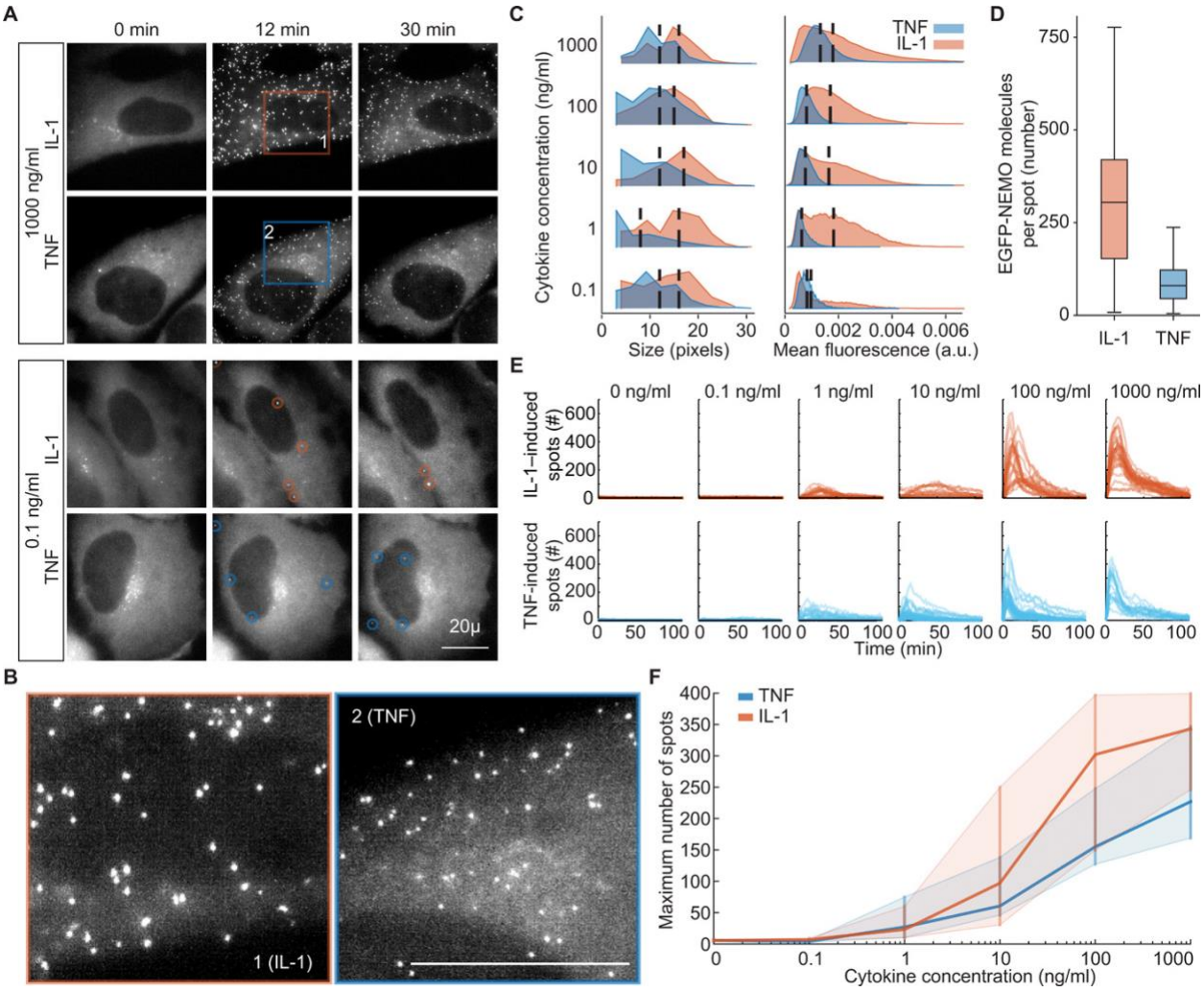

Figure 3.2 Size and intensity of NEMO complexes are modulated by cytokine identity independent of dose

(A) Maximum intensity projections from 3D time-lapse images of endogenous EGFP-NEMO show rapid recruitment to CI-like complexes in cells exposed to IL-1 or TNF. See also movies S1 and S2. (B) Details of fluorescent complexes [orange and blue boxes in (A)] show differences between responses to IL-1 and TNF. Scale bar, 20 µm for all. (C) Histograms summarizing the size (left) or intensity (right) of EGFP-NEMO complexes across concentrations of IL-1 (orange) or TNF (blue). Distributions represent single-cell data in aggregate from three to five experiments. Vertical bar indicates the median of each population. Comparison between all conditions, IL-1–induced complexes are larger and brighter than TNF-induced complexes ($P << 10^{-20}$; t test). Numbers of cells analyzed and associated spot numbers are provided in table S1. a.u., arbitrary units. (D) Boxplot for estimates of the total number of EGFP-NEMO molecules in each CI-like complex. Median and interquartile ranges are indicated.

See also Methods and figure B2 D. (E) Single-cell time courses for the number of EGFP-NEMO complexes in cells exposed to indicated concentrations of IL-1 (orange) and TNF (blue). (F) Dose response of maximum number of EGFP-NEMO complexes. Dark orange and blue lines represent the median, and vertical bars represent the interquartile range for cells stimulated with IL-1 or TNF, respectively.

cytokine concentration and showed a tendency of higher numbers in response to IL-1 at comparable molarities (Figures 3.2 E and F). Taken together, these data indicate that the size and intensity of NEMO complexes depend on the type of engaged receptor, whereas the number of complexes is modulated by cytokine dose.

3.2.3 NF-κB responses are well determined by descriptors of NEMO complexes

Next, we investigated the relationship between cytokine-induced dynamics of NEMO and RelA to ask whether NF-κB responses are well-determined by properties of fluorescent NEMO puncta when measured in the same cell. Time-courses for NEMO complexes and nuclear RelA localization were measured in response to a broad range of cytokine concentrations, and quantitative descriptors that summarize dynamic properties of EGFP-NEMO and mCh-RelA were extracted for each single cell (Figure 3.3 A and B, see also [42, 52]). Scatterplots of descriptors showed that cytokines and concentrations together form a continuum with a strong monotonic relationship between descriptors of NEMO and RelA (Figures 3.3C, B5). We also compared coefficients for determination between NEMO and RelA descriptors which showed stronger correlations when data are log-transformed (Figure B5). Increased R^2 values in log-space is because the NEMO-RelA relationship is likely governed by a power law, which is expected for a signal amplification mechanism with values that scale across orders of magnitude. Correlations

between same-cell descriptors of NEMO and RelA revealed a strong effect size indicating that cell-to-cell variability in NF-κB response can be reasonably determined by descriptors of EGFP-NEMO (Figure 3.3 C and D). Multiple linear regression for combinations of NEMO descriptors only marginally increased correlations (Figure B6).

Previously, we showed that the 'Area Under the Curve' (AUC) and 'Maximum' (MAX) are scalar descriptors of a nuclear RelA fold-change time-course that encode the most information about cytokine dose [52]. Notably, among all descriptors for nuclear RelA fold-change dynamics, AUC_{RelA} and MAX_{RelA} also had the strongest correlation with same-cell descriptors of NEMO-recruiting complexes (Figure 3.3 D; AUC_{NEMO} and MAX_{NEMO} respectively). Both NEMO descriptors showed similar coefficients-of-determination for RelA descriptors, whether measured in terms of numbers for EGFP-NEMO spots or aggregate intensity of EGFP-NEMO within complexes (Figure B5).

Overall, same-cell measurements of EGFP-NEMO and mCh-RelA reveal that the aggregate NF-κB response in a cell is well determined by the sum of NEMO recruitment to CI-like signaling complexes near the plasma membrane. Because enrichment of NEMO at ubiquitin-rich structures is an induced-proximity mechanism for kinase activation, it's reasonable that the AUC of EGFP-NEMO intensity in puncta is a strong proxy for downstream signaling. However, our characterization for the EGFP-NEMO fluorescence intensity at cytokine-induced spots showed wide-based distributions which could indicate that the amount of NEMO recruited at each spot varies significantly (Fig. 3.2 C). Nevertheless, the number of EGFP-NEMO puncta (MAX_{NEMO}) is almost interchangeable with AUC_{NEMO} as determinants of same-cell responses.

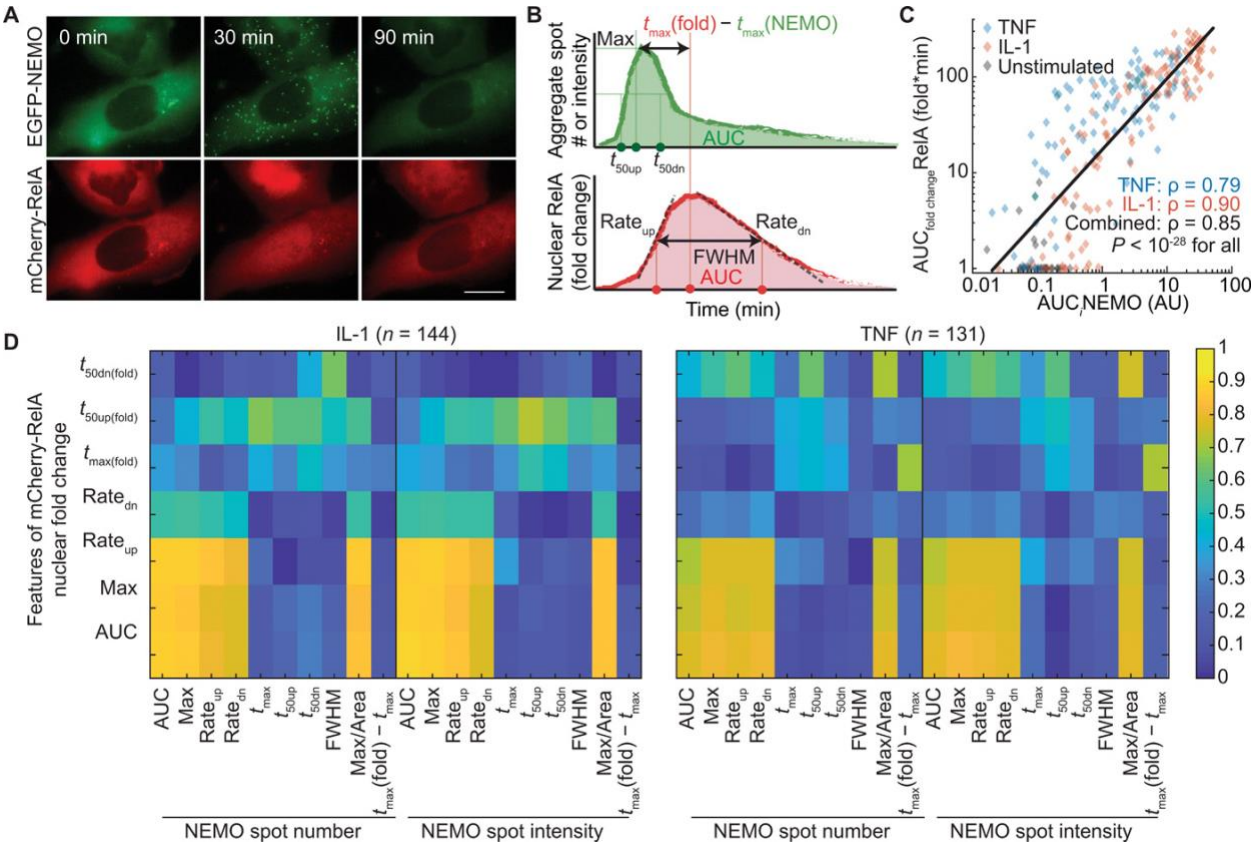

Figure 3.3 Same-cell NF-κB responses are determined by number and intensity of NEMO complexes

(A) Maximum intensity projections from 3D time-lapse images of EGFP-NEMO (top) and mCherry-RelA (bottom) expressed endogenously in the same U2OS cells. Cells were stimulated with IL-1 (10 ng/ml). (B) Diagrams indicating time-course descriptors for EGFP-NEMO complexes (top) and nuclear fold change of mCherry-RelA (bottom) in single cells. RelA features are similar to those used previously (3, 24). (C) Example of a strong same-cell correlation between single-cell descriptors of EGFP-NEMO complexes and nuclear RelA fold change. IL-1 and TNF responses across all doses overlap and form a continuum that relates the paired descriptors. (D) Heatmap of Spearman's rank correlation coefficients (ρ) for all pairs of same-cell descriptors for IL-1 (left) and TNF responses (right). See also figure B5 and table B2 for summary of cell numbers per condition. FWHM, full weight at half maximum.

3.2.4 Cytokine environments control numbers and timing of NEMO complex formation

Asynchronous properties of EGFP-NEMO spots, such as when a spot forms or rates for NEMO recruitment and dissolution, will contribute to variability when spot intensities are measured from a snapshot image at a single time point. To understand the extent of inter-spot and between-cell variability, we used high-frequency imaging to enable tracking of each single spot over time (Figures 3.4 and B7 A). Cells were stimulated with a step, pulse, or ramp in cytokine concentration in a microfluidic cell culture system [46] to observe how dynamic environments modulate properties of NEMO-recruiting complexes.

Tracking experiments revealed differences in fluorescence intensity time-courses, where IL-1 induced EGFP-NEMO puncta were consistently brighter and longer-lived than TNF-induced puncta (Figure 3.4 B). Both cytokines induce spots that peak within 2 to 3 minutes of detection followed by a decay phase where spots decline in intensity (Figure 3.4 B and B7 B). When stimulated with a cytokine pulse, most spots are detected only after the cytokine is removed (Figure 3.4 C) demonstrating that formation of NEMO-recruiting complexes is variable and takes place up to 30 minutes following a stimulus. Step, pulse, and ramp stimulation further showed that the number of spots and the timing of spot formation are both modulated by the dynamics of cytokine presentation.

Descriptors for single spot trajectories showed remarkably low variability, in particular for the TNF response, when compared within the same cell or when the average of single-spot descriptors was compared between cells (Fig. S7C and D). Analysis of the 'AUC spot intensity' descriptor (AUC_i) revealed a quadratic relationship between 'mean AUC_i' and 'AUC_i variance' for spots when measured in the same cell (Fig. S7E). Increased variance between large NEMO-recruiting complexes may be due to steric properties of supramolecular assemblies. For example,

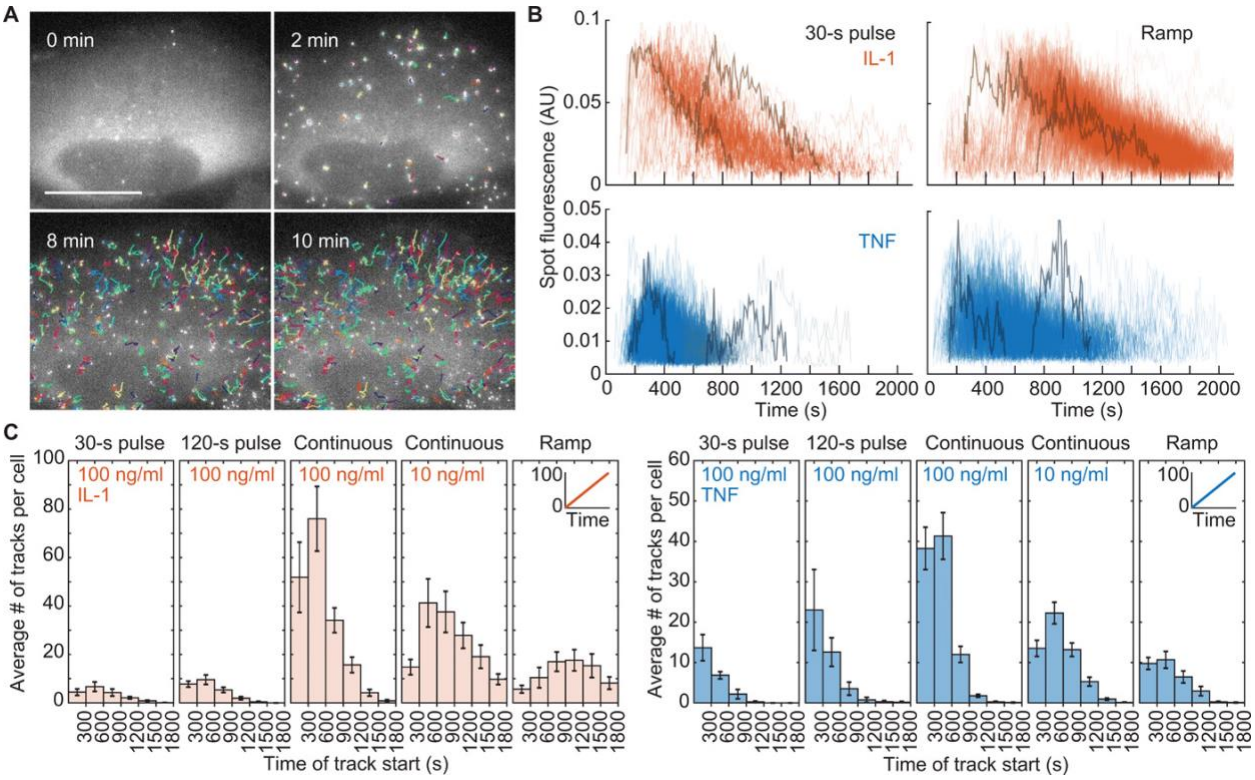

Figure 3.4 The number and time of NEMO complex formation is determined by the extracellular environment

(A) Maximum intensity projections from high-frequency 3D time-lapse imaging experiment of cells exposed to IL-1 (100 ng/ml). Colored lines in overlay indicate tracks for individual EGFP-NEMO complexes over time. On average, 60 to 75% of detected complexes are associated with a track of significant length (figure B4 A). Scale bar, 20 μm. (B) Time courses of fluorescence intensity for single-tracked EGFP-NEMO complexes in cells stimulated with indicated conditions in a microfluidic cell culture system (45). Two representative single-complex trajectories are indicated in each condition (dark orange and dark blue lines). (C) Bar graphs for the average number and the time of formation for tracked EGFP-NEMO complexes. On average, 10 cells were analyzed in each condition. Error bars represent the SEM.

where growth for certain types of ubiquitin polymers is spatially limited, or intact portions of large ubiquitin chains are clipped off en bloc or through endo-cleavage [118], leading to greater inter-spot variability. In nearly all cases, the coefficient of variation (CV) values for distributions of

single-spot descriptors indicate that noise is lower than a Poisson processes (Figure B7). Together, our results suggest that dynamics of NEMO-recruiting protein complexes are strictly regulated for each cytokine response.

3.2.5 Negative feedback on NEMO complexes is primarily independent of transcription

NF-κB-mediated expression of A20 and subsequent deubiquitinating (DUB) activity against NEMO-recruiting complexes constitute an essential negative feedback motif in inflammatory signaling [41]. Within tens of minutes, it's feasible that nascent A20 contributes to the decay phase of EGFP-NEMO spot numbers observed in whole-cell measurements (Figure 3.2 E) thereby reducing IKK activation as observed in cell population assays [49, 137]. It was therefore unexpected that the decay phase for single EGFP-NEMO tracks is visible within several minutes of stimulation, which is remarkably fast for a feedback mechanism governed by transcription and translation (Figure 3.4 B and B7).

To understand how different mechanisms of negative feedback impact trajectories of single EGFP-NEMO spots, we developed a model using ordinary differential equations. Here, cytokine stimulation induces formation of single spots at different times and each spot becomes larger and brighter with Michaelis-Menten kinetics to approximate ubiquitin polymer growth and EGFP-NEMO recruitment. The model considers two sources of negative feedback that act on NEMO-recruiting complexes by enhancing their disassembly rates. The first source aggregates the sum of NEMO-recruiting complexes to drive expression for an A20-like negative feedback mediator ('transcriptional feedback'; Figure 3.5 A). The second source considers the impact from basal expression of A20 and other DUBs in resting cells before stimulation ('basal feedback'; Figure 3.5

A). For both sources, the strength of negative feedback on each NEMO-recruiting spot increases with size to mimic DUB recruitment to ubiquitin polymers in the complex.

Using simulations to vary the strength for each source of negative feedback, their respective impacts on single-spot dynamics was apparent (Figures 3.5 B and B8). By increasing the strength of basal feedback, the decay phase for single-spot trajectories became steeper, and each spot displayed a sharp peak of intensity that was similar between spots regardless of when they form. By contrast, even though transcriptional feedback also increased steepness of the decay phase, the peak intensity of spots that form earlier were significantly greater than spots that formed later. For both sources, increasing strength of negative feedback reduces the overall peak height for all simulated spots (Figure B8).

Based on simulations, if transcription is the predominant source of negative feedback, then spots that form later after cytokine stimulation are predicted to have lower maximum intensity, shorter track length, and smaller AUC (Figures 3.5 B and B8). To test the prediction, we performed a reverse time-course experiment where imaging started after a delay relative to the time of cytokine stimulation (Figure 3.5 C; 0, 5, 10, 15 minutes). Only new spots that formed within the first two minutes were tracked for each condition, thereby enabling direct comparison of early versus late-forming spots and minimizing effects of photobleaching. Biological replicates revealed that early- and late-forming single spot trajectories share highly similar dynamics (Figures 3.5 B and C, and B9), suggesting that transcriptional feedback is dispensable in regulation of dynamics for CI-like complexes. We therefore repeated reverse time-course experiments in the presence of cycloheximide (CHX) to prevent translation of NF-κB-regulated genes, effectively breaking the transcriptional negative feedback loop. To verify that CHX inhibited protein translation, time-courses of nuclear NF-κB were also measured in the same cells during co-stimulation with IL-1

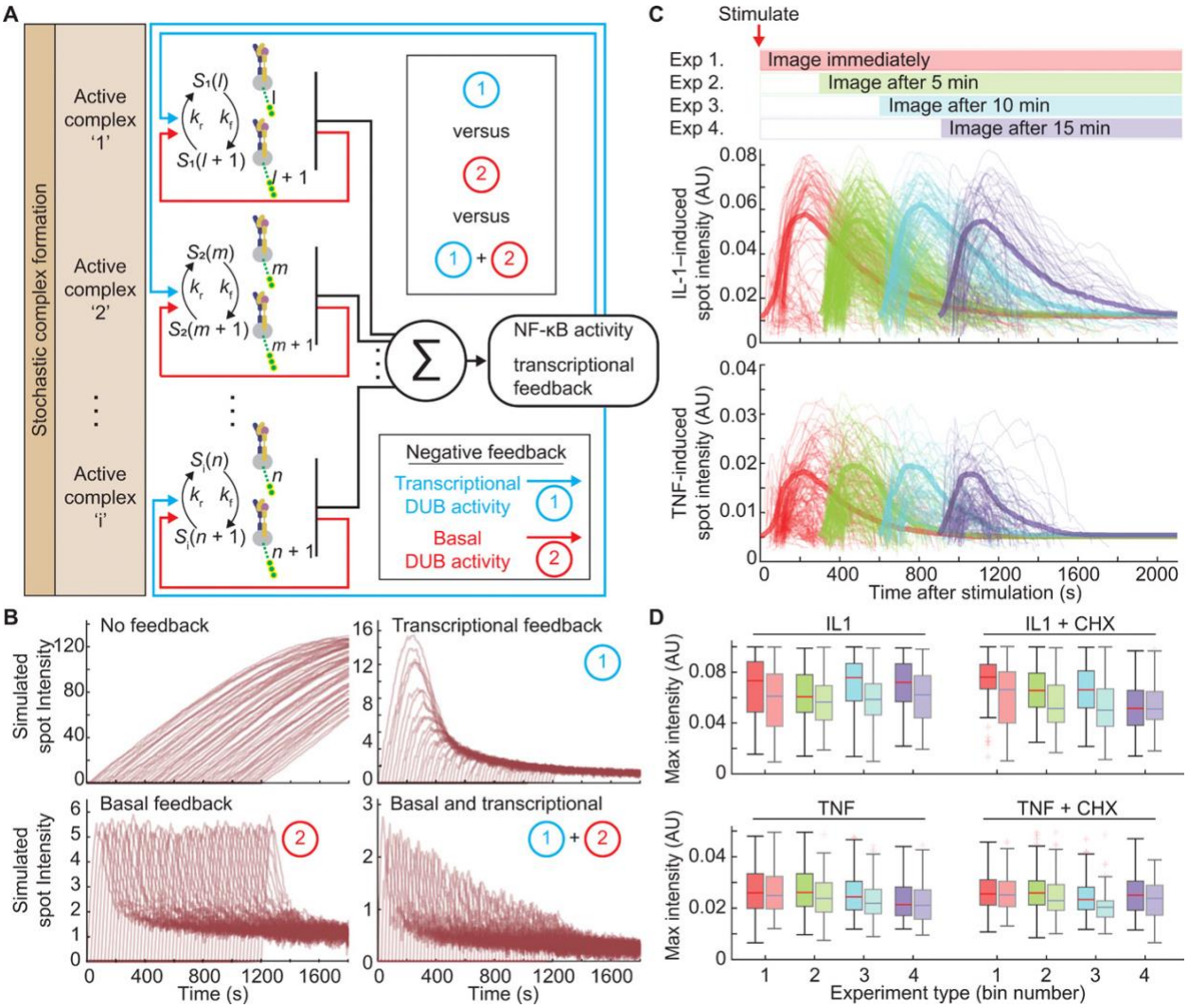

Figure 3.5 The primary NEMO response is independent of the transcriptional feedback loop

(A) Schematic of the HyDeS model of basal (red arrows) and transcription-dependent (blue arrows) feedback regulation of NEMO complexes. Each growing CI-like complex will recede with rates that depend on recruitment of DUB enzymes. (B) Simulations of individual EGFP-complex trajectories using the model in Figure 3.5 A, considering no feedback (top left), transcription-dependent feedback only (top right), basal feedback only (bottom left), or combined transcriptional and basal feedback (bottom right). (C) Schematic of reverse time-course experiments. Only new EGFP-NEMO complexes that form within the first 2 min are tracked in movies from each high-frequency imaging experiment. Cells were stimulated with 100 ng/ml concentrations of either IL-1 (top) or TNF (bottom). (D) Boxplots of maximum intensity of individual EGFP-NEMO complex trajectories after stimulation with IL-1 (top) or TNF (bottom) in cells pretreated for 20 min with media plus dimethyl sulfoxide (left)

or CHX (right). Costimulation with CHX does not significantly increase values for single-spot descriptors as predicted by the transcriptional feedback model (see also figure B5). Median and interquartile ranges are indicated, and biological replicates are shown side by side with increased transparency for each experiment.

and CHX. NF-κB showed persistent nuclear localization in these cells indicating a disruption of the negative feedback loop mediated by IκBα protein expression (Figure B10). Remarkably, loss of transcriptional feedback did not increase features of single spot trajectories as predicted by the transcriptional feedback model (Figures 3.5 D and B8). These results demonstrate that transcription is not the predominant mechanism of negative feedback on NEMO recruitment at CI-like complexes in the timescale of the primary cytokine response.

3.2.6 The IKK-NF-κB signaling axis has the architecture of a stochastic pooling network

When TNF and IL-1 responses are considered separately, trajectories of EGFP-NEMO spots are highly similar regardless of when they form during a cytokine response. This observation argues that each complex behaves as an independent switch, that when activated recruits a quantized amount of NEMO over its lifespan. To understand information transmission properties of the IKK-NF-κB signaling axis, we abstracted the system into four phases (Figure 3.6 A). Detection (‘i’), where parallel and independent CI-like switches that provide redundant measurements of the same extracellular signal (S). Switching (ii) and amplification (iii), when a CI-like complex (CI) activates in response to S, it amplifies with a ligand-specific and quantized gain (G_L) of NEMO activity. The total cellular response (R) in terms of NEMO activity and subsequent NF-κB translocation is the summation (iv) of all amplifier gains in a cell, also referred to as ‘signal pooling’. Although our live-cell data support independent binary switches, quantized

amplification, and signal pooling of IKK into NF-κB (Figures 3.3, 3.4, and 3.5), conditions for detection (i) and switching (ii) remained ambiguous because of cell-to-cell heterogeneity.

The average number of NEMO spots within cells increases with cytokine concentration, yet, we see significant differences between single-cell responses in all conditions (Figure 3.2 F). To determine whether some cells are predisposed to stronger responses, or whether noise at the level of CI formation are predominant contributors to heterogeneity, we exposed cells to two sequential pulses of cytokines. Two-pulse experiments that compare the same cell in different conditions can be used to interpret the impact of stochastic noise on cell-to-cell heterogeneity [47, 52, 79, 111, 138]. For these experiments, cells were first stimulated with a short low concentration reference pulse of cytokine followed by a nearly saturating concentration of cytokine to estimate the maximum number of CI complexes (CI_{max}) that each cell can produce (Figure 3.6). In cells exposed to the same cytokine for both stimuli, the rank ordering of single cell responses to the reference stimulus is strongly correlated with CI_{max} for the same cell (Figure 3.6 C; Spearman $\rho > 0.70$, p-value $< 10^{-10}$). We then asked whether the correlation was due to shared mechanisms downstream of TNF and IL-1 receptors in cross-pulse experiments where cells are exposed sequentially to both cytokines. Same-cell correlations in cross-pulse experiments were greatly reduced with marginal to non-significant p-values (Figure B11). These data suggest that cells are predisposed to different responses based on cell-to-cell variability in receptor-specific components of CI-complexes.

Taken together, our data are consistent with the architecture presented in Figure 3.6 A. Here, the number of CI_{max} is receptor-specific and varies between single cells, and the cell's

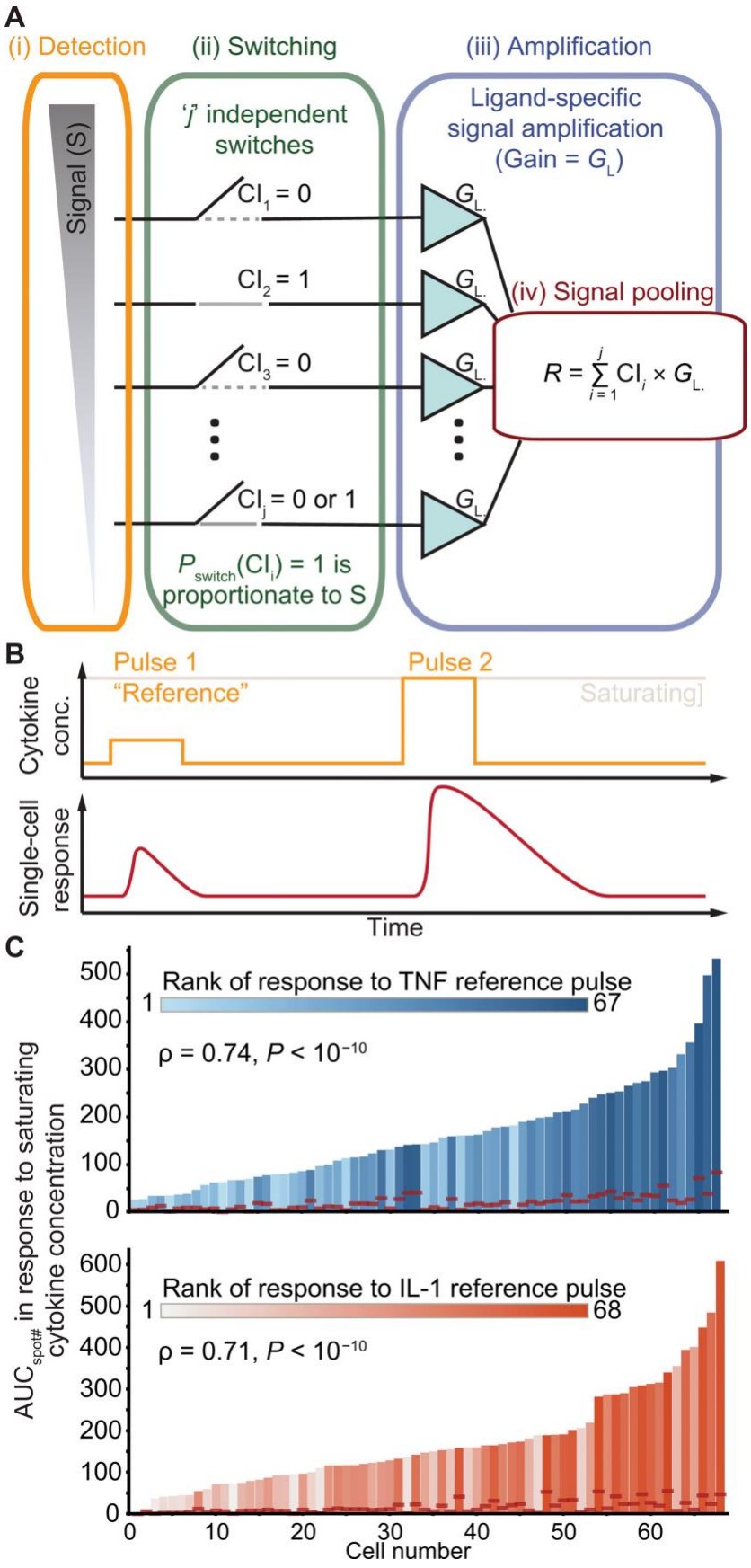
A
(i) Detection
(ii) Switching
(iii) Amplification
Signal (S)
'j' independent switches
Ligand-specific signal amplification (Gain = G_L)
$CI_1 = 0$
$CI_2 = 1$
$CI_3 = 0$
$CI_j = 0$ or 1
G_L
(iv) Signal pooling
$R = \sum_{i=1}^{j} CI_i \times G_L$
$P_{switch}(CI_i) = 1$ is proportionate to S
B
Pulse 1
"Reference"
Pulse 2
Saturating]
Cytokine conc.
Single-cell response
Time
C
Rank of response to TNF reference pulse
1
67
ρ = 0.74, $P < 10^{-10}$
Rank of response to IL-1 reference pulse
1
68
ρ = 0.71, $P < 10^{-10}$
$AUC_{spot\#}$ in response to saturating cytokine concentration
0
100
200
300
400
500
600
0
10
20
30
40
50
60
Cell number

Figure 3.6 Switch-based CI activation in the VG-SPN is governed by cell-intrinsic properties

(A) The VG-SPN consists of four phases: detection, switching, amplification, and signal pooling. For detection, each CI-like complex (CI) is modeled as one of "j" independent switches with an activation probability proportionate to the signal strength. During switching and amplification, each activated switch amplifies the signal with gain "GL," related to the number of NEMO molecules recruited by each CI-like complex. Subsequently, NEMO from each CI-like complex is added to the cytoplasmic "pool" of activated signaling molecules. (B) Schematic for a two-pulse experiment. Cells are first exposed to a short- and low-concentration reference pulse of cytokine. Subsequently, the same cells are exposed to a second pulse of cytokine at saturating concentrations intended to reveal the maximum number of CI complexes that can be generated by each cell (CImax). (C) Single cells are rank ordered by their response to reference cytokine stimulation and correlated with their CImax values. Responses to TNF (top) and IL-1 (bottom) are shown. Inset numbers indicate Spearman's rank correlation (ρ) and associated P values (see also fig. S11).

response to a sub-saturating 'S' is fractional to its CI_{max}. Together with same-cell NEMO and RelA data, our results support a generalization of cytokine-IKK-NF-κB signaling that is evocative of a stochastic pooling network (SPN), a model sensory system with noise-mitigating and information-compressing properties [139]. An important difference, however, is that while binary detectors in an SPN transmit on-off measurements about an information source, each NEMO-recruiting complex performs amplification with a gain determined by the cytokine-receptor-complex identity. Henceforth, we refer to the network architecture as a variable gain SPN (VG-SPN).

3.2.7 Stochastic pooling mitigates noise and fine-tunes response magnitude at the expense of information

Identification of the VG-SPN architecture enabled us to conceptually characterize signal transduction properties that could not be measured from single-cell IKK data due to limited experimental throughput. We first considered the impact of the number of CI switches and their associated gains on noise propagation in the resulting VG-SPN. A mathematically-controlled comparison [123, 140] between different network configurations was enabled by assuming each configuration is capable of producing the same maximal steady-state response (R_{max}; Figure 3.7 A). Simulations for different mathematically-controlled configurations of the VG-SPN demonstrated that shot noise associated with signal detection, and noise associated with the signal gain, both fall off rapidly with increasing numbers of CI switches (Figure 3.7 B). Noise from these sources can be mitigated almost completely when cells are capable of forming ~100's-1000's of CI per cell (CI_{max}/cell). Here, noise-mitigation benefits can be attributed to signal parallelization through quantized nodes. For example, gain noise at each CI can be positive or negative, and because each CI is independent, the distribution for noise across all CI in a cell is centered near zero. Summation of signaling through R_{max} in a VG-SPN effectively averages the contribution of noise across all CI/cell, which is ideally zero assuming sufficient parallelization and absence of other biases. See also Materials and Methods for similar description of shot noise mitigation.

Next, we explored the information transmission properties for different VG-SPN configurations by calculating their channel capacities [51]. We assessed the VG-SPN model using parameters obtained from our single-cell IKK data and simplifying assumptions about distributions for CI properties (see Methods for details, and hyperparameter tuning in Figure B12). For these simulations, CI_{max}/cell and amplifier gain G_L were allowed to vary independently. Consistent with

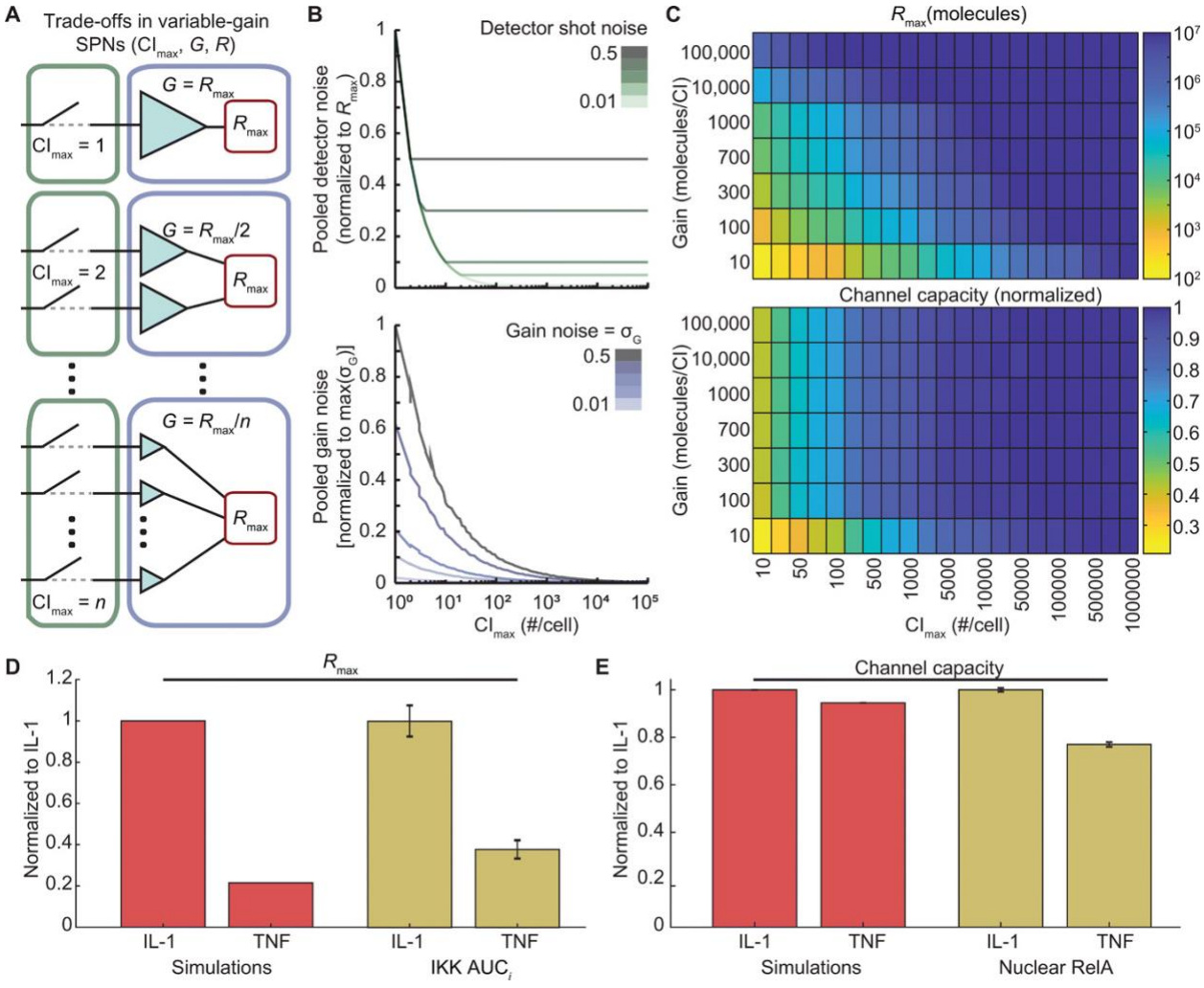

Figure 3.7 VG-SPNs generate trade-offs between noise mitigation, response magnitude, and information transmission

(A) Different configurations of the VG-SPN. For a mathematically controlled comparison, CI and "GL" are adjusted so that each configuration can achieve the same Rmax. (B) Detection introduces shot noise (top), where a switch activates erroneously with a probability given by the SNL. Because each CI is independent, shot noise is mitigated through parallelization via multiple CI until a "noise floor" is achieved. The noise floor is determined by the shot noise value. Variability in the gain from each CI switch (bottom) introduces noise during transmission. Gain noise is effectively averaged and approaches zero via parallelization of independent switches. (C) Rmax (upper limit was set to 10^7 response molecules per cell) and relative channel capacity corresponding to different VG-SPN configurations (see also fig. S12). The VG-SPN architecture provides ligand-specific tunability of response magnitude and

robustness to noise. (D) Simulations (red bars) of the Rmax expected for IL-1 and TNF responses based on experimental values (tan bars) for CImax and Gain. Experimental Rmax is measured as the AUC of NEMO spot intensity in cells exposed to 1000 ng/ml of cytokine as indicated. (E) Simulations (red bars) of the channel capacity expected for IL-1 and TNF responses based on experimental values for CImax and Gain. Experimental channel capacities (tan bars) calculated downstream of NEMO via nuclear RelA dose-response dataset (see also fig. S13). All error bars represent SEM.

our previous analysis for noise-propagation in VG-SPNs, when G_L is greater than 10 molecules per complex the channel capacity increases with the number of CI_{max}/cell and rapidly approaches saturation (Figure 3.7 C, bottom). The maximum channel capacity was found to be 2.5 bits with the model calibrated to live cell data (Figure B12), suggesting a theoretical maximum for information transmission at the level of CI. However, for G_L values of 10 or lower, the system requires orders-of-magnitude more CI_{max}/cell to reach comparable channel capacity values. We also calculated the maximum response (R_{max}) which shows an inverse linear relationship, where different configurations of CI_{max}/cell and G_L can achieve activation of the same number of response molecules up to arbitrarily high numbers (Figure 3.7 C, top).

To test predictions of the VG-SPN, we first simulated R_{max} values expected for TNF and IL-1 responses estimated from experimental G_L and CI_{max} values (Figures 3.2 and 3.7 D). We found that these values were consistent with AUC_i values for NEMO in cells exposed to 1000ng/mL of either cytokine (Figure 3.7 D). Next, we similarly estimated channel capacity values expected for TNF and IL-1 responses. Even though the response magnitude of IL-1 significantly greater than for TNF (Figure 3.7 D), the VG-SPN model predicted that the system would be robust to variation in G_L and CI_{max} values, and the channel capacity for TNF will be only marginally smaller (Figure 3.7 E). Since throughput for NEMO imaging experiments is insufficient for

channel capacity calculations, we instead measured the channel capacity downstream using dynamics of nuclear RelA (Figure B13) as a system output [51, 52]. Model predictions were again remarkably similar with the experimental channel capacity (Figure 3.7 E). Taken together, the VG-SPN motif generates trade-offs, and although the motif results in hard limits for the information content of a signaling pathway, it is also parsimonious and robust to stochastic noise and cell-to-cell variability in protein abundances.

3.3 Discussion

Endogenously expressed EGFP-NEMO is a multifaceted reporter that reveals several aspects of signal transmission. At the level of detection, there is agreement between numbers of EGFP-NEMO puncta induced by saturating cytokine concentrations and average surface receptor numbers in U2OS cells (Figures 3.1 and 3.2). Similarly, the timing of formation of EGFP-NEMO puncta establishes when ligand-receptor-adapter assemblies become capable of signaling in the cytoplasm. Continuous stimulation experiments show that most EGFP-NEMO spots form within 5-10 minutes, indicating that cytoplasmic components of CI-like complexes are not limiting. However, in cells exposed to a short pulse, new spots form up to 30 minutes following cytokine removal, demonstrating variability in timing for receptors to assemble into a signaling-competent stoichiometry. In the cytoplasm, spot intensity time-courses inform about biochemical interactions and feedbacks linked to signal amplification. Here, families of different ubiquitin ligases, kinases, and DUBs engaged at CI-like structures establish rates of EGFP-NEMO recruitment and dissolution. Distinct properties between puncta initiated by different receptor superfamilies (Figures 3.2-3.5) suggest that various adapters and ubiquitin requirements associated with different

types of CI-like complexes will determine cytokine-specific signal amplification [34-36, 117, 118]. We therefore expect endogenous EGFP-NEMO will be valuable in unraveling these upstream mechanisms of inflammatory signaling, similar to reporters for NF-κB that have contributed richly for well over a decade.

Notably, imaging requirements for EGFP-NEMO limit experimental throughput, in particular for spot tracking experiments that require both high magnification and high frequency time-lapse. Although dynamical properties of NF-κB signaling are important mediators of information transmission, analyses that calculate information metrics require a large number of single-cell data points [51, 52, 114]. Consequently, our analysis of EGFP-NEMO required simplifications through coarse-grained scalar descriptors that summarize dynamic properties of NEMO-recruiting complexes and nuclear RelA localization in the same single cells. Our analysis revealed two descriptors of EGFP-NEMO that are strong determinants for descriptors of RelA that were previously shown to carry the most information about cytokine concentrations in the milieu [52]. As technologies emerge that enable data collection for calculation of information metrics between both reporters in the same cell, determination is likely to improve. However, it is also rational that the aggregate sum of NEMO in CI-like complexes during a primary cytokine response is a strong same-cell determinant of the accumulated NF-κB response. This deterministic relationship may therefore remain among the strongest in coming years, providing a read-out for signaling flux and disease-associated perturbations at the level of CI.

Induction of A20 transcription is considered a defining negative feedback in the NF-κB response [10, 34, 49]. However, tracking experiments revealed that trajectories of early and late-forming EGFP-NEMO spots are remarkably similar and insensitive to CHX (Figure 3.5). Although this does not preclude non-catalytic roles for A20 in regulation of IKK [45], it

demonstrates that each CI-like complex is independent and not influenced by transcriptional feedbacks from complexes that form earlier during a response in the same cell. Our data therefore support another proposed role, where transcriptional feedback via A20 is not primarily directed at the initial immune response but instead establishes a new baseline for tolerance to subsequent stimuli [137]. Taken together, signal amplification and negative feedback at each CI-like complex is determined predominantly by the resting cell state.

Abstraction of our experimental observations revealed a VG-SPN signaling architecture (Figures 3.5 and 3.6). The resulting model enabled us to investigate *in silico* the emergent properties of IKK-NF-κB at the level of cytokine detection and signal amplification. With detection and parallel signal amplification at independent CI nodes, our model revealed that noise is effectively mitigated with 100's - 1000's of signaling complexes, and greater numbers have diminishing returns per complex for information transmission. Further benefits to signal transmission through a CI amplifier allow cells to fine tune numbers of activated cytoplasmic signaling molecules, which are significantly more abundant than cytokine receptors at the cell surface. For NF-κB signaling, high-gain amplification enables a large repertoire of receptors to engage the same cytoplasmic pool of IKK with limited occupancy of space at the cell surface. Cells can therefore favor parsimony in receptor numbers, or increase receptor numbers with reduced amplification gain, to interface with the same size pool of signaling molecules while preserving information transmission. These trade-offs provide orthogonal controls to robustly fine tune or diversify response sensitivity to stimuli, as shown here for different cytokines.

3.4 Methods

See full text online for additional data, tables design files, and videos:

https://doi.org/10.1126/sciadv.abi9410

3.4.1 Cell Culture

Parental KYM1 (female), HeLa (female), and U2OS (female) cell lines were obtained from ATCC, and HeLa cell line stably expressing scFv-GFP and tdPCP-tdTomato were a kind gift from Dr. Xiaowei Zhuang from Harvard University [136]. All cell lines were cultured in RPMI (KYM1), DMEM (HeLa), or McCoy's 5A (U2OS) media at 37°C and 5% CO2. All media were supplemented with 10% Corning Regular FBS, 100 U/mL penicillin, 100 µg/mL streptomycin and 0.2mM L-glutamine (Invitrogen). Cells were periodically monitored for mycoplasma contamination.

3.4.2 Quantitative Flow Cytometry

Fluorescence-activated cell sorting (FACS) analysis of samples and PE-beads were performed in a BD LSRFortessa machine (University of Pittsburgh-Department of Immunology Flow cytometry facility). We used Phycoerythrin (PE)-conjugated beads (BD Biosciences, Cat. # 340495) and PE-conjugated antibodies against the following human proteins were obtained from R&D systems: TNFR1 (FAB225P), TNFR2 (FAB226P), IL1R1 (FAB269P), IL1R2 (FAB663P), IL1R3 (FAB676P), polyclonal goat IgG PE-conjugated (IC108P) and mouse IgG1 PE-conjugated

(IC002P). Cells were maintained and used between 5-15 passages. For de-attaching cells from plates, we use 2 mM EDTA in cold PBS. Forty-eight hours before staining 1-2x10^5 cells were plated in 6-well plates. On the day of the staining cells were de-attached from the plate, transferred to polypropylene microtiter tubes (2681377, Fisherbrand™), and maintained on ice during the entire process. Fc-receptors were blocked using human BD Fc block antibody (564219) for 10-15 minutes in the dark. Next, cells were washed with 2% FBS in PBS (FACS buffer) and incubated with primary antibodies for 1 hour at 4°C in the dark. Next, samples were washed twice, and resuspended in 1 ug/mL DAPI (Cat#: D1306, Invitrogen) in FACS buffer between 0.5-1.5 hours before data acquisition. Data analysis was performed using FlowJo™ (BD, version 10.6.1_CL). Samples stained with PE isotype controls were used to set the background fluorescence by subtracting their mean fluorescence intensity (MFI) to the MFI of samples stained with specific antibodies. Next, we used the MFI from PE-conjugated beads to estimate the number of PE molecules on the surface of each cell. All these antibodies have been previously used to estimate surface receptors, with accepted 1:1 ratios of PE to antibody molecules [141-143].

3.4.3 Fixed-cell Immunofluorescence

U2OS WT and U2OS cells stably overexpressing NEMO cells were seeded into plastic flat bottom 96-well imaging plates 24 hours before cytokine treatment at a density of 7000 cells/well. On the day of the experiment, wells receiving IL-1 or TNF (10 ng/mL or 100 ng/mL, respectively) were stimulated 45 min prior to fixation. Pre-warmed 15X cytokine mixture was spiked into wells and mixed. After treatment and before fixation the cells remained in environmentally controlled conditions (37°C and 5% CO2). Cells were fixed with 4% PFA and permeabilized using 100% methanol for 10 minutes each with one PBS wash in between, and three PBS-T (PBS 0.1% Tween

20) washes at the end. Next, cells were incubated in primary antibody solution (3% BSA in PBS-T) with 1 μg/mL of both α-RELA (sc-8008; Santa Cruz) and NEMO (sc-8330; Santa Cruz) at 4°C overnight. The following morning, cells were washed three times with PBS-T and incubated for 1 hour at room temperature with secondary antibody solution in 3% BSA in PBS-T (4 μg/mL of both goat anti-Mouse IgG Alexa Fluor 647 (A21235; Thermo) and goat anti-Rabbit IgG Alexa Fluor 594 (A11012; Thermo). After incubation, cells were washed twice in PBS-T and incubated in 200ng/mL Hoechst in PBS-T for 20 min. Finally, wells were washed in PBS-T and left in PBS to keep cells hydrated during imaging. Cells were imaged using Delta Vision Elite imaging system at 20x magnification with a LUCPLFLN objective (0.45NA; Olympus).

3.4.4 Fixed Cell Image Analysis

Using Cell profiler (www.cellprofiler.org, [144]), cell nuclei were segmented using the Hoechst channel labeling DNA. Next, secondary segmentation was performed using EGFP-NEMO channel to define the cellular boundaries. The output of cell segmentation was compiled and analyzed using custom scripts in MATLAB (Mathworks, R2019b).

3.4.5 Establishing EGFP-NEMO/mCherry-RELA CRISPR Double Knock-in Cells

Single knock-in U2OS cell lines expressing EGFP-RELA/NEMO were generated previously using CRISPR-Cas9 technology as described in reference [37]. To generate double Knock-in cells, we assembled the RELA repair template consisting of DNA sequences for a left homology arm (LHA −544 bp, chromosome 11_65663376–chromosome 11_65662383) followed by a mCherry protein coding sequence with a start codon but no stop codon and a sequence

encoding 3x GGSG linker in-frame with the right homology arm (RHA +557 bp, chromosome 11_65662829–chromosome 11_65662276) from plasmids synthesized by GeneArt. Synonymous mutations were introduced to prevent interaction of the repair template and Cas9. Next, single EGFP-NEMO Knock-in U2OS cells were seeded in 6-well plates (2 x 10^5 cells) and transfected next day with pSpCas9n-(BB)-2A-Puro-RELA_gRNAs and Bgl2-linearized mCherry-RelA repair template donor plasmid. A ratio of 3.5:1 FuGENE HD (Promega) to total DNA was used for transfection of 4 µg of DNA. Plasmids generation, and CRISPR modifications were all based on Ran et al. 2013 [145].

3.4.6 Live-cell Imaging

Live cells were imaged in an environmentally controlled chamber (37 °C, 5% CO2) on a DeltaVision Elite microscope equipped with a pco.edge sCMOS camera and an Insight solid-state illumination module (GE). For detection of NEMO spots, U2OS cells expressing fluorescent protein (FP) fusions of RELA and NEMO were seeded at a density of 15,000 cells/well 24 h prior to live-cell imaging experiments on no. 1.5 glass bottom 96-well imaging plates (Matriplate). Medium was changed to phenol red-free FluoBrite Dulbecco's modified Eagle's medium (Gibco, A18967–01) between 30 min to 2 h before imaging. For detection of NEMO spots, live cells were stimulated with the indicated concentrations of TNF or IL-1. After cells adapted in the environmentally controlled chamber, we collected eight z-stack images of 0.5 µm separation in the Alexa Fluor 488 channel with an exposure of 0.04 sec and a transmission of 32%. Using these stacks of images, we reconstructed NEMO spots in 3D using image J (for display) and dNEMO (more details in "Punctate Structures Detection and Quantification" section). To test our different hypothesis, we performed two types of time-lapse imaging experiments: long-term and short-term

high-frequency imaging. Images were collected over at least 3 fields per condition with a temporal resolution of 2 min per frame for long-term and 10 seconds per frame for short-term high-frequency imaging experiments. Wide-field epifluorescence and DIC images were collected using a ×60 LUCPLFLN objective. For all treatments, cytokine mixtures were prepared and pre-warmed so that addition of 120 µL added to wells results in the indicated final concentration.

For 2-pulse experiments, cells were exposed to a 1-minute dilute 'reference pulse' of either TNF or IL-1, selected from calibration experiments to produce a subtle response in most cells (2 and 5 ng/ml for TNF and IL-1 respectively), followed by a 'saturating pulse' of 500 ng/mL for same-cell comparisons. Cells were washed once with pre-warmed fresh media during media swaps. Since EGFP-NEMO foci form and disperse rapidly after treatment, a 30-minute recovery period was selected between 'reference' and 'saturating' pulses. The short recovery period also minimized the effects of photobleaching which were apparent within 60-90 minutes of imaging.

For small molecule inhibitors experiments to study the nature of the NEMO spots, we pretreated cells with 178 µM CHX, 50 µM MDC, or 20 µM Dynasore for 20 minutes before adding cytokine on top of the medium with inhibitor.

For dose-response experiments to calculate channel capacities using live-cell imaging data, U2OS cells were prestained with Hoechst 33342 (300 ng/ml) for 1 hour. Following the incubation with Hoechst, all growth medium contained trace amounts (60 ng/ml) of Hoechst to maintain the nuclear stain and assist with segmentation. Cells were then treated with six different doses of TNF or IL-1 (1000, 100, 10, 1, 0.1, and 0.01 ng/ml) plus a control of 0 ng/ml. After treatment, cells were imaged at the temporal resolution of 5 min per frame with a 20× LUCPLFLN objective.

3.4.7 Live Cell Imaging in Microfluidic Devices

Microfluidic device fabrication and operation was done as described previously [46]. Briefly, dynamic stimulation devices of two inlets and one outlet were made with PDMS (Sylgard), autoclaved, washed with ethanol, and incubated with a solution of 0.002 v/v fibronectin in PBS for 24 hours at 37 °C. After incubation, excess of fibronectin was flushed with tissue culture media multiple times. Between $3x10^6$ and $8x10^6$ cells/ml were seeded by inserting 200 µl pipette tip in the outlet port. The outlet port was plugged with PDMS plugs after reaching a cell density for approximately 60% confluence. The device was incubated for at least 24 hours and PDMS plugs at the outlet were then replaced with pipette tips filled with medium. On the day of the experiment, tygon tubes (Fisher Scientific 1471139) were attached to the device with the other end connected to basins with media or cytokine treatment. The basins were then placed on corresponding platforms on the gravity pump and the attached tygon tubes were clamped. The device was then fitted to a custom adapter and placed under the microscope for imaging. The clamps on the tubes were removed at the beginning of the experiment. Cells were stimulated with desired pattern of cytokine stimulation (pulse, ramp or continuous) by changing the heights of basins by controlling corresponding stepper motors through custom codes uploaded on the Arduino mega 2560 microcontroller. The cytokine treatment was prepared with Alexa647-conjugated BSA (0.0025 v/v; Invitrogen) and imaged with CY5 filter to confirm the corresponding stimulus pattern. Images were collected under same conditions as previously described for live-cell imaging.

3.4.8 Punctate Structures Detection and Quantification

EGFP-NEMO and SunTag polysome spots were detected and quantified using our application dNEMO [146]. Briefly, dNEMO is a computational tool optimized for measurement of fluorescent puncta in fixed-cell and live-cell time-lapse images. The user-defined threshold for spot detection in dNEMO was set between 1.5 and 2.0 for all images. Reported pixel values for puncta were individually background-corrected by averaging pixels from an annular ring surrounding each spot. The width and offset for the annular ring were both set to 1 pixel. We furthermore stipulated that puncta must appear in at least 2 contiguous slices of the 3D images (out of 8 slices) to be considered valid. The same user parameters were applied to all images and single cells were manually segmented using dNEMO's keyframing function. For each single cell, spot features were measured for each new spot that formed following stimulation, yielding sets of single-cell spot features over time. NEMO puncta flat-field and background-corrected images were prepared for display using ImageJ.

3.4.9 Tracking of Individual NEMO Spots

The location and intensity data of EGFP-NEMO spots obtained with our dNEMO software [146] was used for single-spot tracking using the uTrack package in MATLAB [147]. The hyperparametrs in the uTrack package were adjusted to enhance tracking performance for TNF and IL-1 induced spots. Specifically, the time gap window was lowered to 3 frames and the gap penalty was lowered to 1 from their default values of 5 and 1.5 respectively. The minimum length of tracks segments used for gap closing was increased to 3 frames from the default of 1 frame. The merging and splitting events were considered while tracking. Properties of individual spots

(intensity, size etc.) were then associated with tracking data to generate single-spot trajectories for each spot property. Trajectories lasting for less than 3 minutes were excluded from further analyses. With these settings, approximately 60% and 75% of spots respectively for TNF and IL-1 responses were tracked and included in subsequent analysis (Figure B7 A). Three main features were obtained from each single-spot trajectory:

1. Maximum intensity or Max_i (peak intensity of a single-spot trajectory)
2. Integrated intensity or AUC_i (sum of spot intensities at all time-points in a trajectory)
3. Track length (trajectory length i.e. time for which the spot is tracked)

Features of single-spot trajectories were then compared for dynamic stimuli experiments involving different cytokines across different cells (Figure B7); and for spots formed at different time-windows in reverse time course experiments (Figures 3.5 D and B9).

3.4.10 Estimating Number of NEMO Molecules per NEMO Spot via Calibration with SunTag Labeled Polysomes

To quantify the number of NEMO molecules within each NEMO complex (spot), the CRISPR labeling of NEMO with EGFP allows us to infer the number of NEMO molecules by counting GFP molecules and converting with 1:1 ratio. In counting GFP molecules in NEMO puncta, we utilized the live cell translation reporter developed by Wang et. al, [136] to calibrate the relation between GFP counts and measured GFP intensity and imaged it in HeLa cells with the same imaging condition used for NEMO in U2OS EGFP-NEMO cells.

During translation, one mRNA binds to multiple ribosomes simultaneously and form a large polysome complex. We assume that the positioning of each ribosome on mRNA independently satisfies a uniform distribution. The signal intensity of each fluorescence foci in the

cytoplasm, representing the translating polysomes, varied depending upon the total number of ribosomes and the location of each ribosome on mRNA. When ribosomes reach the region after the coding sequence for the SunTag peptide, the intensity would be the maximum for fully assembled complex; when ribosomes are halfway towards the end, the signal would be approximately half maximal. To account for this variability, we used Monte Carlo simulations to randomly sample the positions of ribosomes and generate the distribution of numbers of SunTag peptides being produced when there are n ribosomes present on single mRNA, denoted by p_2 (m,n), where m is the number of SunTag. n, as the number of total ribosomes on each mRNA, satisfies Poisson distribution p_1 (n)=e^(-λ) λ^n/n!. The average number of ribosomes for each translation foci is measured to be 12 experimentally [136], therefore we set $\lambda \approx 12$. The possibility of m SunTag peptides being translated on each translation foci are calculated as follows:

$$P(m) = \sum_{n=1}^{+\infty} p_2(m,n)p_1(n)$$

When n is large, p_1 (n) rapidly converges to zero. Therefore, we set n = 30 as the cutoff of the summation.

We quantified the fluorescence intensity of individual translating polysome in HeLa cells using dNEMO [146] with the same threshold used for NEMO quantification in U2OS cells. As the GFP intensity is proportional to the number of GFP molecules, we determined the scaling factor between the measured fluorescence intensity and theoretical distribution of GFP molecule numbers. Here, we used the Nelder-Mead algorithm to minimize the square of difference between the "measured" GFP distribution and theoretical GFP distribution to obtain the scaling factor. To account for effects of photobleaching, we calculated the scaling factors independently for each

frame of the time-lapse image. Using the scaling factor obtained from the translation reporter, the intensity of NEMO spots was converted to numbers of GFP molecules per spot.

3.4.11 Extracting Descriptors from NF-κB Dynamics

Descriptors of the fold-change of the FP-RELA mean intensity trajectories were extracted using custom MATLAB scripts and Image J movie explorer. The fold-change transform is carried out by dividing the FP-RELA trajectories by the initial nuclear fluorescence at the zero-time point. Those descriptors include:

- Area under the fold-change curve (AUC_{Fold}): a summary statistic which approximates the cell's response over time, previously found to carry the most information about a cell's response to cytokine stimulation [52].
- Max fold change (F_{max} / $F_{initial}$): maximum value of the fold-change trajectory, previously found to determine the transcriptional response of cells stimulated with TNF [42].
- Maximal rate of nuclear entry ($Rate_{in}$): slope of line fitted to three data points between time zero and time of maximum fold change. Point along fold-change trajectory at which slope was determined was point where slope had maximal absolute value.
- Maximal rate of nuclear exit ($Rate_{out}$): slope of line fitted to three data points between time of maximum fold change and the end of the fold-change trajectory. Point along fold-change trajectory at which slope was determined was point where slope had maximal absolute value.
- Time of max ($t_{max\ (fold)}$): time at which fold-change is maximum.

- Time of half up ($t_{50up\ (fold)}$): time point at which fold-change trajectory rises to half the max fold change.
- Time of half down ($t_{50down\ (fold)}$): time point at which fold-change trajectory falls to half the max fold change.

3.4.12 Extracting Descriptors from EGFP-NEMO Dynamics

Descriptors of trajectories for the NEMO spot number and NEMO spot intensity were extracted from single cell and single complex data using custom MATLAB scripts. The NEMO spot number trajectory is the number of NEMO spots detected per cell over time, while the NEMO spot intensity trajectory is the integrated intensity of the detected spots per cell over time. Those descriptors (per trajectory) include:

- Area under the curve (AUC): area under the trajectory integrated. For a given cell's NEMO spot number and spot intensity trajectories, this represents either the total number of spots detected, or the total intensity of the spots detected, respectively.
- Maximum value (Max): maximum number of spots / spot intensity for a given cell trajectory.
- Rate of entry ($Rate_{in}$): slope of line fitted to three data points between time zero and time of max. Point along trajectory at which slope was determined was point where slope had maximal absolute value.
- Rate of exit ($Rate_{out}$): slope of line fitted to three data points between time of max and the end of the trajectory. Point along trajectory at which slope was determined was point where slope had maximal absolute value.
- Time of max (t_{max}): time at which the NEMO spot trajectory trajectory is maximal.

- Time of half up (t_{50up}): time at which the NEMO spot trajectory rises to half the maximum value.
- Time of half down (t_{50down}): time at which the NEMO spot trajectory falls to half the maximum value
- Full width at half max (FWHM): width of the peak of the NEMO spot trajectory between the time of half up and the time of half down.
- Maximum over area of the cell (Max/Area): maximum value of the NEMO spot trajectory divided by the area of the cell. The cell's area is given by the polygon output from the dNEMO results.
- Fold-change peak difference ($t_{max\ (fold)}$ - t_{max}): difference between the time of maximum fold change and the time of max of the NEMO spot trajectory.

3.4.13 Correlation and Multiple Linear Regression of NEMO and NF-κB Descriptors

Descriptors collected from both the FP-RELA and EGFP-NEMO trajectories were correlated using Spearman's rank and coefficient of determination in linear and log-log scales (see Figure B5). When correlation between a pair of descriptors could not be computed (e.g., an inability to compute some trajectory's $rate_{in}$ or t_{max} in cells that did not respond significantly to stimulation), the single cell was omitted from the affected correlation dataset, but not from the overall set of cell trajectories being analyzed. Multiple linear regression was also applied to the linear and log-transformed descriptors of the cells responding to TNF, IL-1, or the full combined experimental dataset (see Figure B6). Linear correlation and multiple linear correlation of the descriptor sets was carried out using custom MATLAB scripts.

3.4.14 Computational Model (HyDeS) to examine relative effects of basal and transcriptional feedback on NEMO spot dynamics

We modeled the intensity of individual NEMO spots with a hybrid deterministic-stochastic (HyDeS) model. The purpose of this model is to examine the relative effects of basal and transcriptional feedback via DUB molecules on NEMO spot dynamics, and not necessarily to capture precisely the absolute intensity dynamics for EGFP-NEMO at each single spot. Therefore, to directly model the relative effects of basal and transcriptional feedback, we used three main variables. First, we defined the intensity of a spot (I) to represent a continuous approximation for ubiquitin chain size and NEMO activity resulting from molecules recruited at that spot. Second, we defined a variable X_basal for each individual spot as a proxy for feedback due to activity from basal DUBs expressed in resting cells. We modeled the X_basal variable such that the basal feedback increases as the corresponding NEMO spot grows through proportionate recruitment of DUB molecules on the same complex. Third, we defined a variable X_trnsxl to capture the transcriptional feedback due to the aggregate activity of all NEMO spots. Here, transcription-induced DUBs act in the same way as basal DUB molecules.

The model corresponding to N number of NEMO spots consists of 2N+1 ODEs: N for the individual spot intensities (I_i), N for the basal feedback variables corresponding to each spot (X_basal_i) and one for the transcriptional feedback variable (X_trnsxl). For each simulation, we modeled 200 single spots that form at regular intervals to approximate the response of a single cell to cytokine stimulation.

$$\frac{d[I_i]}{dt} = P_{form} * P_{bound} \frac{K_{growth}}{K_{limit} + [I_i]} - Kd_{basal} * X\_lbasal_i * [I_i] - Kd_{trnsxl} * X\_trnsxl * [I_i]$$

$$\frac{d[X\_basal_i]}{dt} = Kx_{basal} * [I_i] - Kxd_{basal} * [X\_basal_i]$$

$$\frac{d[X\_trnsxl]}{dt} = Kx_{trnsxl} * \sum_i [I_i] - Kxd_{trnsxl} * [X\_trnsxl]$$

The variables and parameters in the model are as described in the following tables. We examined the relative effects of the two kinds of feedbacks by varying the parameters Kx_{basal} and Kx_{trnsxl}, which respectively control the amount of local and global feedback, by two orders of magnitudes (Fig. S8).

3.4.15 Variable-gain Stochastic Pooling Network model

Stochastic pooling networks (SPN) are a model sensory system in which noisy detectors are used to make independent and compressed measurements of a signal [139]. These measurements are then pooled to average out the uncorrelated noise and reconstruct the original signal. Here we characterize a SPN system with the decoration of variable-gain (VG-SPN). In the VG-SPN system, each detector amplifies its binary measurement with a 'Gain' before pooling. Thus, the VG-SPN can have different configurations depending on the number of detectors and the Gain per detector. In the context of cytokine signaling mediated by CI complexes, each complex acts as a binary detector of the extracellular cytokine presence and the number of NEMO molecules recruited by a complex is considered its corresponding Gain. Therefore, we define two fundamental variables in our model of VG-SPN system. First, CI_{max} is the number of detectors in a VG-SPN configuration which is given by the maximum number of CI complexes that can form

in a cell at saturation. Second, Gain is the number of NEMO molecules recruited at a given CI complex over the time course of its activity.

Depending on CI_{max} and Gain configurations, VG-SPN systems will have different maximum response (R_{max}) in terms of total number of NEMO molecules recruited. To systematically examine the noise mitigation properties of different VG-SPN configurations, we used a mathematically controlled approach by assuming each configuration is capable of producing the same steady state response (Figure 3.7 A). We therefore fixed the value of R_{max} and defined the Gain per complex to be inversely proportional to the maximum number of complexes as: Gain = R_{max}/CI_{max}. We then varied CI_{max} across orders of magnitude and calculated the noise associated with each configuration (Figure 3.7 B).

The detector shot noise is the fraction of NEMO molecules recruited when a CI complex forms erroneously i.e. in absence of the signal. We assigned the probability of a complex to erroneously form as the 'shot noise level' (SNL). Therefore, the noise propagated when the SNL is less than the uniform probability ($1/CI_{max}$) will correspond to one complex forming erroneously which, in turn, will be the Gain associated with that configuration. For example, erroneous activation of a 1-receptor system via shot noise will activate the system to its fullest capabilities. Due to the inverse correlation of CI_{max} with Gain, the shot noise will decrease with CI_{max} (Figure 3.7 B, top). However, after reaching a certain value of CI_{max}, the SNL will become higher than the uniform probability allowing more than one complexes to erroneously form at the same time. Configurations beyond such value of CI_{max} will hit the noise floor and the shot noise will not decrease further.

$$Fractional\ Shot\ Noise = \begin{cases} \dfrac{Gain}{R_{max}} = \dfrac{1}{CI_{max}}, & when\ SNL < \dfrac{1}{CI_{max}} \\ \dfrac{SNL * CI_{max} * Gain}{R_{max}} = SNL, & when\ SNL > \dfrac{1}{CI_{max}} \end{cases}$$

We observed considerable variability in intensities of NEMO complexes formed in response to a particular cytokine (Figures 3.2 D, 3.5 C and D). This variability suggests that although the mean value of Gain per complex is cytokine specific, the gain associated with a single complex can vary among different complexes within a cell, and these differences will introduce 'Gain noise' in the pooled response. Specifically, Gain noise captures the noise in the pooled response corresponding to same number of active detector complexes due the variability in Gain per complex (i.e. the number of NEMO molecules recruited to a single complex over its lifespan). We examined the effect of different VG-SPN configurations on the Gain noise using the mathematically controlled approached as described earlier. We modeled the Gain per complex with Gaussian distribution and using the coefficient of variation given by the 'Gain noise level' (GNL) as: σ_G = GNL*Gain. Therefore, for a given VG-SPN configuration, each cell will have a response corresponding to the sum of CI_{max} random numbers obtained from the distribution $\mathcal{N}(Gain, \sigma_G)$. We simulated 1000 cells for every configuration with different GNL values and calculated the Gain noise (coefficient of variation) that contribute to the resulting responses (Figure 3.7 B, bottom).

Next, we developed a computational VG-SPN model to generate simulated data for channel capacity calculations using the framework developed by [51] and codes from our previous study [52]. In this model, the signal S in the range (0,1] represents the extracellular cytokine dose where S=1 corresponds to saturating dose. The dose range is equally divided in discrete levels controlled by the hyperparameter 'numDoses'.

$$S_i \in (0,1]\,, i \in [1, numDoses]$$

For each input signal S_i, we simulate responses from N cells, where N is another hyperparameter. The response of 'j'th cell to 'i'th level of input signal (R_{ij}) is a scalar quantity representing the total number of recruited NEMO molecules. The model thus produces simulated data as response vectors of length N for each of the 'numDoses' number of input conditions. The data workflow is as follows:

$$S = \begin{bmatrix} S_1 \\ S_2 \\ \vdots \\ S_i \\ \vdots \\ S_{numDoses} \end{bmatrix} \rightarrow R = \begin{bmatrix} R_1 \\ R_2 \\ \vdots \\ R_i \\ \vdots \\ R_{numDoses} \end{bmatrix} \; where \; S_i \rightarrow R_i = [R_{i1} \quad R_{i2} \quad \dots \quad R_{ij} \quad \dots \quad R_{iN}]$$

As described earlier, CI_{max} is the maximum number of NEMO complexes a cell can form at saturating conditions i.e. when $S_i = 1$. CI_{max} will be related to the number of surface receptors (SR) per cell through the cytokine-dependent valency as: CI_{max} = SR/valency. Therefore, to model cell-to-cell variability in receptor expression (Figure 3.1 B), we assumed that CI_{max} follows a Gaussian distribution over the N simulated cells with coefficient of variation given by the Receptor Noise Level (RNL).

$$CI_{max_j} \sim \mathcal{N}(CI_{max}, RNL * CI_{max})$$

Here the mean CI_{max} is set by the VG-SPN configuration and RNL is another hyperparameter controlling the coefficient of variation in receptor expression. For instance, for N=1000, CI_{max}=100 and RNL=0.3, we sample 1000 normally distributed integer random numbers from $\mathcal{N}(100,30)$ to simulate responses for 1000 cells where each cell can maximally form around 100 complexes with coefficient of variation 0.3.

We used binomial distribution to model switch-like properties of complex formation in the detection and switching steps (Figure 3.6 A) wherein the probability of complex formation (P_{form})

increases with the input signal S_i. We used modified Hill function to relate S_i with P_{form} (Figure 3.2 F).

$$CI^*_{max_j} \sim Binomial\left(CI_{max_j}, P_{form}\right), \qquad where \quad P_{form} = \frac{(1+0.5) * S_i^3}{0.5 + S_i^3}$$

Here $CI^*_{max_j}$ is the number of complexes formed in response to the dose level S_i in a cell having capacity to form CI_{max_j} complexes at saturation. Therefore, for a given 'j'th cell, we generate CI_{max_j} random numbers between [0,1]. We then check how many of those fall below the P_{form} value corresponding to the given signal S_i. This number, $CI^*_{max_j}$, will be used as number of active complexes in the 'j'th cell. Thus, the output of detection step corresponding to signal S_i is the following vector:

$$S_i \rightarrow \left[CI^*_{max_1} \quad CI^*_{max_2} \quad \ldots \quad CI^*_{max_j} \quad \ldots \quad CI^*_{max_{N^\#}}\right]$$

Note that $N^\# \leq N$ because for lower doses there might be some cells that don't cross the P_{form} threshold i.e. they don't form any spots.

In the detection step, we simulated the number of complexes formed by a given cell ($CI^*_{max_j}$) in response to a given dose (S_i). Next, in the amplification step (Figure 3.6 A), we model the Gain (G_k) in terms of number of NEMO molecules recruited per complex. The response of a cell i.e. total number of recruited NEMO molecules is then sum of the Gains associated with all the complexes formed in that cell (signal pooling step, Figure 3.6 A).

$$Response\ R\left(S_i, CI_{max_j}\right) = \sum_{k=1}^{CI^*_{max_j}} G_k$$

We assume a linear relation between Gain per complex (in terms of NEMO molecules) and the experimentally observed integrated intensity (AUC_i, Figure B5).

$$G_k(NEMO\ Molecules) = AUCi\_to\_NEMO\_factor * G_k(Intensity)$$

Here AUCi_to_NEMO_factor is another hyperparameter. As previously stated for calculation of Gain noise, we use Gaussian distribution to model the variability in G_k within a cell.

$$G_k \sim \mathcal{N}(Gain, GNL * Gain)$$

Here GNL is the Gain Noise Level i.e. the coefficient of variation of Gains corresponding to different complexes within a cell. We use the quadratic relation between intracellular mean and variance of AUC_i (Figure B7 E) to get GNL for different mean values of Gain corresponding to different VG-SPN configurations.

To summarize, response of 'j'th cell with a VG-SPN configuration given by (CI_{max}, Gain) to the input signal level S_i is calculated as following:

$$Response\ R_{ij}(S_i, CI_{max}, Gain) = \sum_{k=1}^{CI^*_{max_j}} AUCi\_to\_NEMO\_factor * \mathcal{N}(Gain, GNL * Gain)_k$$

$$Where \qquad CI^*_{max_j} = Count(CI_{max_j} < P_{form}(S_i))$$

$$And \qquad CI_{max_j} \sim \mathcal{N}(CI_{max}, RNL * CI_{max})$$

This process is repeated for N number of cells and 'numDoses' number of input signal levels:

$$CI_{max_j} \in \left[CI_{max_1} \quad CI_{max_2} \quad \dots \quad CI_{max_N}\right]$$

$$S_i \in [S_1 \quad S_2 \quad \dots \quad S_{numDoses}]$$

There are two independent variables in this model, CI_{max} and Gain, which completely define the VG-SPN configuration. In other words, the model allows independent 'tuning' of maximum number of NEMO complexes (i.e. number of surface receptors) and the Gain (i.e. number of NEMO recruited by each complex) to achieve a certain channel capacity.

The model has four hyperparameters: numDoses (controlling number of discrete dose levels), N (number of cells to simulate per dose level), RNL (coefficient of variation in CI_{max} over cells) and AUCi_to_NEMO_factor (relating integrated intensity to number of NEMO molecules per complex). In addition to these four, the channel capacity calculation framework developed by [51] requires another hyperparameter 'K' which controls the K-nn classification to estimate probability densities of response given input dose level. To interface the VG-SPN model with our previous code for channel capacity calculations [52], we adjusted these five hyperparameters to avoid technical biases that can artificially limit calculated channel capacity values for a VG-SPN configuration.

After running preliminary computational experiments, we arrived at a set of values for the five hyperparameters. Then, for each hyperparameter, we varied its value while keeping other values in the set constant to confirm that the chosen value doesn't limit the maximum channel capacity value of a VG-SPN configuration. By iterating through this process several times, and repeating it for multiple values of R_{max}, we converged on the following settings (Figure B12 A).

First, the number of simulated input conditions can artificially limit the channel capacity calculated for a signaling system but becomes increasingly costly to compute when input conditions become excessively high. We simulated our model with 10, 30, 60 and 100 input conditions ('numDoses' parameter in the methods) and found that the max channel capacity does not increase beyond 60. Next, we observed that the max channel capacity decreases as the cell-to-cell variability in number of CI per cell (RNL parameter) increases. We therefore chose the intermediate value of stdR = 0.3 that is consistent with our FACS receptor analysis (Figures 3.1 and B1). Next, the value of K used for K-NN classification introduces minial bias beyond a value of 5 and contributes to computational cost at higher values. We therefore chose K = 5, consistent

with previous calculations [51]. We then found that simulating more than 1000 cells per input condition does not increase the channel capacity but significantly affects simulation time, so we chose N = 1000. Finally, in order to relate amplifier gain (G_L) to the quadratic noise relationship observed in data (Figure B7 E), we estimated the factor to convert integrated spot intensity to number of NEMO molecules at a CI-like complex ('AUCi_to_NEMO_factor'). Values for the conversion factor did not have significant effects on max channel capacity beyond a value of 200.

Once we fixed the hyperparameters of the model, we removed the constraints of the mathematically controlled framework and allowed the two model variables, CI_{max} and Gain, to vary independently. We then calculated the channel capacities corresponding to VG-SPN configurations given by different (CI_{max}, Gain) pairs using previous codes [52] which are based on the framework developed by [51]. We also calculated the maximum response (R_{max}) corresponding to each (CI_{max}, G) configuration which is simply given by CI_{max}*Gain. Effectively, the value of R_{max} relates to the number of NEMO or other response molecules in the cytoplasm that can be activated by a VG-SPN configuration.

3.4.16 Statistical Analyses

Distributions of physical properties of NEMO puncta were compared to see if they were statistically different from one another (Figure 3.2 C). The distributions were compared with a student's t-test (using native MATLAB functions), yielding p-values for the null hypothesis that the two distributions were from the same (normal) distribution, with identical means and standard deviations. Each null hypothesis was rejected at the 5 percent significance level with p-values << 10-20 for every TNF and IL-1 pair with the same dosage condition.

Spearman's rank correlation and linear regression were performed on NEMO predictors for the RELA responses (and the log-transformed predictors/responses) for cells responding to TNF and IL-1. Native MATLAB functions were used to calculate all coefficients. Multiple linear regression was also performed on NEMO predictors for RELA AUC-Fold response in cells responding to TNF and IL-1 to see whether combinations of descriptors improve R2 values. R2 values shown in Fig. S6 are the best R2 determined for the indicated number of predictors when considering all possible predictor combinations. Combination of predictors provided only marginal improvements, with maximum R2 values approaching 0.7 and 0.8 for the linear and log-transformed (respectively).

3.4.17 Channel capacity calculations using live-cell imaging data

The dose-response data with TNF and IL-1 was used to calculate the channel capacities corresponding to the two cytokines. First, nuclear regions stained with Hoechst were segmented using CellPose [55] and then tracked with a custom Python script. For each time point, the mean nuclear intensity from the mCherry-RelA channel was measured for single cell time-course trajectories and used to calculate the fold change as described above. The trajectories of nuclear RelA fold change were then filtered to remove cells that die, divide, or leave the field of view. Thus, we have the dose-response datasets of seven experimental conditions (six cytokine doses and one control) for both TNF and IL-1.

Time-course trajectories from each of the TNF and IL-1 dose-response datasets were then subsampled at 15-min intervals for the first 1.5 hours of response (vector dimension = 6). Subsampled time courses were then used to calculate the channel capacity with our previous code [52], which are based on the method developed by [51]. K = 5 was used for the K-nn probability

density estimation as described in [51]. These calculations were repeated for 20 times to capture the random noise associated with the channel capacity calculation algorithm. Calculated channel capacities for TNF and IL-1 responses were then normalized by the maximum (here IL-1) for qualitative comparison (Figure 3.7 E).

3.5 Author contributions

Conceptualization: JAC, CSM, RECL. Methodology: JAC, CSM, GJK, YG, SAG, DLS, QZ, SWS, RECL. Software: CSM, GJK, SAG, SWS. Formal analysis: JAC, CSM, GJK, YG, DLS. Investigation: JAC, CSM, YG, CSM, QZ. Writing – original draft: JAC, CSM, RECL. Writing – review and editing: JAC, CSM GJK, YG, SAG, DLS, QZ, RECL. Visualization: JAC, CSM, RECL. Supervision and funding acquisition: RECL.

4.0 Implementing a comprehensive model of the NF-κB pathway to optimize cellular responses with dynamic inputs

4.1 Introduction

Cellular signaling pathways respond to extracellular cues through intricate signal transduction networks which modulate various cell fate decisions [1-6]. Variability and nonlinearity are typical characteristics of this signal transduction [56, 64]. Variability arises from various sources of intrinsic and extrinsic noise associated with transcription rates, protein expression etc., whereas nonlinearity emerges due to network topologies with multiple feedback loops and complex interactions between signaling molecules. Additionally, the extracellular environment is dynamic, and cells are constantly exposed to multiple signaling molecules with changing concentrations [2, 10, 12, 13]. The combined effects of variability, nonlinearity and dynamic input signals could therefore make cellular signaling pathways highly versatile in producing a wide range of responses.

The cellular signaling pathways have been traditionally studied and quantified with the dose-response approaches which only consider continuous exposure of signaling molecules. Although response to continuous exposure is a useful end-point reading, it is neither comparable with dynamic signals as seen in vivo, nor is it effective to probe the versatility of cellular responses [2, 11-13, 46, 50]. We and others have recently shown that dynamic input signals can produce atypical cellular responses which could potentially be higher in magnitude compared to those from continuous input signals [11, 12, 46]. Specifically, for the NF-κB pathway (as reported in chapter 2), we showed that the ramp input of TNF concentration can produce atypical and higher responses

in terms of fold change of NF-κB nuclear translocation, than a continuous input over the same exposure time (Figure 2.5). The increase in response happens despite the ramp input exposing cells with only half the AUC of TNF concentration compared to the continuous input. Although we were able to explain the atypical response patterns of NF-κB with a mechanistic model (Figure 2.6), the model fell short of recapitulating the increased response magnitude. We attributed this shortcoming to the lack of key signaling nodes, especially regarding receptor mediated activation of IKK complexes, mechanisms of which were not fully enough understood to be incorporated into the model.

In chapter 3, we quantified the cytokine induced activation of IKK punctate structures, their dynamics, and downstream signal transduction into NF-κB. We reported that the number and time of formation of IKK puncta is controlled by the dynamics of cytokine input (Figure 3.4). Depending upon the cytokine identity, a quantized number of IKK molecules is recruited at punctate structures, activity of which is then pooled for downstream signal transmission (Figures 3.2 and 3.6). We also showed that the aggregate IKK responses, such as AUCs of spot number and intensity, are monotonically correlated with the aggregate NF-κB responses (Figure 3.3). We characterized a signaling motif called Variable-Gain Stochastic Pooling Network (VG-SPN) to formalize this signal transduction (Figures 3.6 and 3.7). We surmised from chapter 3 that this newly characterized mechanism of IKK activity could be a key piece that could improve upon the current mechanistic models of the NF-κB pathway.

In this chapter, we build upon the work presented in chapter 2 and 3 and attempt to construct a comprehensive model of the NF-κB pathway while considering the effects of variability, nonlinearity and dynamic inputs of cytokine concentrations. First, to probe the pathway responses on the orthogonal axis of cytokine exposure, in contrast to cytokine concentration as

reported in chapter 3, we measure the dynamics of both IKK and NF-κB responses as a function of cytokine pulse duration. Because TNF may cause cell death during longer experiments, we chose IL-1 as a preferred cytokine for all the experiments in this chapter. We find that both IKK and NF-κB responses increase with IL-1 pulse duration and saturate beyond a 30 min pulse. Consistent with our previous observations in chapter 3, we also find a strong monotonic relationship between the aggregate AUCs of IKK and NF-κB responses to IL-1 pulses.

Next, we measure the IKK and NF-κB responses to AUC-conserved repeat pulses of IL-1 and compare with the responses of an equivalent 'bolus' pulse. We find that certain repeat pulse conditions, depending on pulse lengths and gap times between the pulses, can produce higher NF-κB responses compared to the bolus pulse. We also find that the monotonic relationship between IKK and NF-κB responses becomes weaker when cells are exposed to repeat pulses of IL-1.

Finally, with the aim of recapitulating our data, we construct a comprehensive model of the NF-κB pathway by integrating the VG-SPN model as explained in chapter 3 with the D2FC model as explained in chapter 1 and building a new receptor binding module. We use the experimental data from pulse experiments to parametrize and constrain the comprehensive model. However, we find that the model is too large and complex to fit with traditional parameter estimation methods and more advanced methods might be needed to fit and use the model for predictive purposes.

4.2 Results

4.2.1 Increasing IL-1 pulse duration produces higher single cell IKK and NF-κB responses with strong monotonic correlation

Although the characterization of the IKK and NF-κB responses to continuous exposures of cytokines, as reported in chapter 3, is useful to understand broader signaling properties, the cytokine exposures experienced by cells in vivo are likely to be transient and pulsatile [2]. Moreover, although the VG-SPN model describes the behavior of IKK puncta once they are formed, the temporal probability of puncta formation as a function of cytokine input is still unknown. To address these issues, we stimulated the doubly tagged U2OS cells (as previously reported in chapter 3) with IL-1 pulses of increasing duration and measured single cell responses both in terms of IKK spot number and fold change of nuclear NF-κB (Figure 4.1 A). For these experiments, we chose the intermediate concentration of 10 ng/ml IL-1 to avoid the effects of saturation while producing an observable response. We observed that as the pulse duration increases, single cell IKK response trajectories form a distinct 'shoulder' indicating more sustained IKK activation at later times (Figure 4.1 A, top row, green line at 60min. Also see Figure 4.6). As the lifespan of a single IKK spot is fixed (Figure B7), the sustained IKK response is likely due to new spots forming at later times in presence of longer IL-1 exposure. We also observed that the longer pulses produce more sustained NF-κB responses compared to those from shorter pulses (Figure 4.1 A, bottom row). Next we measured the 'area under the curve (AUC)' of both IKK and NF-κB response trajectories to characterize their aggregate response. We observed that AUCs of both IKK and NF-κB responses increase with pulse duration and saturate after the 30 minutes of

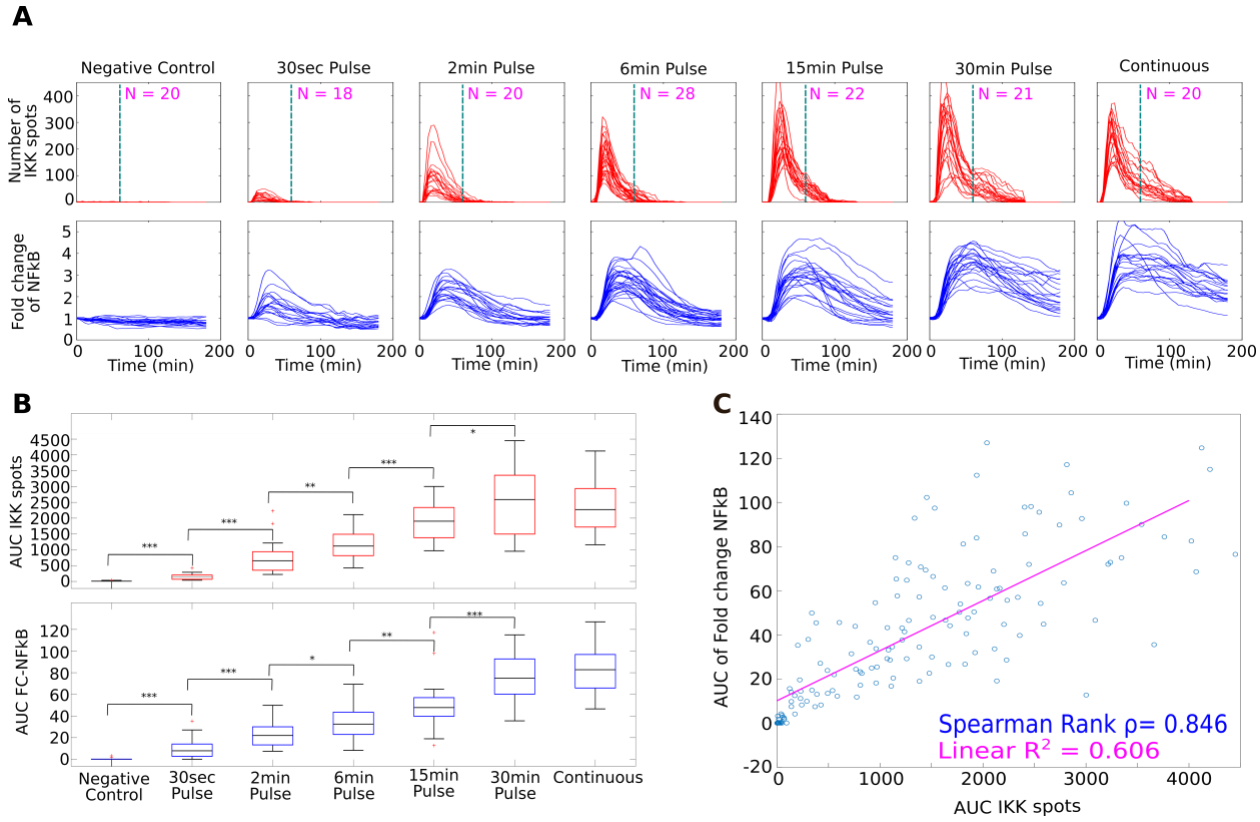

Figure 4.1 Longer Il-1 pulses increase aggregate IKK and NF-κB responses while maintainng a strong monotonic relationshio between the two

(A) Trajectories of single cell responses in terms of number of IKK spots (top row) and fold-change nuuclear NF-κB (bottom row) to IL-1 pulses of increasing duration. Inset number shown number of cells in each condition. Green dashed line denotes time = 60min. (B) Boxplots of aggergate IKK and NF-κB responses measured in terms of AUCs of the corresponding response trajectories in A. * represents $5x10^{-2}>P>5x10^{-3}$, ** represents $5x10^{-3}>P>5x10^{-4}$, and *** represents $5x10^{-4}>P$. (C) Scatterplots of AUCs of IKK spots and fold-change NF-κB showing a strong monotonic relationship. Linear (Pearson, R^2) and Rank (Spearman, ρ) correletation constants are shown.

IL-1 pulse duration (Figure 4.1 B). Because the per-spot lifespan is constant, the AUC of IKK spot number can be used as a proxy to the total number of IKK spots formed. We therefore fitted the AUCs of IKK spot number to different ligand-receptor binding models to get the probability of spot formation over time (Figure 4.8 A, see section 4.2.3 and methods for further information).

Finally, the scatterplots of IKK and NF-κB AUCs show that the strong monotonic relationship between aggregate IKK and NF-κB responses is present in pulsatile exposures (Figure 4.1 C). These results taken together demonstrate that increasing IL-1 pulse duration increases both IKK and NF-κB responses while preserving a strong monotonic relation between the two.

4.2.2 AUC-conserved repeat pulses of IL-1 produce higher NF-κB responses compared to a bolus pulse

We reported in chapter 2 that a ramp input of cytokine produces higher NF-κB response AUC than a continuous input (Figure 2.5), and in chapter 3 that a ramp input produces delayed formation of IKK spots (Figure 3.4). We can also see from Figure 4.1 that a longer exposure to IL-1 produces a more sustained IKK responses (Figure 4.1 A, top row, Figure 4.6 A), and produces higher corresponding NF-κB responses (Figure 4.1 B). Considering these results, we hypothesized that a cytokine stimulation pattern that prolongs the IKK response could in turn result in higher downstream NF-κB response. We also surmised that a repeat pulse stimulation could be used to prolong the IKK response as it will delay the IKK spot formation. To systematically test these hypotheses, we compared responses to a 'bolus' single pulse with those to shorter repeat pulses with identical combined AUC that of the bolus pulse, and with varying gap times between the pulses. We chose a 6min single pulse of 10 ng/ml IL-1 as the bolus to avoid saturation as well as to stay behind the timescale of transcriptionally induced feedback (approx. 30min) for repeat pulse stimulations. First, we stimulated the cells with two, three and four shorter pulses with 3min, 2min and 90sec duration respectively so that the total AUC of exposure is equal to the 6min bolus pulse (Figure 4.2 A). We kept the gap time between these pulses the same at 5 min. We observed that

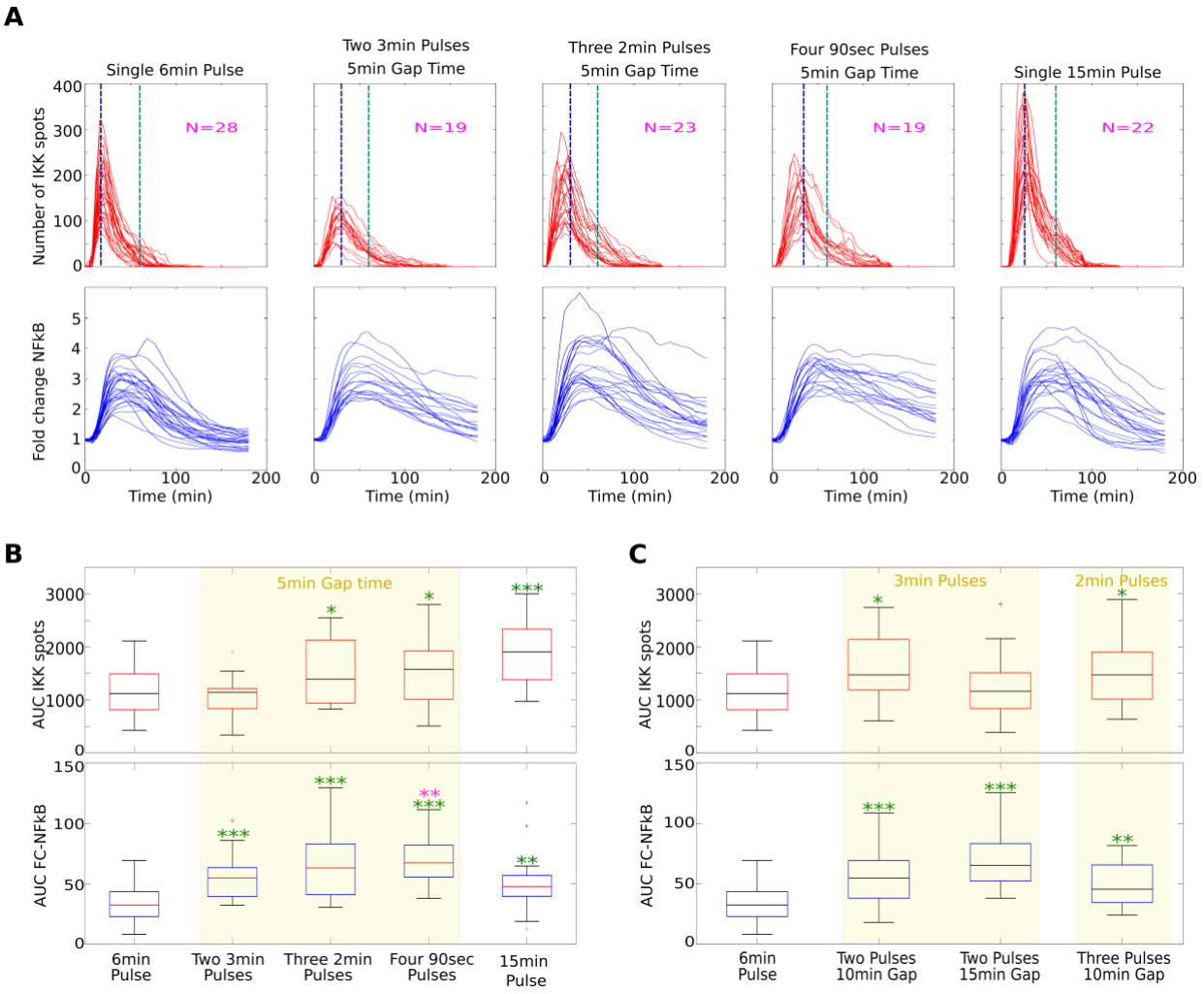

Figure 4.2 AUC-conserved repeat pulses of IL-1 increase NF-κB responses

(A) Trajectories of single cell responses in terms of number of IKK spots (top row) and fold-change nuuclear NF-κB (bottom row) to the AUC-conserved repeat pulses of IL-1. Responses to bolus pulses of 6min and 15min duration are also shon for comparison. Inset number shown number of cells in each condition. Dashed violet line marks the time of peak of the IKK response, which shifts towards the right for repeat pulses compared to the bolus 6min pulse. Green dashed line denotes time = 60min. (B) Boxplots of aggergate IKK and NF-κB responses measured in terms of AUCs of the corresponding response trajectories in A.Conditions with 2 and 3 repeat pulses significantly increase the NF-κB responses compared to the corresponding 6min bolus, while the condition with 4 repeat pulses produces increased response compared to both the 6 and 15 min bolus pulses. IKK responses show only a moderate increase in some repeat pulse conditions. Green * denotes comparison with the 6min bolus while magenta * denotes

comparison with the 15 bolus pulse. (C) Boxplots of IKK and NF-κB responses of AUCs of repeat pulse conditions with varying gap time between the pulses. The corresponding response trajectories are shown in Figures 4.4 and 4.5. Similar to the results in B, while IKK AUCs show a moderate increase, the NF-κB AUCs show significant increae in these repeat pulse conditions. * represents $5x10^{-2}$>P>$5x10^{-3}$, ** represents $5x10^{-3}$>P>$5x10^{-4}$, and *** represents $5x10^{-4}$>P for both B and C.

repeat pulses delay the time of peak (Figure 4.2 A, top row, violet line) and indeed produce a more sustained IKK response compared to that from the bolus (Figure 4.2 A top row, green line. Also see Figure 4.6 B). We also found that while IKK response AUCs do increase moderately in some conditions, the NF-κB response AUCs for repeat pulses are significantly higher compared to the bolus pulse (Figure 4.2 B). Remarkably, the NF-κB response AUCs for the four 90sec pulses are significantly higher than even the 15min single pulse, which has more than twice the input IL-1 exposure. Next we stimulated the cells with 2min or 3min repeat pulses while keeping the total AUC identical to the bolus but varying the gap time between the pulses (Figure 4.4 A and 4.5 A). We again observed higher NF-κB responses with certain repeat pulse conditions of varying gap times compared to the bolus (Figure 4.2 C). Notably, the NF-κB response AUCs decrease as the gap time increases to 15min and beyond (Figure 4.4 B and 4.5 B) suggesting the effect of transcriptionally induced negative feedback. Next we calculated the correlations between the aggregate IKK and NF-κB responses and found that the monotonic relationship between two is significantly reduced for repeat pulse conditions (Figure 4.7). The decrease in monotonicity between IKK and NF-κB responses suggests that the repeat pulse conditions may amplify the dynamic aspects of the relationship and therefore aggregate features such as AUC, may be insufficient to fully characterize the correlation between the two. Taken together, these results

show that certain repeat pulse conditions can produce higher NF-κB responses compared to a bolus pulse of identical AUC of IL-1 input while diminishing the monotonic relationship between the aggregate IKK and NF-κB responses.

4.2.3 Framework for a comprehensive model of the NF-κB pathway

The data reported in the previous sections pose the question of what mechanism could cause the NF-κB response to increase by the repeat pulse inputs. Moreover, can we predict a dynamic stimulus pattern, repeat pulses, ramps or otherwise, that would further maximize the pathway response? A mechanistic model with mathematical representations of pathway components and reactions is needed to address these questions. As reported in chapter 2, our mechanistic model, which lacked the details about the upstream pathway components such as the receptor binding and IKK spot formation, could not explain the increase in NF-κB response with ramp stimuli. We know from the data in the last section that the response of upstream components is significantly altered by the dynamic stimuli, and therefore those need to be included in the mechanistic model in order to correctly represent the signaling mechanisms. We therefore set out to build a comprehensive mechanistic model of the NF-κB pathway which can recapitulate the pathway response from receptor engagement to the gene transcription.

We combined three sub-modules, the receptor binding module, the VG-SPN module and the D2FC model, to construct the framework of the comprehensive model (Figure 4.3 A). First, we built and parametrized the 'receptor binding module' to model the receptor-ligand binding and subsequent recruitment of adapter proteins to intracellular parts of the receptors. Next we used the output of the receptor binding module as input to the VG-SPN module to model the Ubiquitin recruitment and polymerization initiated by the adapter proteins at individual IL-1 induced CI-like

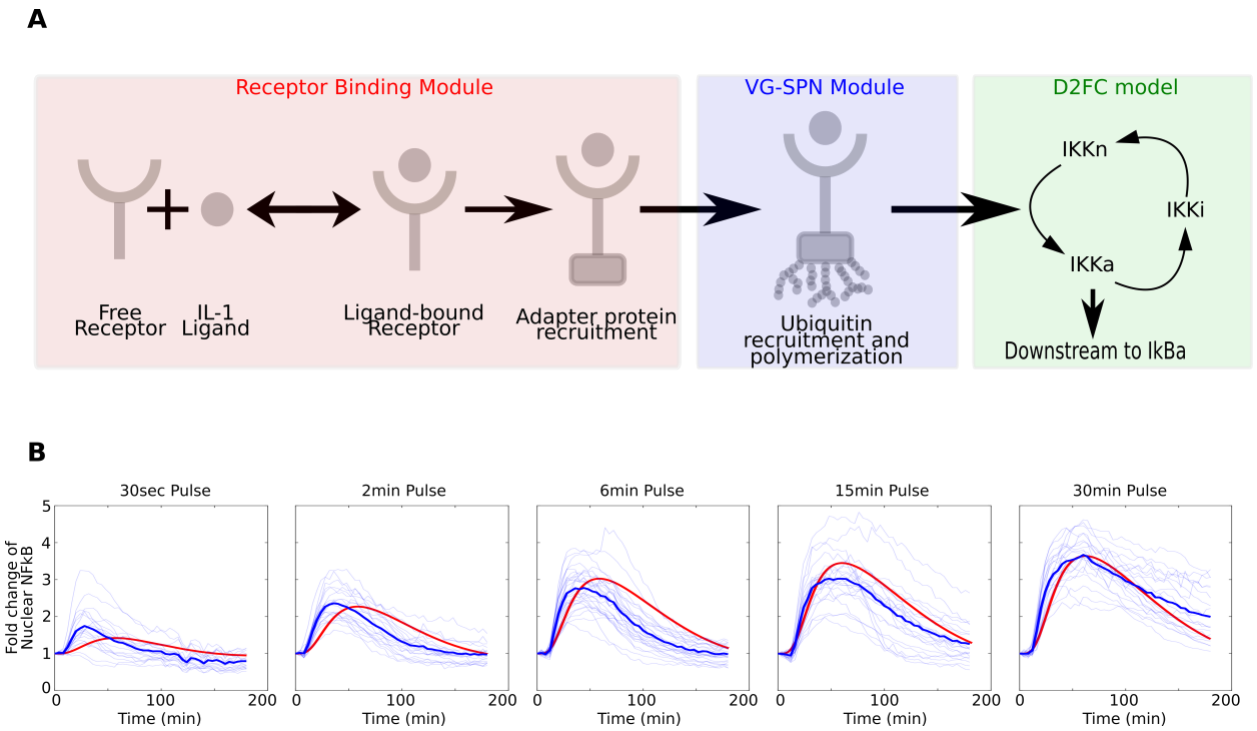

Figure 4.3 Framework of the comprehensive model and example model-fits

(A) The comprehensive model consists of three sequentially connected sub-modules: the receptor binding module, the VG-SPN module and the D2FC model. (B) Exaple fits of the comprehensive model to the single pulse experimenta data. Faint blue lines represent the single-cell trajectories and dark blue lines represent the mean response trajectory. The red lines are the simulated response trajectories.

complexes, and binding of NEMO to such polymerized Ubiquitin scaffolds. We used the 'state-dependent inactivation' [148, 149] mechanism to model the Ubiquitin polymerization in order to achieve perfect adaptation of scaffold-bound NEMO at each CI-like complex as observed in experiments (see methods for details). Finally, we used the output of total scaffold-bound NEMO for IKK activation in the D2FC model. See the methods (section 4.4.4) for further details about the structure and working of each of these modules of the comprehensive model. This framework of the comprehensive model can predict the pathway response at various stages, such as number

and timing of spot formation, activity of individual spots and the nuclear translocation of NF-κB, that can be verified with the experimental data.

We parametrized the comprehensive model by individually fitting the three sub-modules to the experimental data. First, we used the AUCs of IKK response to approximate the spot number and fitted with the receptor binding module (Figure 4.8 A, also see methods). Here we chose the parameter sets that can also produce a higher spot formation with repeat pulses as observed in the experimental data (Figure 4.2 B, Figure 4.8 A, right panel). Next we chose the parameters of the VG-SPN model such that the per-spot scaffold-bound NEMO adapts to zero within the experimentally observed timescales (Figure 4.8 B). The per-spot scaffold-bound NEMO is then summed for all active spots at a given time to obtain the total scaffold-bound NEMO per cell at that time (Figure 4.8 C). The resulting simulated trajectories of scaffold-bound NEMO (Figure 4.8 C) compare well with the experimentally observed IKK spot trajectories (Figure 4.1 A). Finally, to parametrize the D2FC model, we used the simulated trajectories of scaffold-bound NEMO as input to IKK activation (see methods) and then adjusted the parameters to fit to the experimentally observed trajectories of fold-change NF-κB. We used a combination of manual adjustments, Latin-hypercube sampling, and the lsqnonlin optimizer for parameter estimation.

Despite trying various approaches and strategies for parameter estimation, the comprehensive model in its current state does not fully recapitulate the NF-κB response dynamics (Figure 4.3 B). Although the model, to some extent, can recapitulate the increase in IKK response with repeat pulses (Figure 4.9 A, B and D), it falls short of producing significantly higher NF-κB response with repeat pulses (Figure 4.9 C). Due to the complexity of the model, including the feedback loops that can also alter the baseline conditions, more sophisticated approaches might be needed to arrive at the optimal parameter set (see discussion for further analysis).

4.3 Discussion

In this chapter we first systematically generated a dataset measuring the NF-κB pathway response to single pulses of IL-1 with identical concentrations. This dataset is orthogonal and hence complementary to the data presented in chapter 3 wherein NF-κB responses were measured with varying concentrations but continuous exposures of cytokines. Our single pulse data revealed that both IKK and NF-κB responses increase with the IL-1 pulse duration and saturate after a 30min pulse. These data allowed us to make informed approximations about the number and timing of IKK spots which were crucial in parametrizing the receptor binding module of the comprehensive model. We also observed that the monotonic relationship between the IKK and NF-κB response AUCs is preserved with single pulse stimulation. Therefore, we can infer that aggregate features of responses, in contrast to dynamics and features thereof, can be used to characterize the signal transduction with 'bolus' stimuli such as continuous and single pulse exposure.

Next, we measured the IKK and NF-κB responses with repeat pulse stimuli of varying pulse lengths and gap times and compared them with the equivalent bolus pulse. We observed a delay and moderate increase in IKK responses but significant increase in NF-κB responses with certain repeat pulse conditions. We also observed that the monotonic relationship between aggregate IKK and NF-κB responses is lost with repeat pulse stimuli and cannot be captured by low-level dynamic features such as time of peak and full-width-half-max. Therefore, we can infer that dynamics and dynamic features, in contrast to aggregate features, of responses might be essential to characterize signal transduction with dynamic input stimuli.

The delay in IKK responses can be attributed to the delay in the stimulus itself which will cause the IKK spot formation at later times. Furthermore, in our parameter search for the receptor binding module, we discovered that certain parameter sets can indeed result in higher IKK spot formation with repeat pulses compared to the equivalent bolus pulse (Figures 4.8 A, 4.9 A). This increase happens due the reversibility in ligand-receptor binding. After a pulse is taken away, depending on the relative rates of unbinding and adaptor protein recruitment, more free receptors might be available for the next pulse compared to if the previous pulse was persistent. This result will stand true for any reaction system where a reversible reaction is followed by an irreversible reaction. In such systems, the output i.e. the product of the irreversible reaction, under certain conditions, can be maximized by pulsatile introduction of reactants.

The increase in NF-κB responses can be attributed to a few mechanisms and potentially their combined effect. One mechanism for the increase in response could be the delay in transcriptional feedback. Delayed activation of IKK due to repeat pulses will also produce a delayed IκBa mediated feedback and hence will allow the NF-κB to remain in the nucleus for longer times. Another mechanism could be the refractory state of IKKβ wherein the activated IKKβ phosphorylates its own C terminus which weakens its kinase activity [150]. Such hyperphosphorylated IKKβ is then dephosphorylated by phosphatases and returned to its activatable form [151]. Therefore, delayed activation of NEMO spots due to repeat pulses could allow more efficient recycling of IKKβ from its refractory state and hence increase the downstream NF-κB response. Regardless of the mechanism, the repeat pulse data suggest that there will be an optimal combination of pulse length and gap time which could maximize the NF-κB response. Such an optimal input can be thought of as a resonant frequency, which is a common observation in dynamical systems. There could also be response minimization at higher frequencies wherein

several short pulses produce a much delayed IKK response that can't produce any substantial NF-κB translocation. A calibrated model of the system is needed to identify such optimal input patterns and predict the corresponding system responses.

We integrated all the novel findings in this and the previous chapters to construct a framework for the comprehensive model of the NF-κB pathway. Although our model at this stage can qualitatively reproduce some experimental results, more work is needed to find the optimal parametrizations that can quantitatively reproduce the experimental data. At the current stage, the sub-optimal fitting of the model to the data is due to rapid activation of IκB mediated negative feedback, which causes quick translocation of NF-κB out of the nucleus, in contrast to sustained presence as observed in experiments. There are many parameters in the D2FC model, such as the IκB transcription rate, IκB degradation rate, NF-κB-IκB dissociation rate, and the nucleo-cytoplasmic shuttling rates, that need to be simultaneously tweaked while not changing the baseline conditions. Apart from sub-optimal parameterization, there could also be structural characteristics of the D2FC model that may need to be modified for better results. For instance, as the D2FC model only considers the negative feedback from IκBα, activity of other IκB family proteins such as IκBβ and IκBε, which have distinct dynamics, could also be included in the model [152, 153]. Additionally, in the receptor binding module, incorporating additional mechanisms to the simplifying abstraction of all adapter protein recruitment in a single reaction, might alter the dynamics of IKK response and could improve the model performance, especially with the repeat pulse inputs. Advanced parameter estimation methods such as Markov Chain Monte Carlo sampling paired with parallel tempering could prove greatly useful in finding the optimal parametrizations of the model [73, 154].

4.4 Methods

4.4.1 Cell culture

U2OS cells doubly tagged with EGFP-NEMO and mCherry-RelA (as described in chapter 3) were cultured in McCoy's 5A media at 37°C and 5% CO2. The media was supplemented with 10% Corning regular fetal bovine serum (FBS), penicillin (100 U/ml), streptomycin (100 U/ml), and 0.2 mM L-glutamine (Invitrogen). Cells were periodically monitored for mycoplasma contamination.

4.4.2 Live-cell imaging for pulse experiments using the microfluidic dynamical stimulation system

Our in-house developed microfluidic system, as described in detail in chapter 2, was used for the single and repeat pulse experiments. Briefly, 2-inlet PDMS devices were made from corresponding 3D printed molds, autoclaved, washed with ethanol and incubated with 0.002 (v/v) solution of fibronectin in PBS for 24 hours at 37^0C. The U2OS double-CRISPR cells (~ $5*10^6$ cells/ml) were then seeded in the microfluidic devices and incubated for at least 24 hours. On the day of experiment, the microfluidic device was connected to the basins, containing appropriate treatments, on the gravitational pump using tygon tubes. FluoroBrite media (Gibco, A18967-01) was used for imaging. Additionally, IL-1 treatment was made with Alexa Fluor 647–conjugated BSA (0.0025, v/v; Invitrogen) to confirm the stimulation patterns. The Alexa FITC channel was used to acquire z-stack (eight images of 0.5-µm separation) images of EGFP-NEMO every 4 minutes with an exposure of 0.04 s and a transmission of 32%. Similarly, the Alexa A594 channel

was used to image mCherry-RelA every 4 minutes at 0.1 s exposure and 50% transmission; whereas Alexa CY5 channel was used to image Alexa Fluor 647–conjugated BSA every 1 minute at 0.1 s exposure and 50% transmission. All images were acquired in an environmentally controlled chamber (37°C, 5% CO2) on a DeltaVision Elite microscope equipped with a pco.edge sCMOS camera and an Insight solid-state illumination module (GE Healthcare) at 60x magnification.

4.4.3 Extracting EGFP-NEMO and mCheery-RelA data from live-cell images

As explained before in chapter 3, the in-house built dNEMO software was used to detect and quantify EGFP-NEMO spots. The threshold for spot detection in dNEMO was set between 2.1 and 2.4 and only spots appearing in at least two contiguous slices of the 3D images (of eight slices) were considered valid. Single cells were manually segmented using dNEMO's keyframing function. Trajectories of mCherry-RelA nuclear intensity were quantified using custom ImageJ scripts. The fold change transform was carried out by dividing the mCherry-RelA trajectories by the initial nuclear fluorescence at the zero time point. A 3-point moving average was taken to prepare display images.

4.4.4 Building the comprehensive model of the NF-κB pathway

Our framework for the comprehensive model of the NF-κB pathway consists of three sub-modules that are linked together (Figure 4.3 A). First, we have the receptor binding module, which describes the receptor-ligand binding on plasma membrane and recruitment of corresponding

adaptor proteins that are required to initiate Ubiquitin polymerization. Second, we have the VG-SPN module, which describes the ubiquitin polymerization that results in quantized NEMO recruitment at the punctate structures. Third, we have the D2FC model [42], which describes the IKK activation from recruited NEMO and the subsequent NF-κB nuclear translocation as well as the activation of IκBa and A20 mediated negative feedback. The VG-SPN model is described in detail in the methods section of chapter 3 and more details about the D2FC model can be found in the methods section of chapter 2 and [42]. Here we focus on the receptor binding module, and the changes that we incorporated in the VG-SPN and D2FC modules to integrate them all in the comprehensive model.

The receptor binding module consists of three biomolecular species: the free receptor (R), the ligand-bound receptor (LR) and the receptor with recruited adapter proteins (R*) (Figure 4.3 A). Here, a ligand (such as IL-1) can reversibly bind to its receptor, and a ligand-bound receptor can then initiate recruitment of various adapter proteins. Although multiple adapter proteins such as Myd88 and IRAK1 are necessary to the formation of IL-1 induced CI-like complexes that can initiate Ubiquitin polymerization [155, 156], we abstracted all their recruitment with a single irreversible reaction. There are two reactions in the receptor binding module:

$$L + R \rightleftharpoons LR \quad \{K1, Kd1\}$$

$$LR \rightarrow R^* \quad \{K2\}$$

Here K2 is an aggregate parameter representing the rate of recruitment of adaptor proteins such as MyD88 and IRAK1. We modeled the adapter protein recruitment as an irreversible reaction to represent the ‘spot formation’ - a point of no return after which the IKK spot is mature enough to initiate Ubiquitin recruitment and polymerization. We did not consider the receptor recycling as IL-1R1 is internalized after binding and no significant replenishment is observed for

at least 4 hours post-treatment with IL-1 [157, 158]. We assumed the ligand to be in excess and therefore did not explicitly model its dynamics and assumed the ligand concentrations remains constant, denoted by 'Dose'. The corresponding ODEs for the receptor binding module are as follows:

$$\frac{d[R]}{dt} = Kd1 * [LR] - K1 * Dose * [R]$$

$$\frac{d[LR]}{dt} = K1 * Dose * [R] - Kd1 * [LR]$$

$$\frac{d[R^*]}{dt} = K2 * [LR]$$

In order to fit the receptor binding module to the experimental data, we used the single pulse data to approximate spot formation. As the lifespan of a spot is fixed, we can use the AUC of spot number (Figure 4.1 B) as a proxy to the total number of spots formed in a given pulse condition. We assumed the 30min pulse is saturating i.e. it can convert all free receptors to active spots. We therefore normalized the IKK spot number AUCs of other pulse conditions with that of the 30min pulse to approximate the fraction of free receptors converted into spots. This fraction then can be multiplied with the number of free receptors (i.e. R) to obtain the experimentally approximated number of spots formed in a given pulse condition.

We fitted the receptor binding module to the experimentally approximated number of spots formed using the MATLAB 'lsqnonlin' optimizer. We used the range of IL-1 ⇌ IL-1R1 dissociation constant as reported in [159] to constrain Kd1, and allowed K1 and K2 to vary two orders of magnitude above and below the Kd1 range (Figure 4.8 A, left panel). While fitting we realized that many parameter sets of {K1, Kd1 and K2} fit the data equally well. We know that many repeat pulse conditions produce more AUC of spot number compared to the corresponding bolus pulse (Figure 4.2 B). We therefore chose the parameter sets that produce a higher number of

spots for repeat pulse conditions compared to the corresponding bolus (Figure 4.8 A, right panel). Thus, the output of the receptor binding module is a binary vector of length equal to the number of free receptors, having entries of 1 if the corresponding receptor has formed a spot, and 0 if it has not. This binary vector represents the number of spots formed at a given time, for a given treatment condition (i.e. single or repeat pulses).

The VG-SPN module describes the Ubiquitin recruitment at a spot once the spot is formed. We used the binary output vector from the receptor binding module to initiate the VG-SPN module. In chapter 3, we used a negative feedback-based mechanism to model the Ubiquitin polymerization (Methods section 3.4.14). Although the negative feedback was helpful in discriminating between the sources of feedback, it does not produce perfect adaptation i.e. the per-spot intensity does not go to zero as observed in the experimental data (Figure 3.5). As the output of the VG-SPN module will affect the downstream NF-κB activation, perfect adaptation is crucial for the integration of the VG-SPN model. Therefore, in order to achieve perfect adaptation, we replaced the negative feedback mechanism with the 'state-dependent inactivation' mechanism [148, 149]. In state-dependent inactivation, rather than activating its own local negative feedback (e.g. deubiquitinases), a spot passively undergoes Ubiquitin depolymerization with a fixed rate. In addition to achieving perfect adaptation, this mechanism requires fewer assumptions and is easier to manipulate the per-spot dynamics. The corresponding model ODEs are as follows:

$$\frac{d[Ub_{Poly}]}{dt} = K_{Poly} * (MaxUb - Ub_{Poly} - Ub_{dePoly}) - K_{dePoly} * Ub_{Poly}$$

$$\frac{d[Ub_{dePoly}]}{dt} = K_{dePoly} * Ub_{Poly}$$

$$[Scaffold \cdot bound\ NEMO] = 300 * \sum_{i}^{\#Spots} Ub_{Poly}$$

Here Ub_{Poly} represents the extent of Ubiquitin polymerization at a spot, whereas Ub_{dePoly} is an abstract variable representing the corresponding depolymerization. MaxUb represents the carrying capacity of each spot in terms of the scaffold of polymerized Ubiquitin. We set the value of MaxUb to 1.2 so that the model produces per-spot trajectories with an average maximum value of 1 of the polymerized Ubiquitin scaffolds. We also introduced variability in MaxUb to account for the variation in per-spot dynamics (Figure B7). We assume that the NEMO recruitment at each spot is a proxy to the size of polymerized Ubiquitin scaffold at that spot. We have also estimated that the number of NEMO molecules per IL-1 induced spot is approximately 300 (Figure 3.2 D). We can therefore multiply [Ub_{Poly}] by 300 to get the number of 'scaffold-bound NEMO' at each spot. We chose the parameters of the VG-SPN module such that the scaffold-bound NEMO undergoes perfect adaptations within the experimentally observed timescales (Figure 4.8 B). Next, we can sum the total output of the VG-SPN model in terms of the scaffold-bound NEMO at a given time to obtain the total number of scaffold-bound NEMO per cell at that time (Figure 4.8 C). The scaffold-bound NEMO per cell is then used as input to the downstream D2FC model.

The VG-SPN module is connected to the D2FC model via the IKK activation mediated by the scaffold-bound NEMO. The D2FC model has three states in which IKK can exist: active IKK that can phosphorylate IκBa (IKKa), neutral IKK that can be activated by scaffold-bound NEMO (IKKn), and inactive IKK (IKKi), which is converted from IKKa, potentially due to hyperphosphorylation [150]. IKKi can then be converted to IKKn by phosphatases so that the total amount of IKK remains constant. The scaffold-bound NEMO can bind to any of the IKKa, IKKn

or IKKi but only IKKn can be converted (or activated) to IKKa. This process resembles competitive binding and we therefore used the following ODEs to represent the IKK activity:

$$\frac{d[IKKn]}{dt} = Kp * [IKKi] - \frac{Ka * [Scaffold - bound\ NEMO] * [IKKn]}{(1 + [IKKn] + [IKKa] + [IKKi])}$$

$$\frac{d[IKKa]}{dt} = \frac{Ka * [Scaffold - bound\ NEMO] * [IKKn]}{(1 + [IKKn] + [IKKa] + [IKKi])} - Ki * [IKKa]$$

$$\frac{d[IKKi]}{dt} = Ki * [IKKa] - Kp * [IKKi]$$

The IKKa then participates in the downstream reactions as described by the D2FC model. We did not make any other structural alterations in the other ODEs of the D2FC model. However, we did adjust the corresponding parameters to fit the model output to the experimental data.

Overall, the comprehensive model takes the stimulus dynamics in terms of dose(t) as input, and predicts the time and number of spots formed, dynamics of per-spot activity, the corresponding IKK activity, and the downstream response in terms of NF-κB nuclear translocation. Assuming the number of free receptors to be R, in total the model has 2R+19 ODEs. We assumed the number of free receptors to be 500 (IL-1R1, Figure 3.1) which makes the total number of ODEs to be 1019. All new and adjusted parameters used in the model are tabulated in Table 4.1.

We used a combination of manual adjustments and lsqnonlin optimizer to fit the comprehensive model to the single pulse experimental data. Although we obtained a reasonable fit, a more systematic approach is needed to achieve better fits as well as to further study the model (i.e. for repeat pulses, sensitivity analysis), and make reliable predictions. Approaches such as Markov-Chain Monte Carlo paired with parallel tempering can be used for better and efficient parameter estimation [73].

4.5 Supplementary figures and table regarding chapter 4

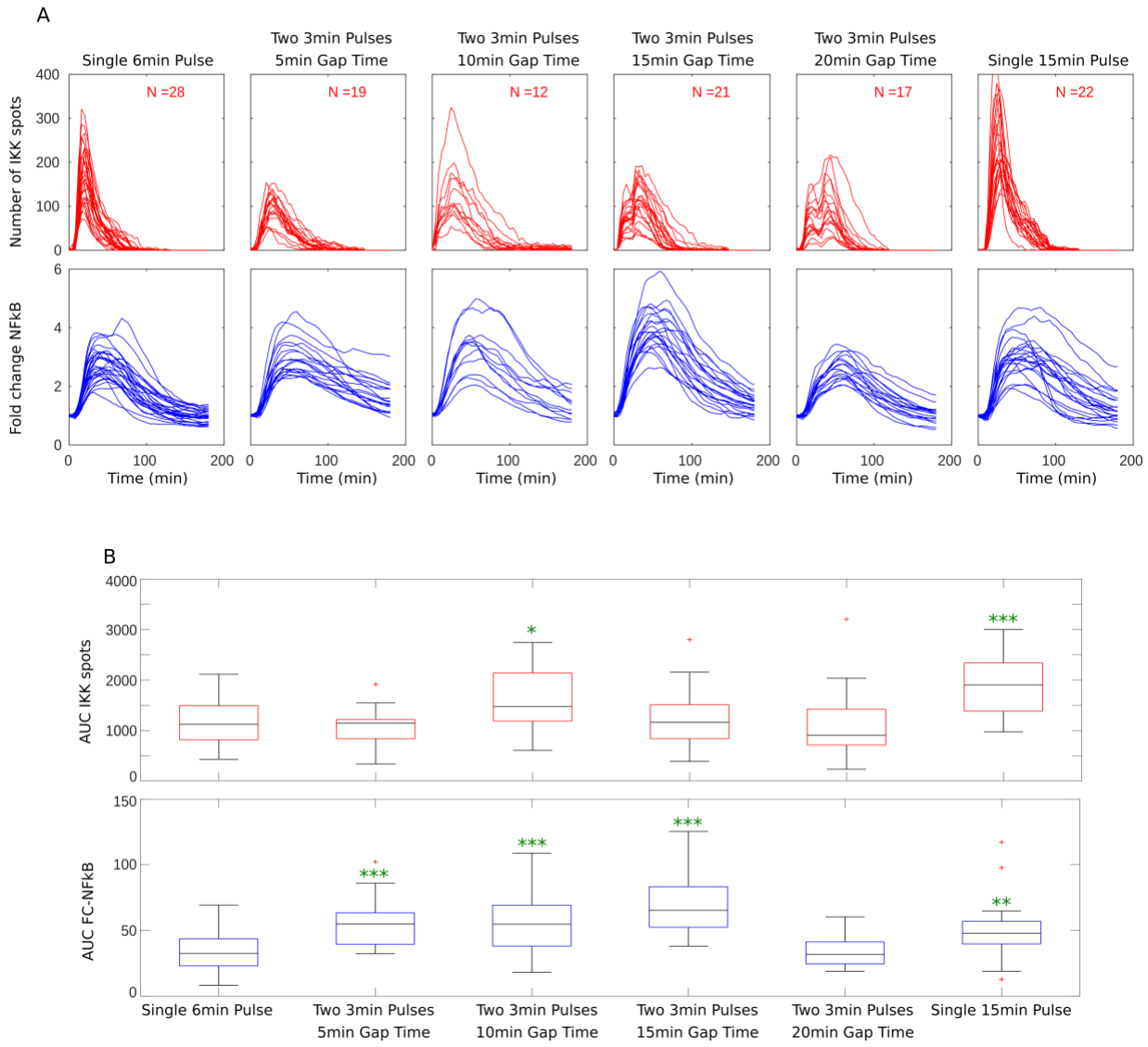

Figure 4.4 IKK and NF-κB responses to two 3min pulses with varying gap time

(A) Trajectories of single cell responses in terms of number of IKK spots (top row) and fold-change nuuclear NF-κB (bottom row) to two 3min IL-1 pulses of increasing gap times of 5, 10, 15 and 20 min. Inset number shown number of cells in each condition. Bolus 6min and 15min pulse response are shown for comparison. (B) Boxplots of aggergate IKK and NF-κB responses measured in terms of AUCs of the corresponding response trajectories in A. Green * denote comparison with the 6min bolus pulse. * represents $5x10^{-2}>P>5x10^{-3}$, ** represents $5x10^{-3}>P>5x10^{-4}$, and *** represents $5x10^{-4}>P$.

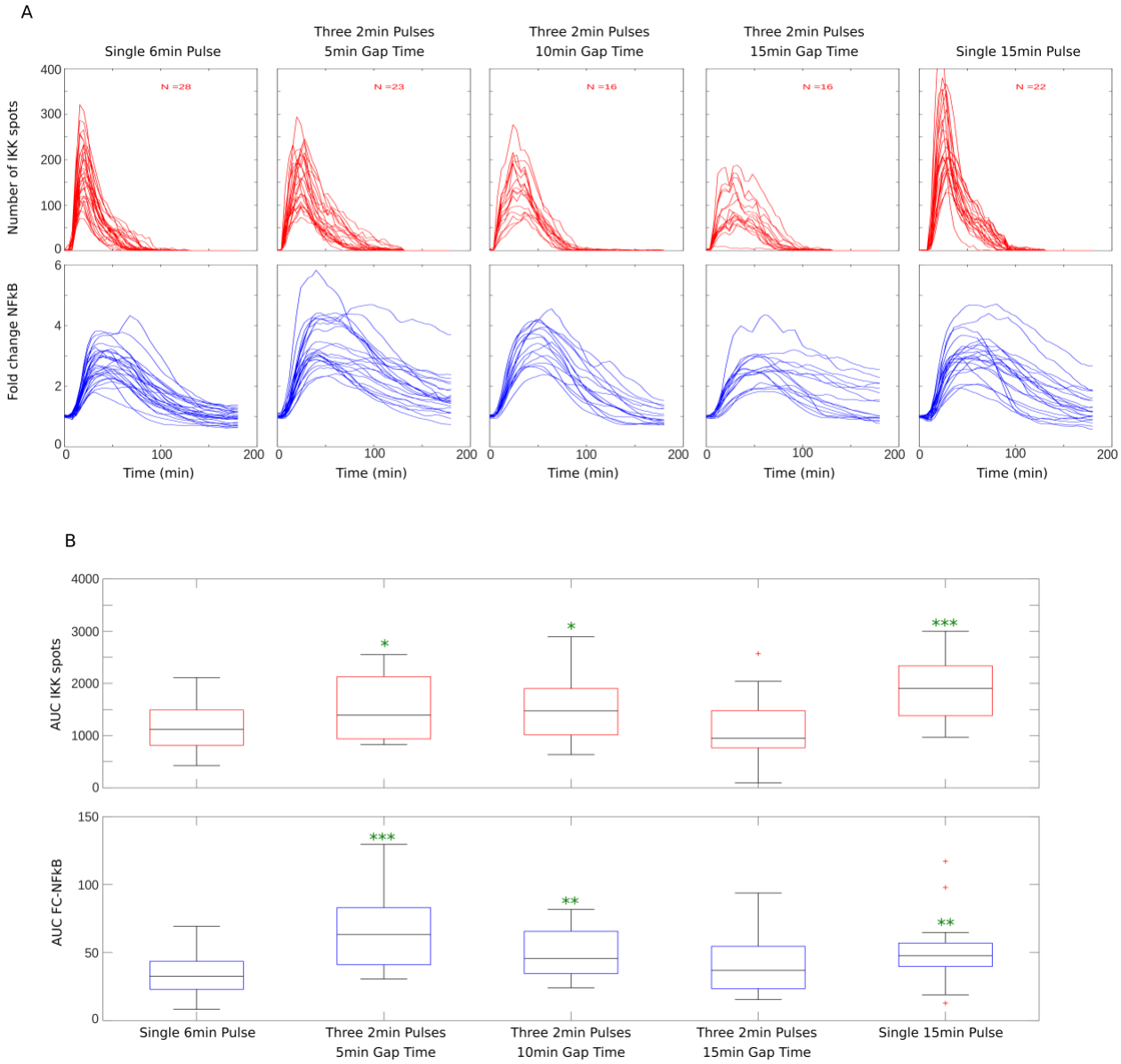

Figure 4.5 IKK and NF-κB responses to three 2min pulses with varying gap time

(A) Trajectories of single cell responses in terms of number of IKK spots (top row) and fold-change nuuclear NF-κB (bottom row) to three 2min IL-1 pulses with increasing gap times of 5, 10 and 15 min. Inset number shown number of cells in each condition. Bolus 6min and 15min pulse response are shown for comparison. (B) Boxplots of aggergate IKK and NF-κB responses measured in terms of AUCs of the corresponding response trajectories in A. Green * denote comparison with the 6min bolus pulse. * represents $5x10^{-2}$>P>$5x10^{-3}$, ** represents $5x10^{-3}$>P>$5x10^{-4}$, and *** represents $5x10^{-4}$>P.

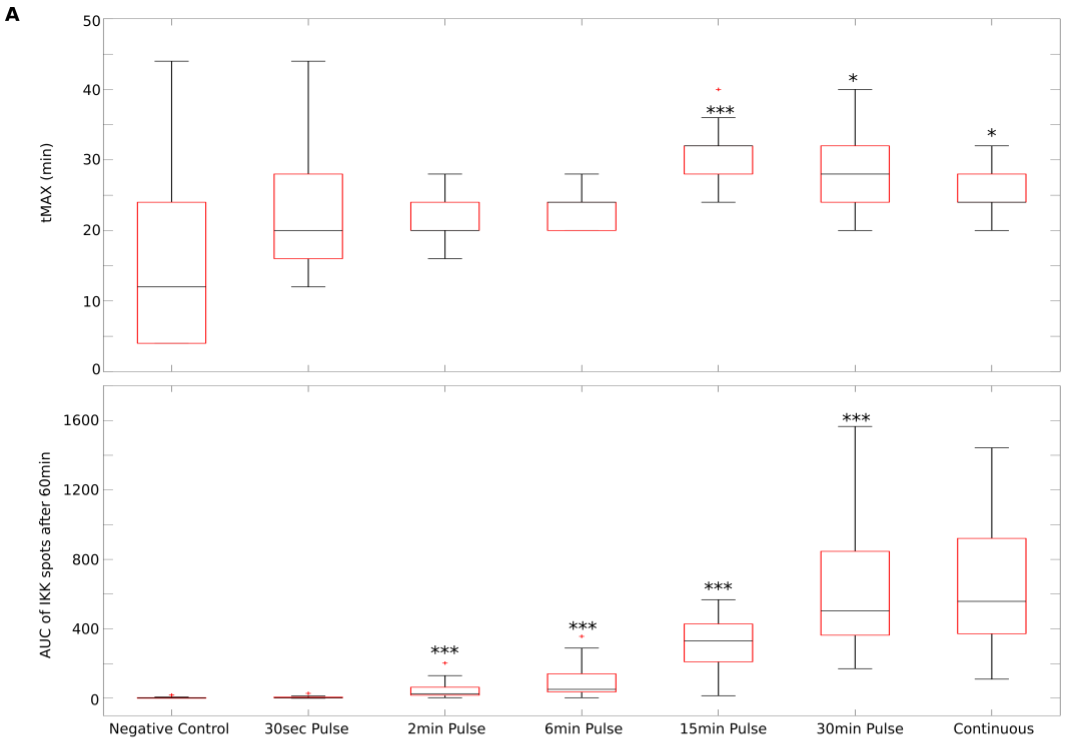
A
tMAX (min)
AUC of IKK spots after 60min
Negative Control
30sec Pulse
2min Pulse
6min Pulse
15min Pulse
30min Pulse
Continuous

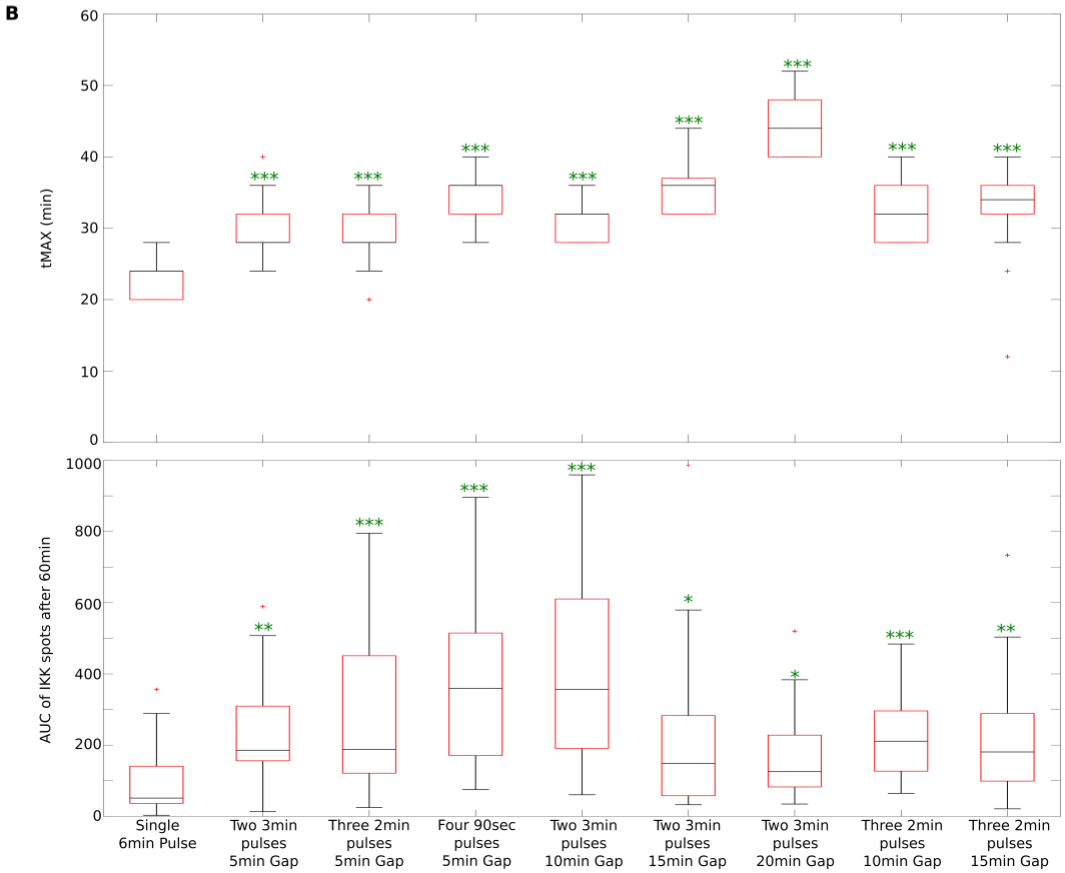
B
tMAX (min)
AUC of IKK spots after 60min
Single 6min Pulse
Two 3min pulses 5min Gap
Three 2min pulses 5min Gap
Four 90sec pulses 5min Gap
Two 3min pulses 10min Gap
Two 3min pulses 15min Gap
Two 3min pulses 20min Gap
Three 2min pulses 10min Gap
Three 2min pulses 15min Gap

Figure 4.6 Repeat pulse conditions prolong the IKK response

Boxplots of time of peak (tMAX, top) and AUC after 60min (bottom) of IKK responses to single pulses (A) and repeat pulses (B) of IL-1. Repeat pulse conditons significantly increase both tMAX and the AUC after 60min compared to the 6min bolus. In (A) * denote the comparison to the condition immediately to the left. In (B) * denote comparison with the 6min bolus pulse. For both (A) and (B) * represents $5x10^{-2}>P>5x10^{-3}$, ** represents $5x10^{-3}>P>5x10^{-4}$, and *** represents $5x10^{-4}>P$

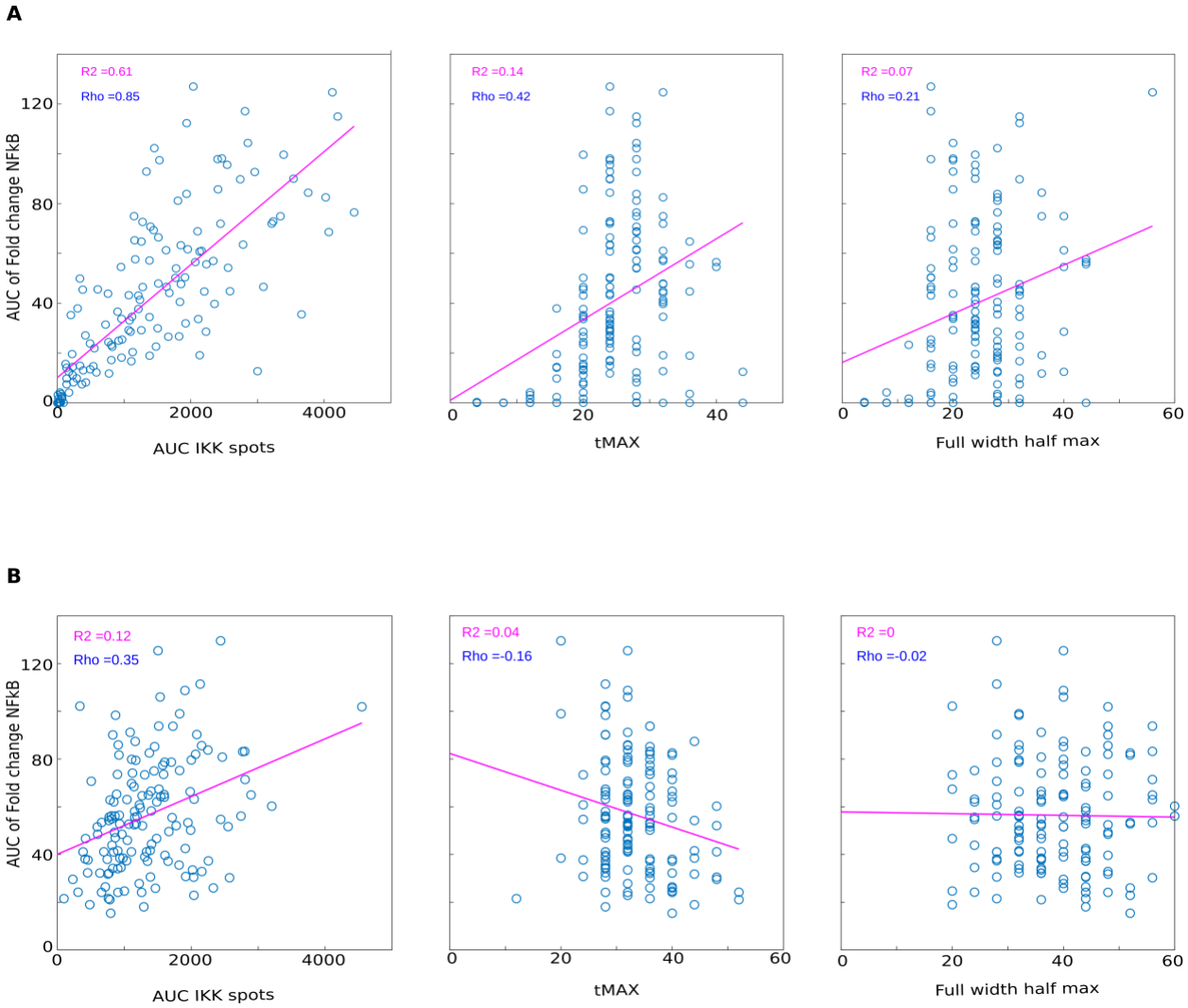

Figure 4.7 Monotonic reationship between aggregate IKK and NF-κB responses decreases in repeat pulse conditions

Scatterplots of AUC of fold-change NF-κB vs features of IKK response trajectories of single pulses (A) and repeat pulses (B). Linear (Pearson, R^2) and Rank (Spearman, ρ) correletation constants are shown. The monotonic relationship between AUCs of NF-κB of IKK siginficantly decreases in repeat pulse conditions compared to single pulses, as seen by decrease in the Spearman Rank correlation. Features of the trajectory dynamics, such as tMAX (time of peak of IKK) and 'Full width half max' (see section 3.4.12), are also unable to capture the relationship.

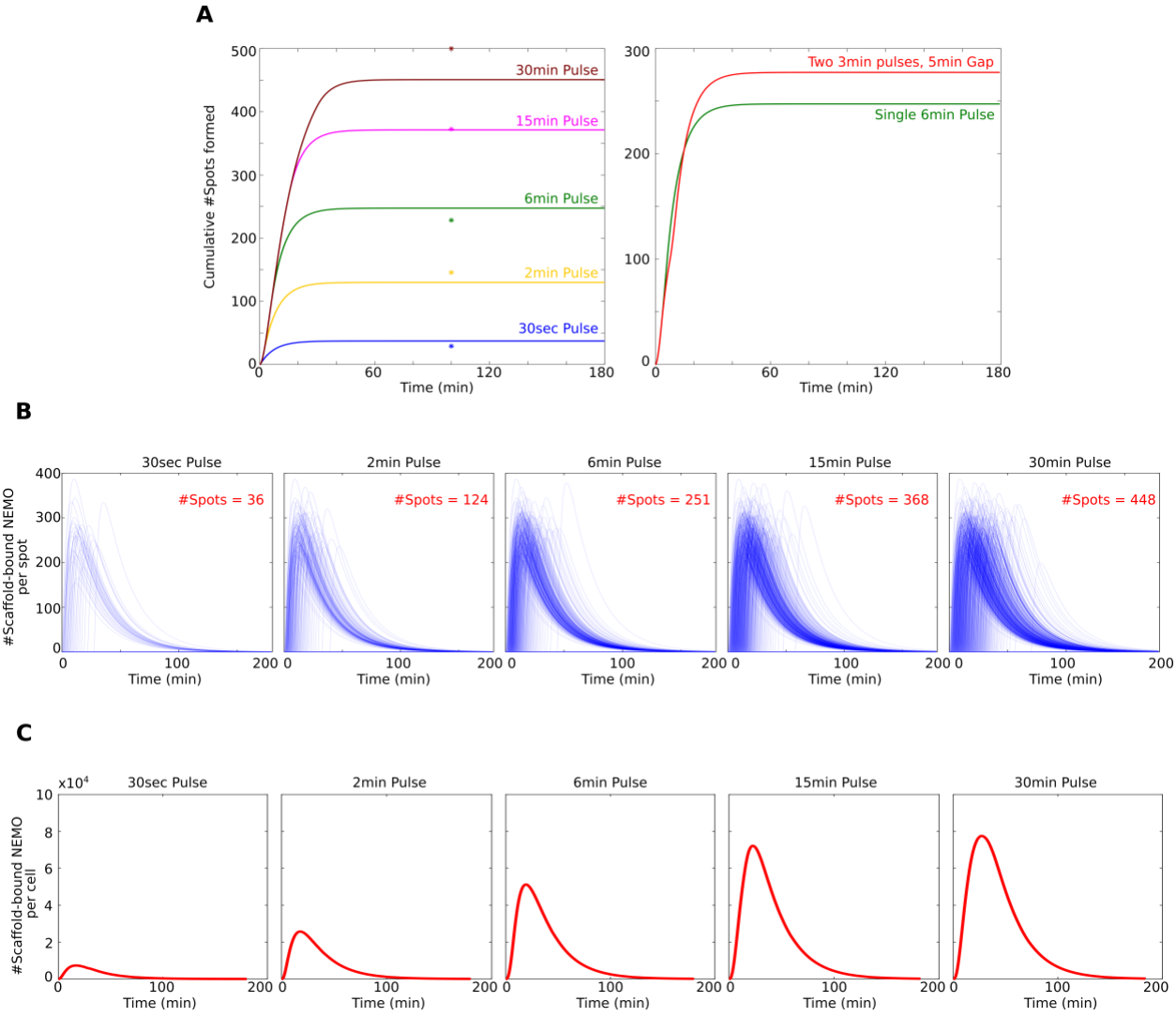

Figure 4.8 Example simulations of the comprehensive model with single pulse inputs

(A) The parameters of the receptor binding module are chosen such that experimentally approximated number of IKK spots are produced with single pulses (*s on left panel) as well as more number of spots are formed with repeat pulses compared to the bolus (right panel). The comprehensive model can predict the scaffold-bound NEMO per spot (B) as well as per cell (C) depending on the input stimuli.

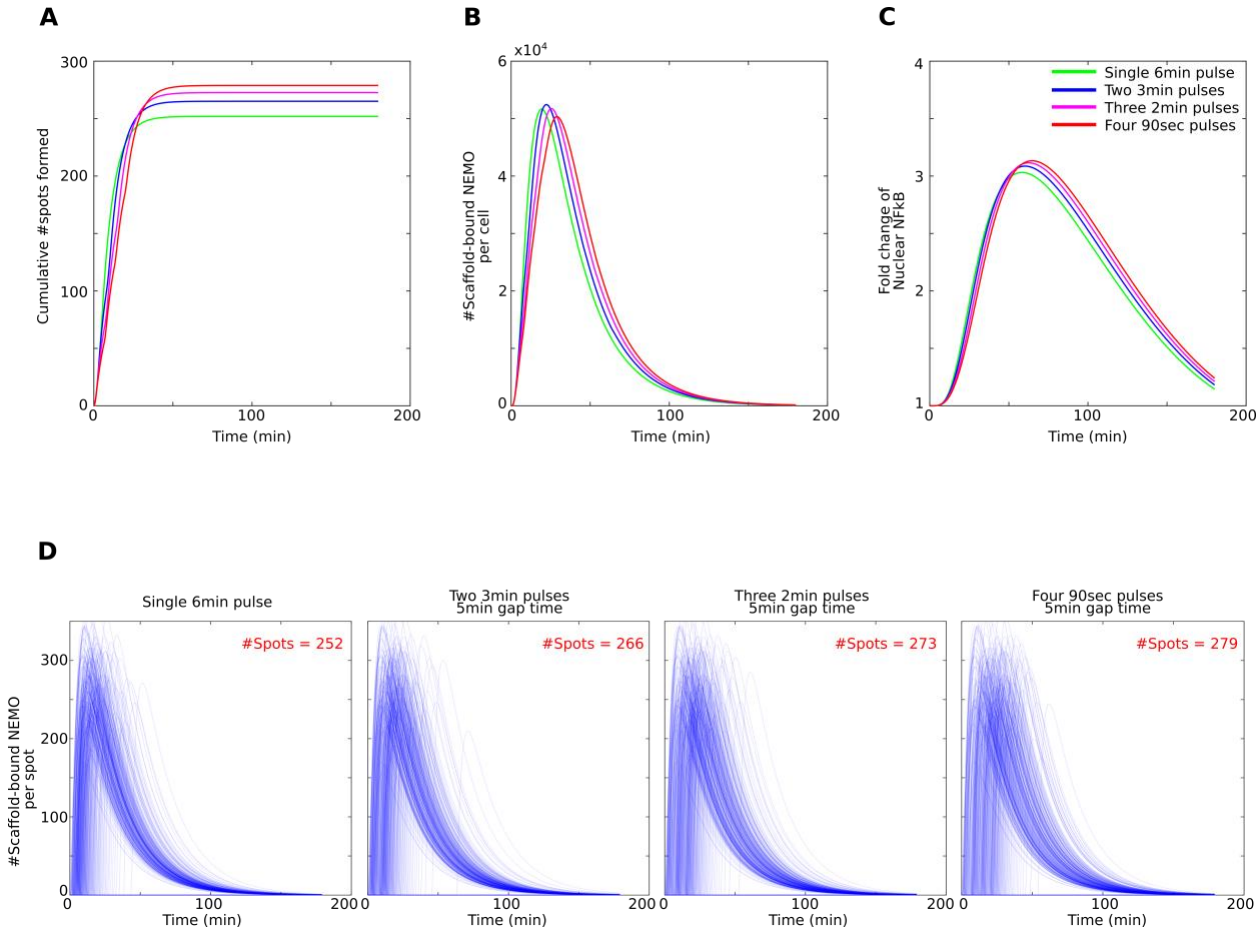

Figure 4.9 Example simulations of the comprehensive model with repeat pulse inputs

(A) Chosen parametrization of the receptor binding module produces increase in IKK spot number as the number of repeat pulses increases. (B) Simulated total response of the scaffold-bound NEMO is delayed and higher for the repeat pulses compared to the bolus pulse. (C) Simulated repeat pulses produce slight increase in the NF-κB response but the simulated response trajectories are both qualitatively and quantitatively different than the experimental observation (Figure 4.2 A). (D) Example trajectories of per-spot scaffold-bound NEMO with repeat pulse simulations. Activity of newly formed spots can be seen equally-spaced clustes of trajectories. All repeat pulse simulations shown have a 5min gap time between the pulses.

Table 4-1: Parameters values used in the comprehensive model of the NF-κB pathway

	Parameter	Value	Unit	Description
Receptor Binding Module	K1	4.691×10^{-4}	Concentration^{-1} s^{-1}	Ligand-receptor binding rate
	Kd1	9.647×10^{-4}	s^{-1}	Ligand-receptor unbinding rate
	K2	1.3×10^{-3}	s^{-1}	Rate of adapter protein recruitment
VG-SPN Module	K_{Poly}	5×10^{-3}	s^{-1}	Rate of Ub polymerization
	K_{dePoly}	7×10^{-4}	s^{-1}	Rate of Ub de-polymerization
	MaxUb	1.2	A.U.	Carrying capacity of Ub scaffolds
	MaxUb_cov	0.2	-	Coefficient of variation of carrying capacity of Ub scaffolds
	Scaling_factor	300	Number	Number of scaffold-bound NEMO per spot

Table 4-1 continued

D2FC Model	Ka	$1x10^{-8}$	$\mu M\ Molecules^{-1}\ s^{-1}$	Rate of conversion of IKKn into IKKa
	Ki	0.1	s^{-1}	Rate of conversion of IKKa into IKKi
	Kp	$3.16x10^{-2}$	s^{-1}	Rate of conversion of IKKi into IKKn
	IkBa_tr_rate	$8.844x10^{-8}$	$\mu M\ s^{-1}$	Rate of transcription of IkBa
	IkBa_NfkB_diss_rate	0.04	s^{-1}	Dissociation rate of IkBa-NFkB
	IkBa_phosph_rate_free	0.0433	$\mu M^{-1}\ s^{-1}$	Rate of IKKa mediated phosphorylation of Free IkBa
	IkBa_phosph_rate_bound	0.2164	$\mu M^{-1}\ s^{-1}$	Rate of IKKa mediated phosphorylation of NFkB bound IkBa
	A20_tr_rate	$2x10^{-10}$	$\mu M\ s^{-1}$	Rate of transcription of A20
	Init_NFkB	0.3	µM	Total NFkB in the cell
	Init_IKK	0.08	µM	Total IKK in the cell

Only the tweaked parameters from the D2FC model are shown in the table. For full list of D2FC parameters see [42].

5.0 Conclusion

We reported the development of a low-cost and accessible microfluidic stimulation system in chapter 2. We demonstrated its functionality in various experiments in chapters 2, 3 and 4. These experiments, especially those from chapter 4, provide examples of how dynamic stimuli can be useful to delineate and understand key mechanisms of signal transduction, and to manipulate the output of signaling networks. Probing signal transduction machinery with dynamic stimuli can also reveal the influence of variability within cell populations and its effects on the output responses of signaling networks. Furthermore, our results in chapter 2 and 4 suggest that pharmacologic control of input signal dynamics may effectively modulate the degree and mode of pathway activation for signaling networks, which may prove valuable in designing optimal point-of care strategies. As systems-level studies pursue subjects with increasing complexity, for example using asynchronous perturbations to shift and exploit cell phenotypes [160, 161], biology labs will require tools that reproducibly control dynamic cellular microenvironments. We expect that our low-cost, scalable, and modular dynamic stimulation system, as reported in chapter 2, will find broad adoption, help reveal molecular mechanisms of complex cellular behaviors, and can be extended generally for automation of other fluidic applications.

In chapter 3, we characterized the cytokine signal encoding into the IKK punctate structures (CI-like complexes) and its downstream decoding into the NF-κB responses. We showed that the cytokine identity is encoded into the CI-like complexes via an amplification ‘gain’ which determines the number of IKK molecules that can be recruited at a punctate structure, independent of other CI-like complexes and feedback. These ‘gains’ at IKK level are then ‘pooled’ before the signal is transmitted downstream into NF-κB. We developed a computational framework, called

the Variable-Gain Stochastic Pooling Network (VG-SPN) model, to describe this quantized and switch-like activity of the CI-like complexes. The VG-SPN model characterizes the cytokine mediated signal transduction at the level of receptors, associated adaptors and machinery required to transmit the signal into the cell – an area which was previously less explored. Our data and models reveal key insights about the signal and information transfer across plasma membrane through the receptors and associated machinery. The classic model of chemoreception [162], established limitations for the signal-to-noise relationships in biological sensing systems that use time-averaged receptor occupancy to measure chemical concentration. By contrast, multivalent cytokines exhibit markedly increased apparent affinity over bimolecular interactions and therefore limit the likelihood of ligand dissociation from mature signaling complexes. Although these signaling systems are distinct, they are both reducible to the same motif with alternative definitions for amplification gain, and possibly with different pooling functions. A remaining question is why biological sensory systems would converge on SPN-like architectures? Although several conceptual benefits and limitations of VG-SPNs are discussed here, other general properties of SPNs may also contribute to the answer. Stochastic resonance is an example of a counterintuitive property of SPNs that uses stochastic fluctuations to enhance information transmission [139, 163]. Although the number and timing of CI-like switches is stochastic and subject to noise during cytokine responses, they can theoretically enhance information transmission over an array of noiseless binary switches. An array of perfect switches that simultaneously activate at the same signal threshold is a binary system, either all ‘on’ or all ‘off’, whereas stochasticity in the fraction and timing of CI formation increases the number of system states through probabilistic interactions with the milieu. Although our results in chapter 3 revealed CI-like complexes are independent and switch-like, where each complex recruits a quantized amount of IKK over its lifespan, these were

unexpected results that led to conceptual simplification and identification of the underlying signaling architecture. However, independence between detector nodes such as CI-like complexes is not a required characteristic of a VG-SPN and most receptor signaling systems can therefore be viewed through a similar lens. We expect the VG-SPN is common to receptor-signaling systems, each with distinct pooling functions, feedbacks, and feedforwards that will reveal their individual trade-offs and information transmission benefits to the cell.

In chapter 4, we showed that while the monotonic relationship between aggregate features of IKK and NF-κB responses is preserved with bolus stimuli such as single pulses, the relationship is lost with dynamic stimuli such as repeat pulses. As the cells are constantly exposed with dynamic stimuli in vivo, these data underscore the importance of measuring and characterizing the response dynamics of signal transduction. The observed increase in NF-κB responses with repeat pulse stimuli further demonstrates, in addition to results in chapter 2, how dynamic stimuli can be used to manipulate the patterns and magnitudes of pathway responses. We consolidated all our results from chapters 2,3 and 4 to construct a comprehensive mechanistic model of the NF-κB pathway. The comprehensive model provides a practical framework to build mechanistic models of NF-κB signaling via other cytokines such as TNF, and potentially an integrated model that can predict the pathway responses to simultaneous exposures of multiple cytokines. While our attempts to fit the comprehensive model to the experimental data fell short of an optimal parametrization within the time-constraints of this dissertation, advanced parameter estimation methods and potentially some structural changes could result in better parametrizations. Even qualitative predictions with sub-optimal parametrizations could provide insights about signaling mechanisms and can be used for experimental design. Overall, we anticipate that our proposed framework of the comprehensive

model will provide a sound starting point for development of more advanced and complex models of NF-κB signaling, and potentially other signaling pathways.

We can summarize this dissertation in three key takeaways. First, due to the combined effects of nonlinearity, variability and dynamic input stimuli, cells have a highly versatile repertoire of responses to the changing microenvironment. Cellular signaling therefore should be viewed through the lens of thermodynamic 'path functions' which define the dynamics of transition between two states, in contrast to 'state functions', which only consider the intrinsic characteristics of the states. Second, the information transmission across plasma membrane is a function of the identity of the signaling molecule and the number of its cognate receptors and corresponding adapter proteins. Stochasticity in number of receptors and associated proteins can limit this information transmission but it also allows for tuning a balance between fidelity to information and magnitude of the corresponding response. Third, dynamic stimuli generated with microfluidic systems can be used to take advantage of the versatility and stochasticity in cellular responses to manipulate the signaling outputs. Mechanistic models fitted to such experimental data can be used to predict such optimal stimuli, as well as to identify potent perturbations in signaling nodes, for desired response outcomes.

Appendix A

Supplementary material for chapter 2: Development of a microfluidic dynamic stimulation platform to probe cellular signaling

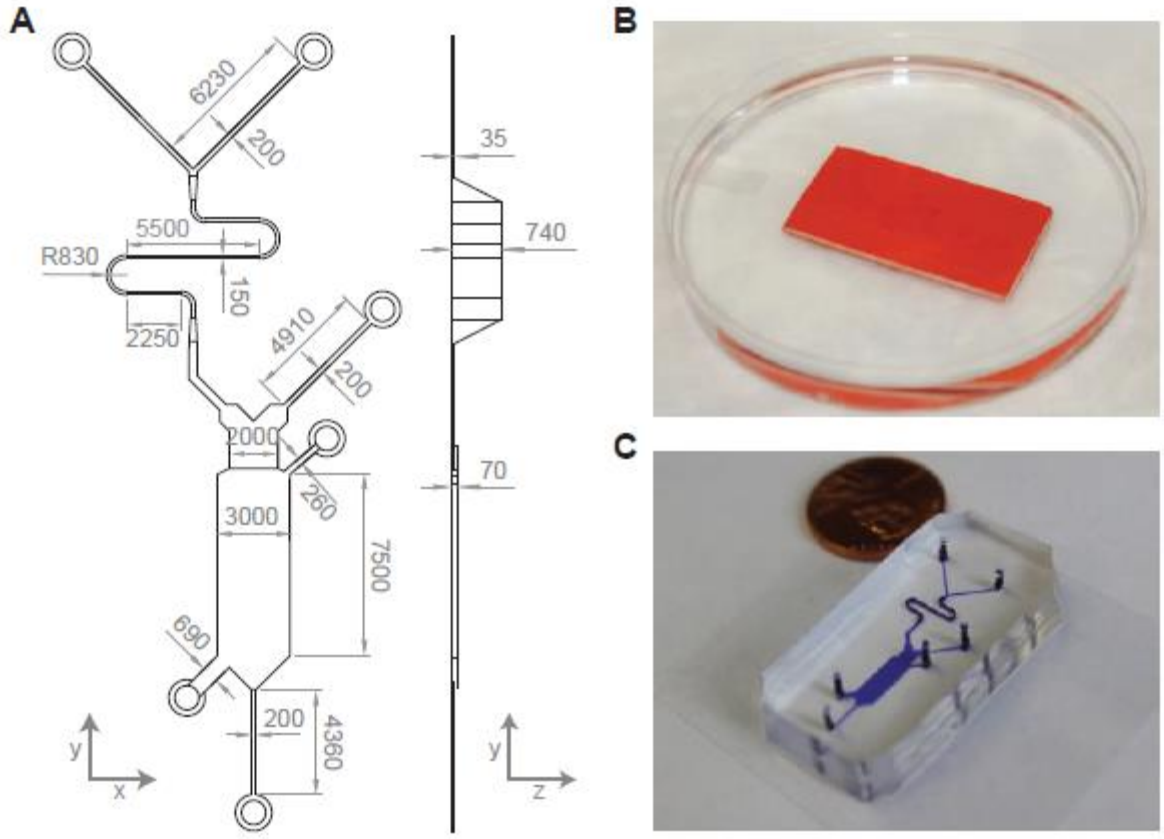

Figure A1: Design and fabrication of dynamic stimulation device

(A) Top-down (left) and relief (right) views of the dynamic stimulation device. All dimensions are in micrometers. (B) The 3D-printed mold is pasted to a petri dish and covered with PDMS mixed with a hardening agent. The cured PDMS relief is cut along the edges of the mold with a box cutter, carefully peeled from the mold, and bonded with a glass cover slip. (C) The completed device filled with a dye for visualization, coin provided for scale

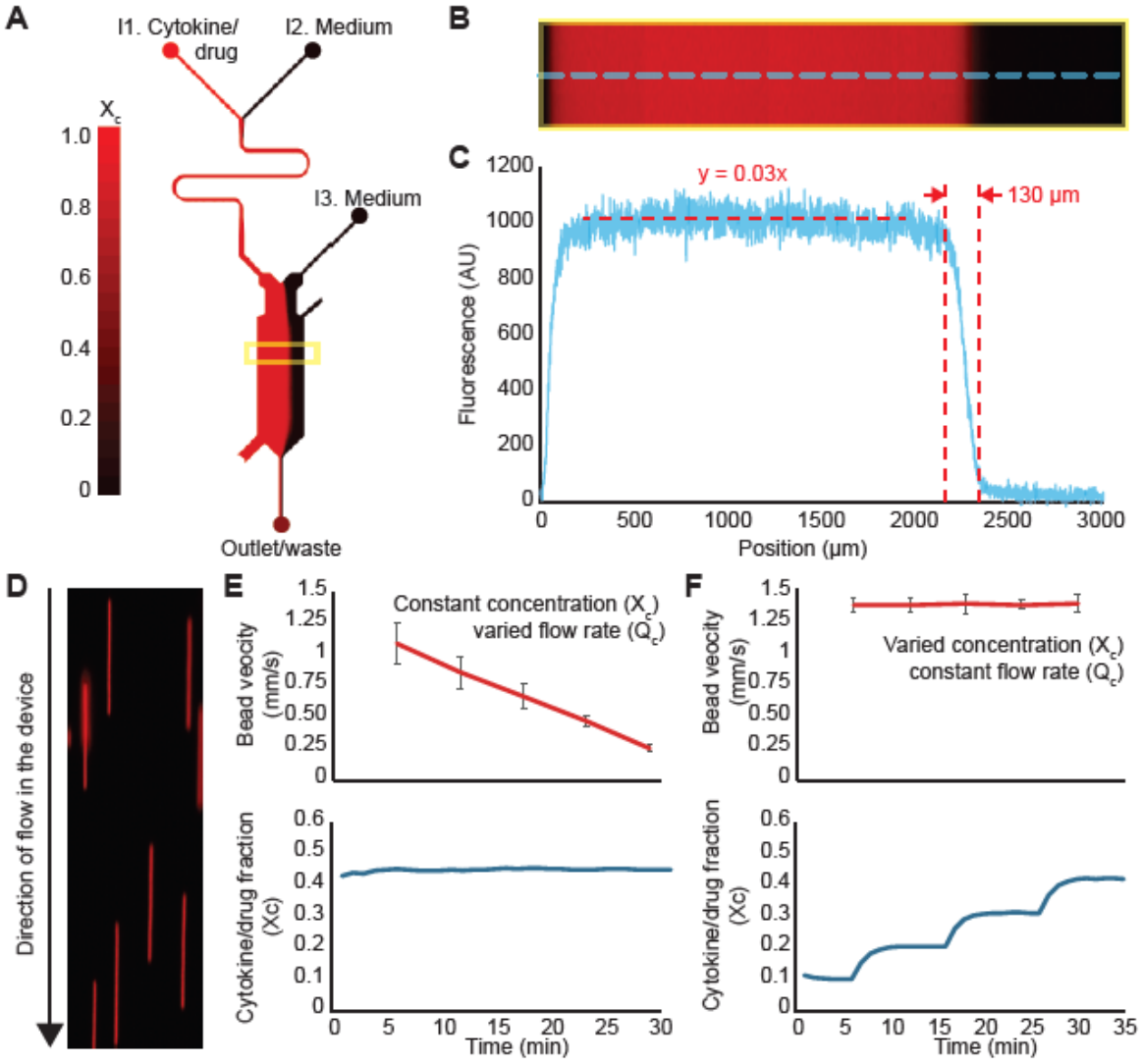

Figure A2. Characterization of mixing and flow rates within in the dynamic stimulation device

(A) Representative Ansys-Fluent simulation of the device with volume fraction of stimulus at inlet I1 is set to 1 and that at inlets I2 and I3 is set to 0. Many such simulations were performed with different inlet pressures (P1, P2 and P3) and corresponding inlet flow rates (Q1, Q2 and Q3) were used to fit the linear model. (B) Alexa647-conjugated BSA intensity was diluted through the mixer

and a panel of images were collected across a cross-section of the cell culture channel (depicted by yellow box in panel a). (C) Representative fluorescence of Alexa647-conjugated BSA was collected along a line scan (blue dotted line in panel B) shows an even distribution across ‘M’ and ‘E’ bands of the channel demonstrating nearly perfect mixing with a small diffusive region (< 150 μm) between the ‘E’ and ‘C’ bands. (D) Path lines of fluorescent tracer beads (FluoSpheres) used to measure the flow rate in the cell culture channel. Bead velocity is calculated by dividing the trace length by the exposure time of the microscope. (E) The flow rate, measured by bead velocity, can be independently controlled while keeping the concentration (Xc) of Alexa647-conjugated BSA unchanged. (F) Concentration of the stimulus in terms of Xc canbe independently controlled while keeping the flow rate unchanged. Error bars describe the standard deviation of 40 beads per data point on average.

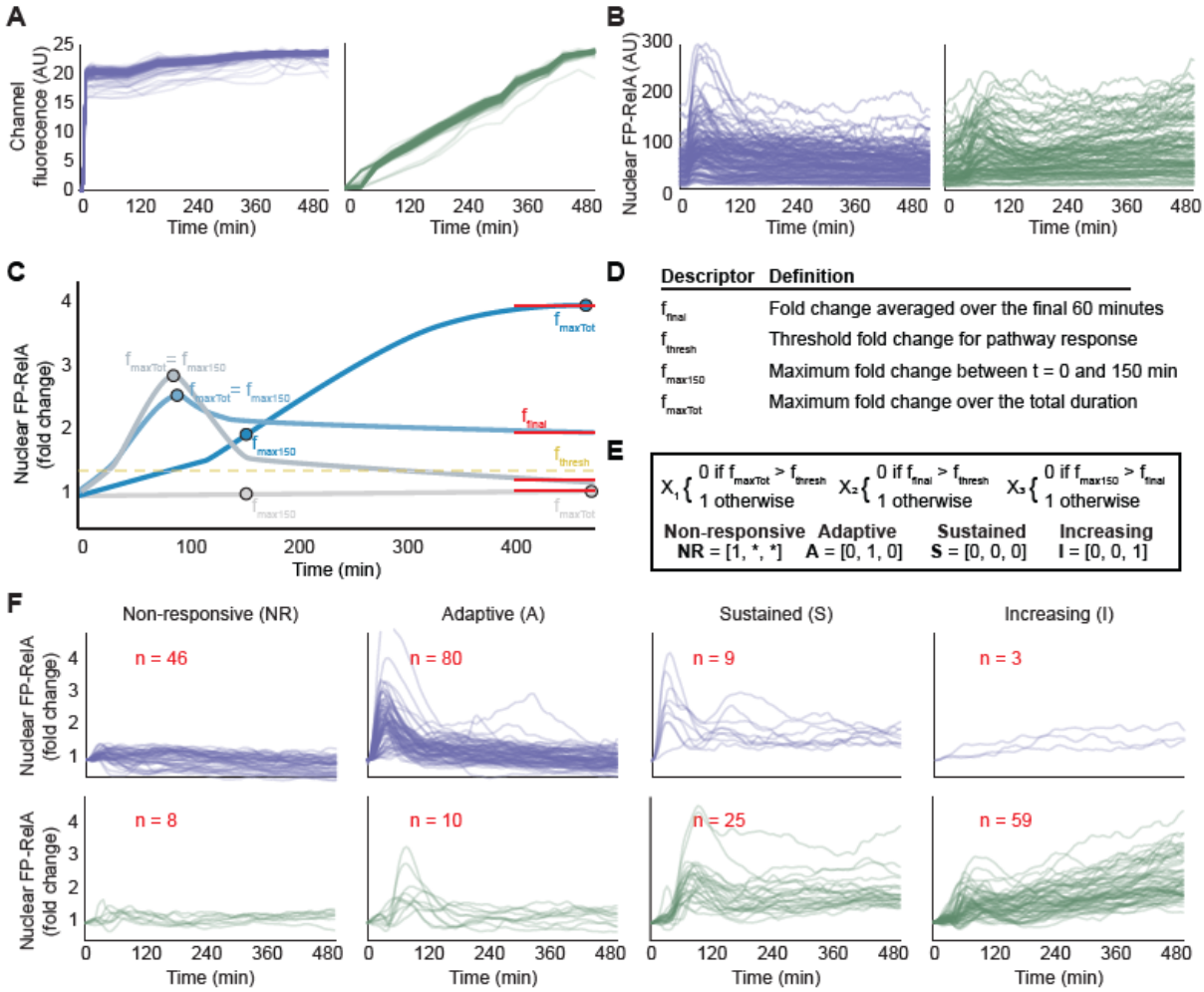

Figure A3. Categories of single-cell responses to 8h step and ramp stimulation

(A) Fluorescence intensity of Alexa 647-conjugated BSA was measured at every cell over 8 hours for step (left) and ramp (right) TNF treatment for a representative experiment. The fluorescence intensity was normalized to maximum to get fractional intensity, and used as proxy for volume fraction (Xc) of TNF concentration between 0 and 5ng/mL. (B) Raw time-course trajectories for nuclear FP-RelA for single cells exposed to step (left) and ramp (right) TNF conditions for a representative experiment. The same trajectories are plotted as nuclear fold change in Figure 4. (C) Example of quantitative descriptors extracted from illustrative single cell time courses of

nuclear FP-RelA fold change, defined in (D). (E) Each time course is represented as a vector of the form [X_1, X2, X3] and used to classify cells exposed to TNF as either non-responsive (NR), adaptive (A), sustained (S), and increasing (I). (F) Time courses of nuclear FP-RelA in (B) are classified into four categories as defined by the feature-based classification algorithm in (E). Insets show number of cells in each category for each condition.

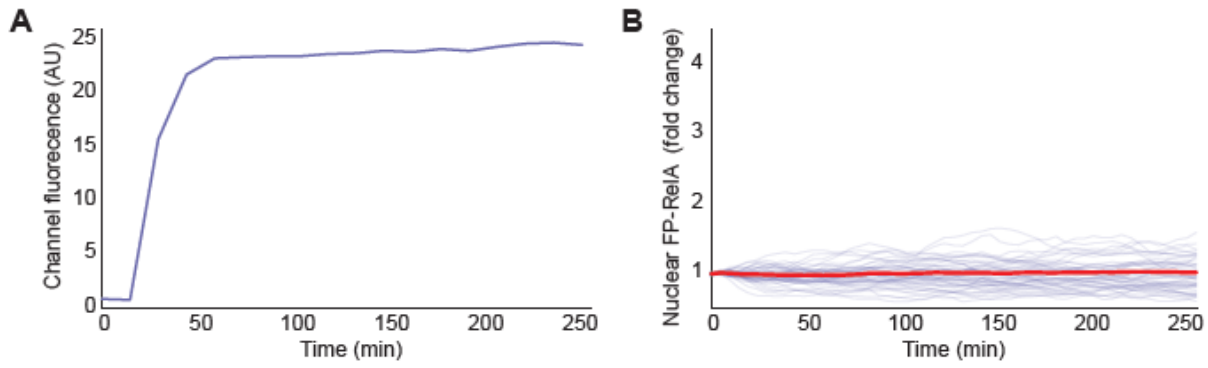

Figure A4. Responses to a mock step of Alexa 647-conjugated BSA but without TNF

(A) Fluorescence intensity of Alexa 647-conjugated BSA was measured in the cell culture channel in an experiment during a mock treatment, where cells were exposed to a step of BSA but were not exposed to TNF. (B) Average (red line) of 46 nuclear FP-RelA single cell time courses (purple lines) do not show evidence of mechanotransduction-dependent pathway activation.

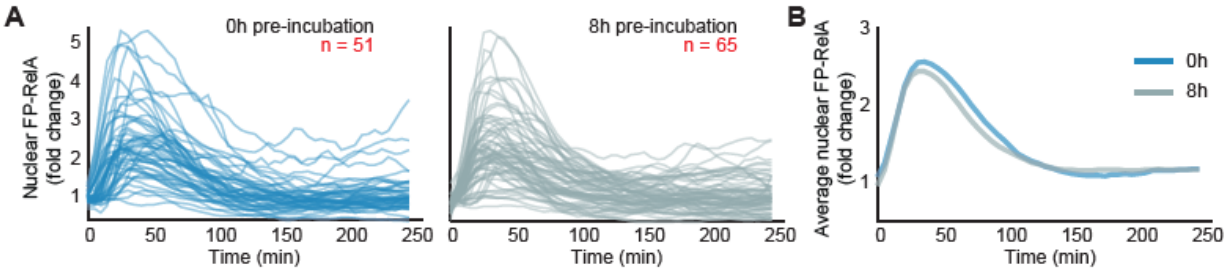

Figure A5. TNF retains bioactivity over the duration of experiments

(A) Time-course trajectories for nuclear FP-RelA in single cells exposed to a 5 ng/mL TNF step in a 96-well plate. TNF was prepared either immediately before cell stimulation (left, 0h) or 8-hours before cell stimulation (right, 8h) and incubated at room temperature. Red inset numbers indicate the number of single cell trajectories collected in each condition. (B) Average of single cell time-courses for nuclear FP-RelA demonstrate that TNF retains comparable bioactivity over an 8-hour duration.

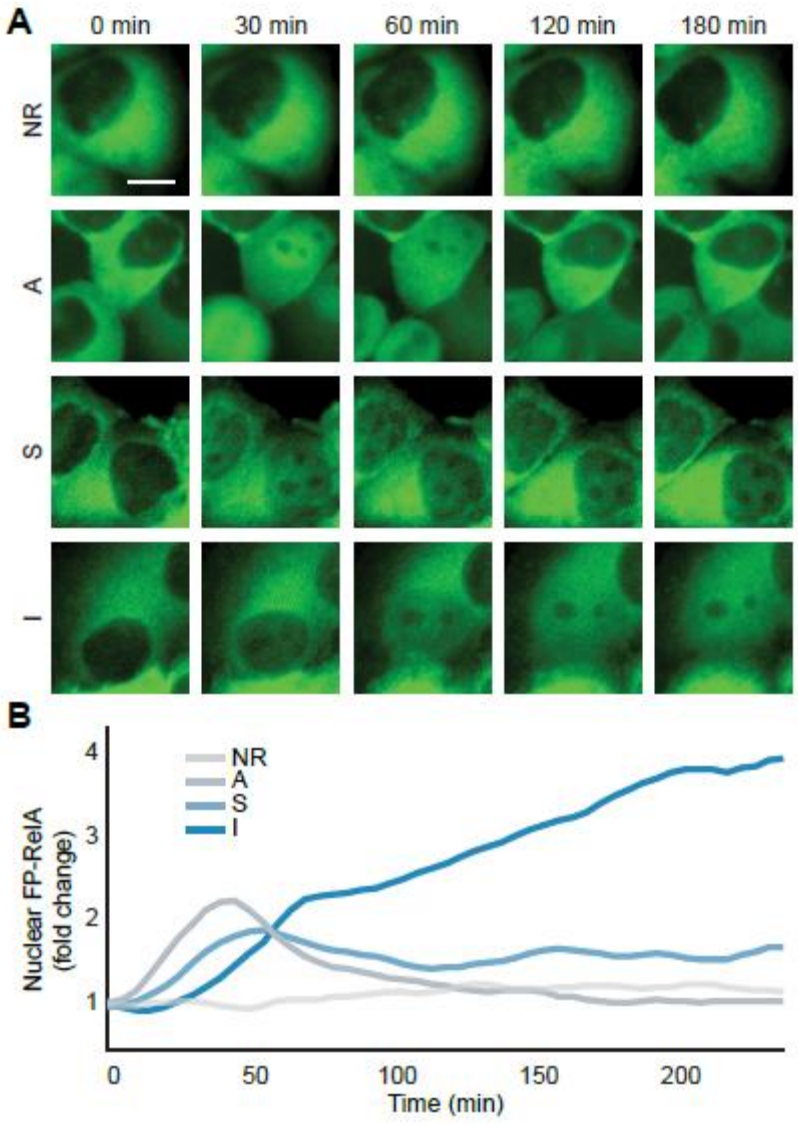

Figure A6. Example single cell trajectories for nuclear FP-RelA response categories, (A) Time-lapse images of FP-RelA-expressing HeLa cells illustrate non-responsive (NR), adaptive (A), sustained (S), and increasing (I) classifications in cells exposed to TNF. Scale bar is 10 μm. (B) Quantification of nuclear FP-RelA from single cells in panel A).

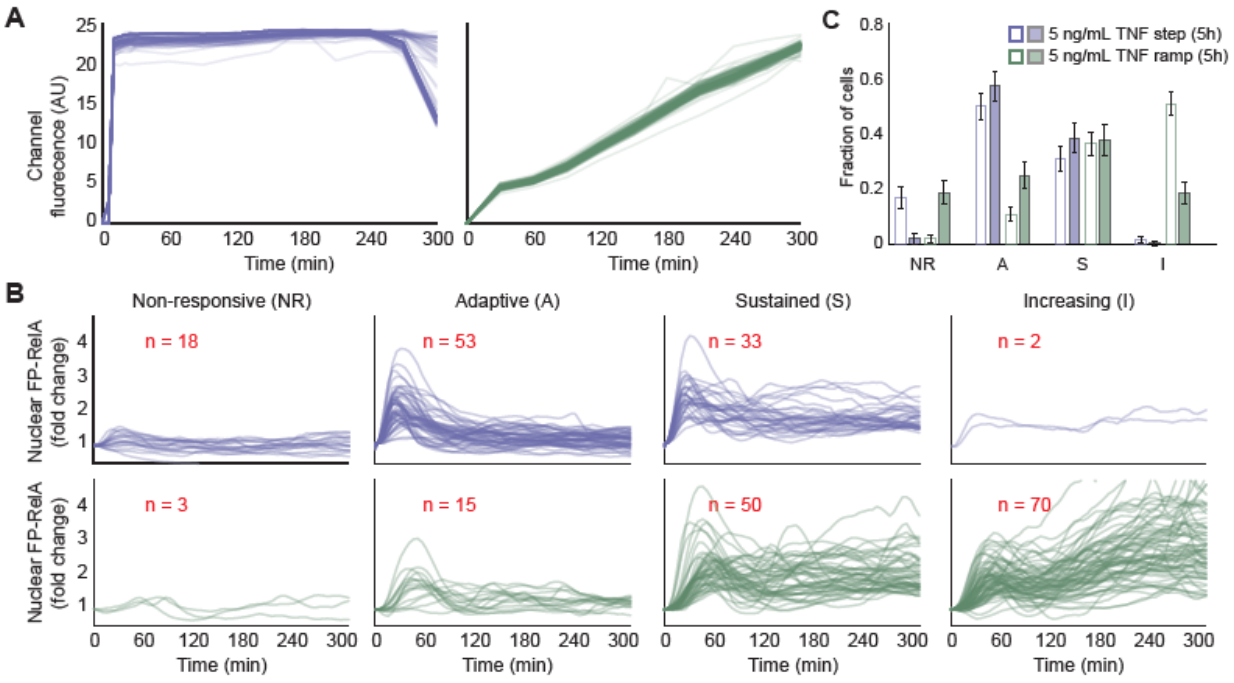

Figure A7. Responses to a 5-hour exposure to step or ramped TNF stimulation

Fluorescence intensity of Alexa 647-conjugated BSA was measured at every cell over 5 hours for (A) step (left) and ramp (right) TNF treatment in a representative experiment. The fluorescence intensity was normalized to maximum to get fractional intensity and used as proxy for volume fraction (Xc) of TNF concentration between 0 and a maximum of 5ng/mL. (B) Time courses of nuclear FP-RelA are classified into four categories: Non-responsive, Adaptive, Sustained, and Increasing, for continuous (top row) and ramp (bottom row) stimulation with TNF for a representative experiment. Insets show number of cells in each category for both conditions. (C) Quantification of the fraction of single cells in each category for 5-hour step and ramp stimulation shows show statistically significant differences in their distributions (p-value = 0.05; Pearson's chi-squared test). Biological duplicate data are shown as open and closed barss and show enrichment of the Increasing category after ramp stimulation as observed for an 8-hour ramp in Figure 4. Error bars represent standard deviation of 5000 bootstrap samples.

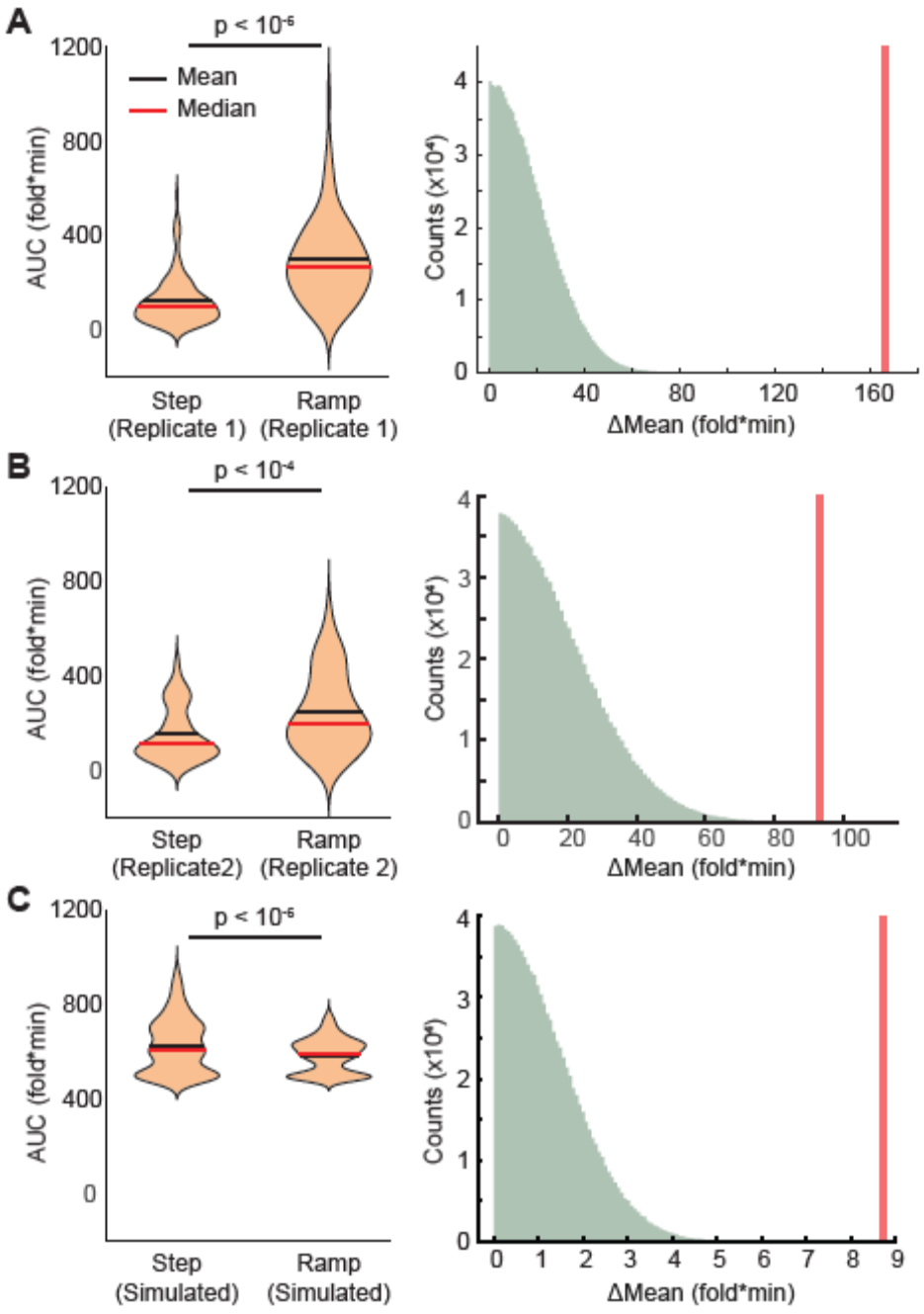

Figure A8. Ramp stimulation produces greater AUC responses

For each cell, the area under the curve (AUC) of nuclear FP-RelA response is calculated. Violin plots (left) and permutation test (right) showing a significant difference between the AUCs of fold change responses between 8h step and ramp stimuli for (A) biological replicate 1, (B) biological

replicate 2, and (C) simulated data (see figure 6). For permutation tests, AUC data from a step and ramp stimulation experiment are randomly permuted between groups without replacement and the difference between the means (ΔMean) of the permuted data is measured. Frequency histograms (right) depict ΔMean of the AUC for 10^6 permutations of the data. Red lines indicate the ΔMean of the original unpermuted data set. For (A) and (C), values of ΔMean for all permuted data sets are smaller than the ΔMean of the original unpermuted data demonstrating statistical significance with a p-value < 10-6 (two-tailed). For (B) the two-tailed p-value < 10-4 . We therefore reject the null hypothesis and accept the alternative for all three tests, that differences between the AUC of step and ramp data did not occur by chance.

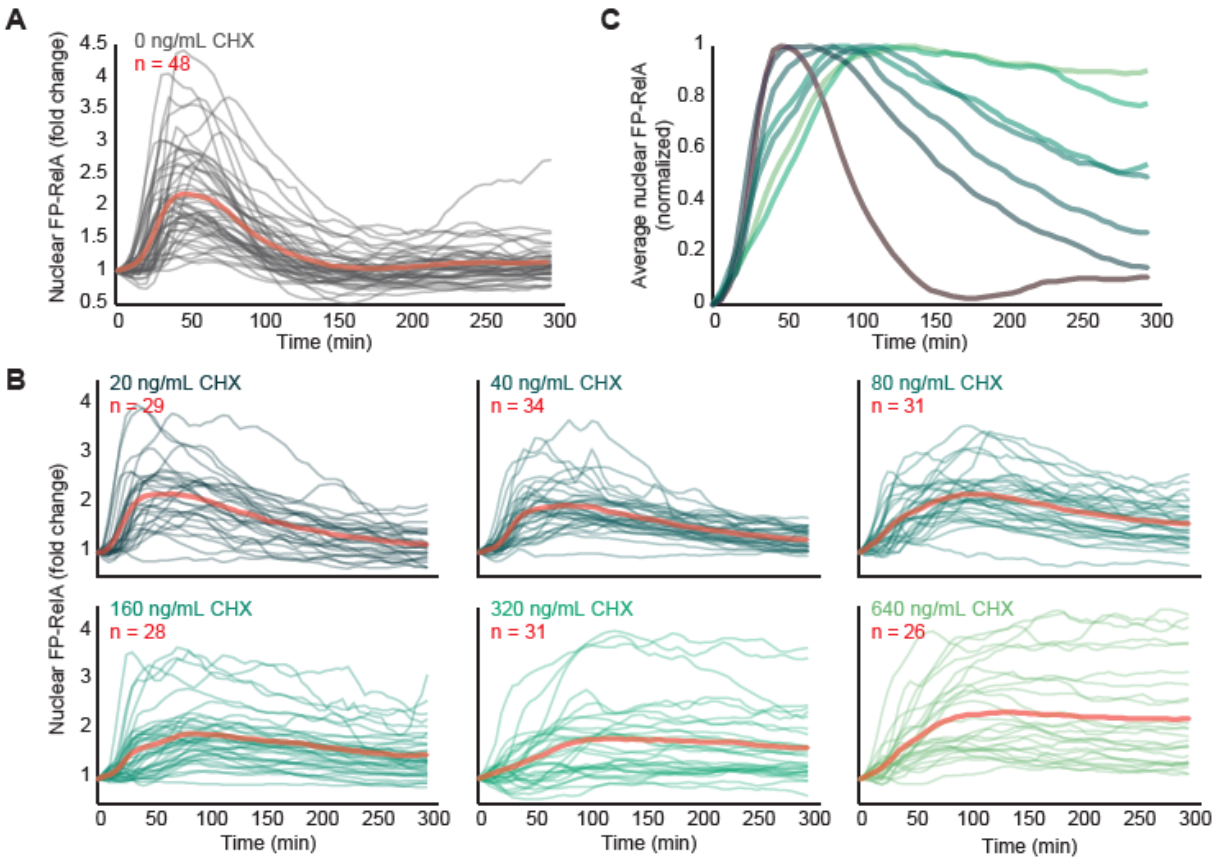

Figure A9. Nuclear FP-RelA trajectories in response to a TNF step are sustained in the presence of cycloheximide

(A) Time-course trajectories for nuclear FP-RelA in single cells exposed to a 5 ng/mL TNF step. Red line indicates the average of single cell responses. (B) Time-course trajectories for nuclear FP-RelA in single cells exposed to a 5 ng/mL TNF step in the presence of indicated concentration of cycloheximide (CHX, added 60 minutes before TNF stimulation). Significant cell death was observed in many conditions. Consequently, trajectories were only collected from cells that survived for at least 300 minutes after TNF exposure. Red line indicates the average of single cell responses for each condition. (C) Average of of single cell time-courses for each condition in panels A) and B). Nuclear FP-RelA is normalized for each condition to demonstrate differences in nuclear export of FP-RelA attributed to CHX-dependent inhibition of protein translation for

mediators of negative feedback. All CHX calibration experiments were performed in 96-well plates. Red inset numbers indicate the number of single cell trajectories collected in each condition.

Appendix B

Supplementary material for chapter 3: Dynamics of IKK-mediated transmission of cytokine signals in the NF-κB pathway

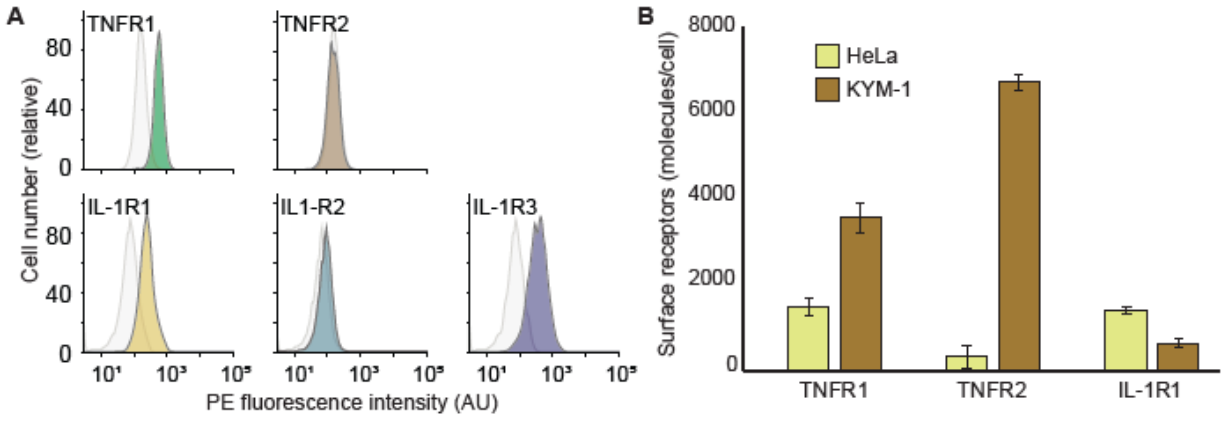

Figure B1: Quantification of surface receptors in U2OS, HeLa, and KYM-1 cells

(A) Flow-activated cell sorting (FACS) distributions for surface receptor expression. Unstimulated U2OS cells were stained for with PE-conjugated antibodies against indicated surface receptors. Semi-transparent histograms represent cells stained with negative isotype control antibodies. Surface receptor numbers were subsequently calculated using BD Quantibrite™ PE beads as standard curve. (B) Quantification of surface expression for TNFR1, TNFR2, and IL-1R1 was performed similarly with HeLa and KYM-1 cells for comparison with U2OS data and previously published results. The average of 3-7 biological replicates is shown for each condition. Error bars represent SEM.

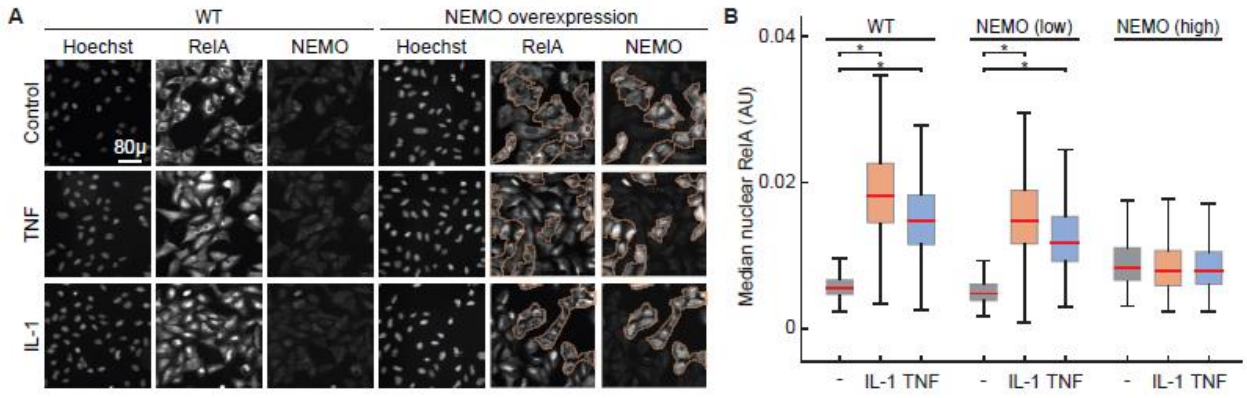

Figure B2: Overexpression of NEMO interferes with the downstream NF-κB **response**

(A) Fixed-cell images of U2OS cells stained with fluorescent antibodies against RelA and NEMO. Hoechst counterstain was used to identify nuclei. U2OS wild-type cells (WT) or U2OS stably transfected to overexpress NEMO were stimulated with TNF or IL-1 and translocation of RelA (NF-κB) was quantified in nuclei. For stable NEMO overexpression, two cell subpopulations were visible, one with near endogenous levels of expression and the other with high expression (marked with an orange perimeter). Scale bar represent 20µm for all. (B) Nuclear RelA abundance from fixed-cell images described in (A) using measurements from approximately 1000 single cells per condition. For both WT and NEMO-low cells, clear accumulation of nuclear RelA is observed in response to TNF and IL-1 ($p < 1015$; 1-tailed t test). However, in NEMO-high cells basal nuclear RelA was increased and cytokine stimulation did not induce nuclear translocation of RelA.

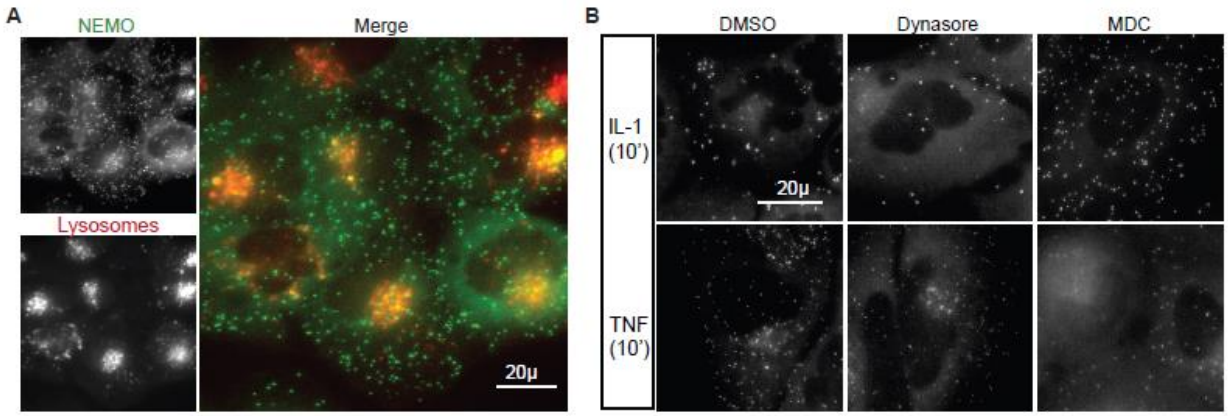

Figure B3: Endogenous fusion EGFP-NEMO proteins do not colocalize with lysosomal structures

(A) U2OS cells with endogenous EGFP-NEMO were preloaded with LysoTracker™ Blue DND-22 (ThermoFisher) and stimulated with IL-1 or TNF. Maximum intensity projections of 3D images demonstrate that EGFP-NEMO complexes do not co-localize with labeled lysosomes. (B) Endocytosis inhibitors do not interfere with formation of TNF- and IL-1- induced Nemo complexes. Cells were pre-exposed to indicated inhibitors for 20 minutes prior to addition of 100 ng/mL of cytokine for 10 minutes. Scale bars represents 20µm.

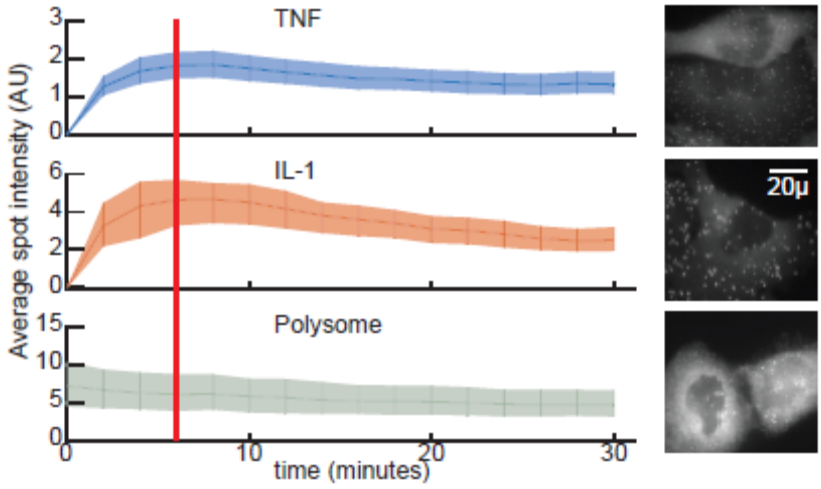

Figure B4: Polysome calibration to estimate numbers of EGFP-NEMO molecules per complex

U2OS EGFP-NEMO cells stimulated with 100ng/mL IL-1 or TNF were imaged by time-lapse microscopy. In parallel, HeLa cells expressing scFv-EGFP suntag and transfected with V4-PP7 to reveal polysomes (cells were provided by the Zhuang group and prepared as described in their original work (43)). Imaging conditions were identical for all. Polysome images, with a known number of EGFP molecules per spot were then used to calibrate the intensity of EGFP-NEMO complexes in TNF- or IL-1 stimulated cells at a time when cytokine-induced complexes are brightest (red line). The comparison enabled an estimation for the number of EGFP-NEMO molecules per CI-like complex. Representative maximum intensity projection images are shown for each. Scale bar represents 20µm.

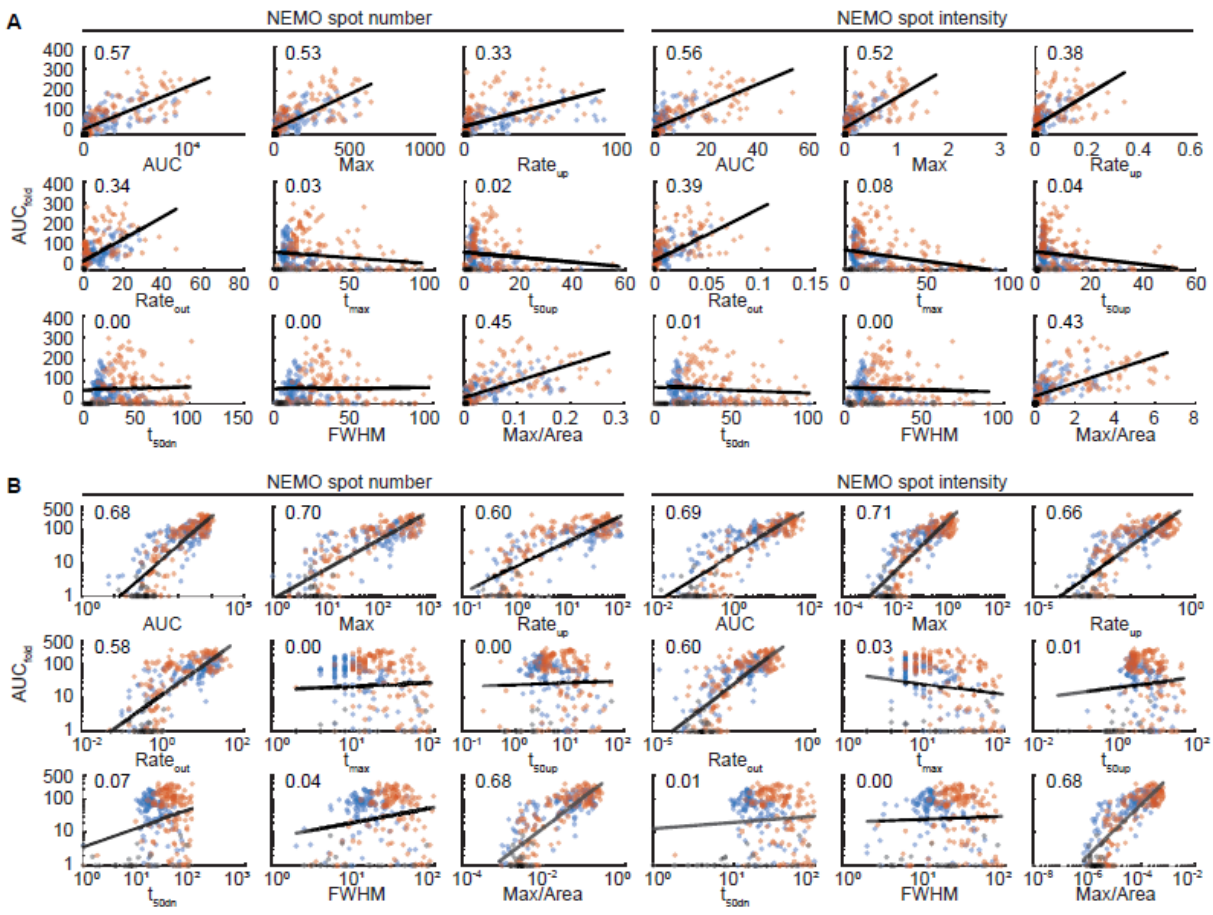

Figure B5: Same-cell coefficients of determination for descriptors of EGFP-NEMO and mCh-RelA dynamics

(A) Linear regression of descriptors of NEMO spot numbers (left) and aggregate spot intensities (right) against the area under the curve of the RelA fold change curve (AUCfold). NEMO descriptors in addition to those described in Fig. 3 in the main article include the Full Width Half Maximum (FWHM) in addition to descriptors normalized to the cell area. Although correlations are shown only against the AUCfold, each NEMO descriptor was calculated against each descriptor of RelA as shown in Figure 3.3 of the main article. (B) For comparison, coefficients of determination were calculated for log-transformed data. The descriptors with the strongest

coefficients of determination from linear data showed consistent improvement when data are log-transformed.

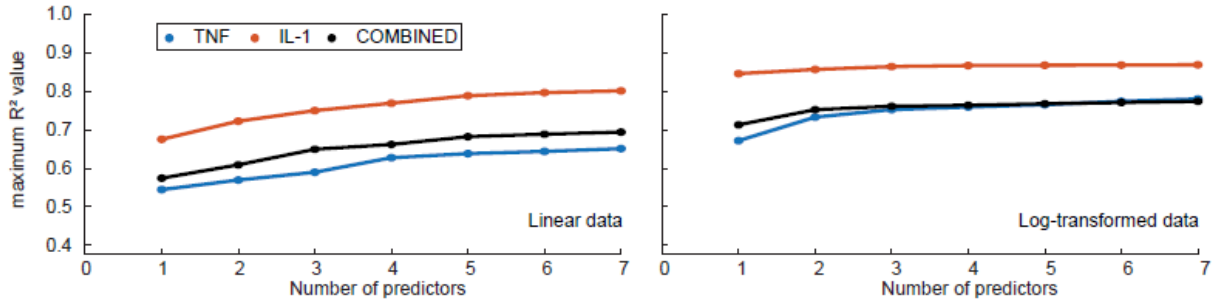

Figure B6: Multiple linear regression does not greatly increase determination between EGFP-NEMO and mCh-RelA.

The maximum R2 value for multiple linear regression analysis for descriptors of EGFPNEMO complexes against the AUC_{fold} of nuclear RelA. For untransformed linear data (left), multiple linear regression increases R2 values up to 7 predictors. However, even with 7 predictors, the R2 value is still lower than all R2 values for log-transformed data (right). For log-transformed data, inclusion of a second predictor showed modest improvements in R2 values. Beyond the second predictor, further improvements were marginal or non-existent.

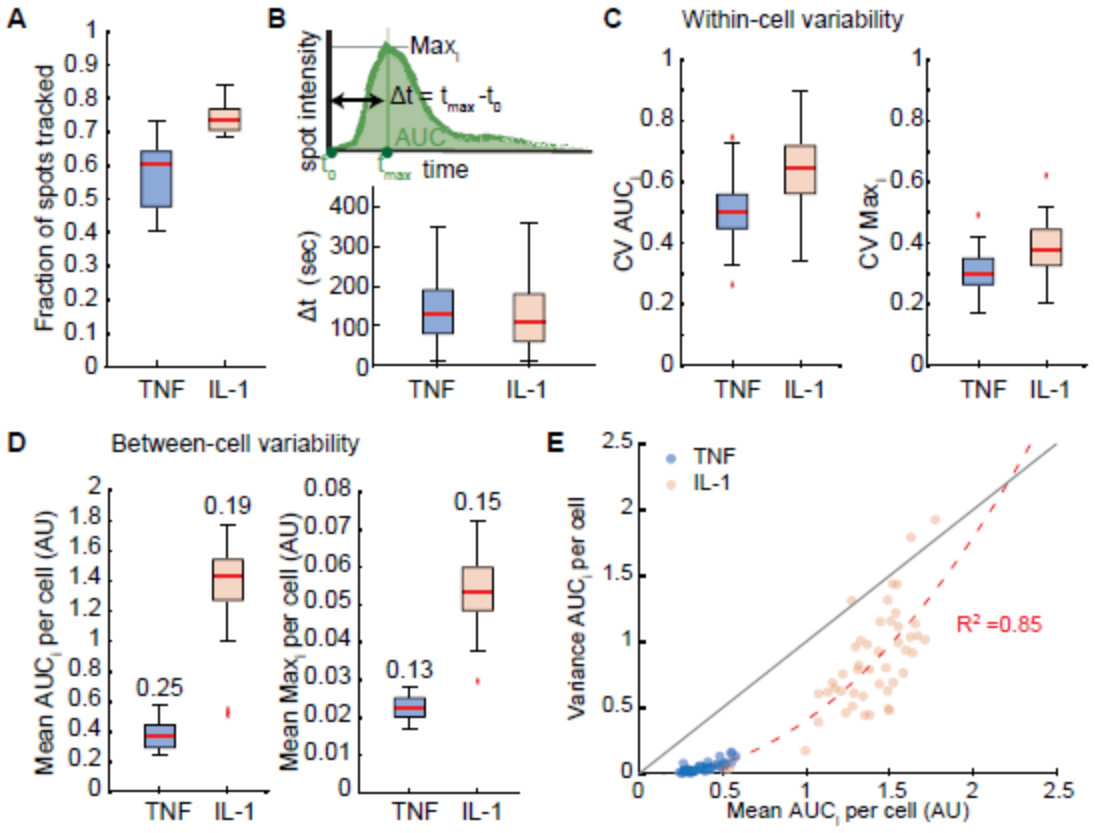

Figure B7: Tracked spots and their intra- and inter-cellular variability

(A) Boxplots (median and inter-quartile range) for the fraction of detected spots that belong to tracks across single cells. All experimental conditions were combined for each of TNF and IL-1. This analysis shows that approximately 60% of TNF-induced complexes and 75% of IL-1-induced complexes were represented by single-complex trajectories from tracking experiments. (B) Schematic of descriptors for single-complex trajectories include maximum intensity (Maxi), area under the curve of intensity (AUCi), and time of peak (Δt). The time of peak (Δt) is within three minutes of complex formation for both TNF and IL-1 responses. (C) Coefficients of variation were calculated for descriptors of all complex trajectories detected within the same cell. Boxplots are distributions of single-cell CV values among all cells for each of TNF and IL-1 responses. These data indicate that there is more within-cell variability for descriptors for IL-1-

induced complexes when compared with complexes formed in response to TNF. (D) The mean of descriptor values for all complex trajectories in a cell were calculated. The tight distributions for each of the TNF and IL-1-induced complexes (CV values are inset) indicate that the average of descriptors for single complex trajectories are remarkably similar between single cells. For both AUCi and Maxi, descriptors are 3-4 times lower for TNF-induced spots than IL-1-induced spots, which is consistent with biophysical differences between cytokine-induced spots described in Fig. 2 of the main article. (E) For single cells, the plot between mean and variance of AUCi of all spots within a cell follows a quadratic relation. This result suggests that as single complexes become larger and longer-lived in a cell, the corresponding variance between single spots in a cell increases multiplicatively. In general, both TNF and IL-1treated cells fall below the y=x line indicating sub-Poisson noise.

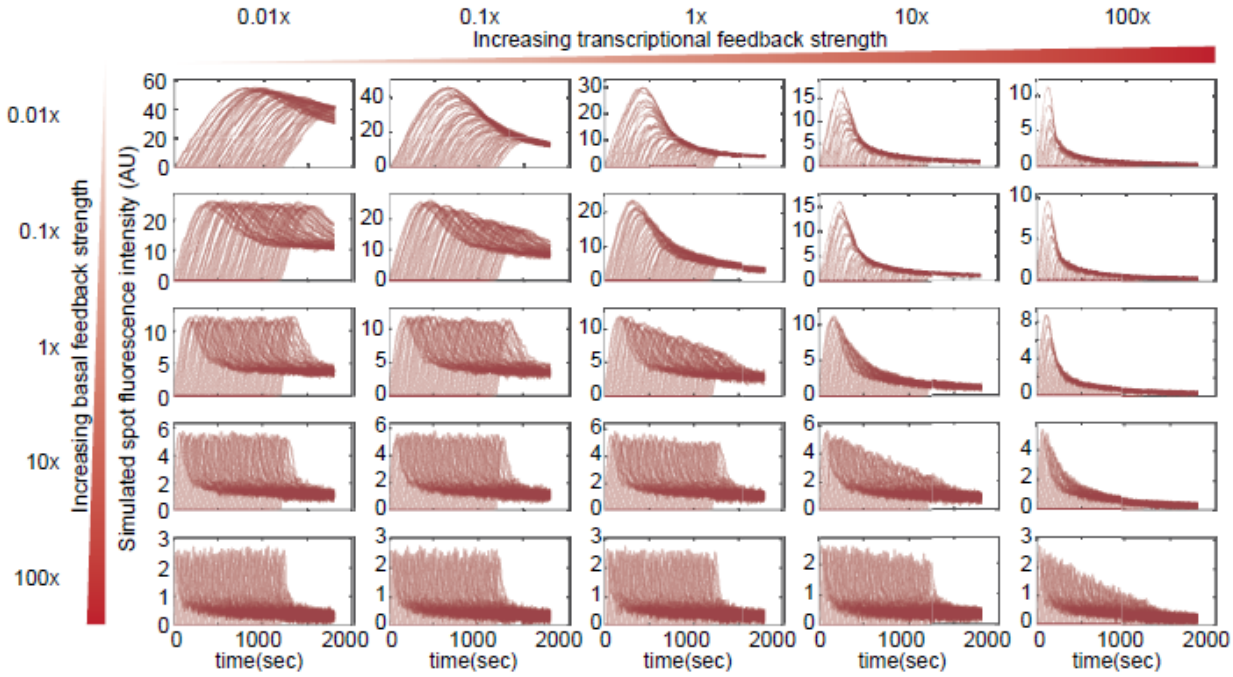

Figure B8: Simulations of transcriptional and basal negative feedback on single complex NEMO time courses.

Matrix of simulations of individual EGFP-complex trajectories using the HyDeS model in Fig. 5A. Parameter sweeps for increasing strength of transcriptional feedback (left to right) and increasing basal feedback (top to bottom) were used to observe trends in single complex trajectories that form in regular intervals after cytokine stimulation. For both sources of negative feedback, increasing feedback strength reduces the maximum intensity and AUC of each complex. Negative feedback through transcription uniquely causes late-forming complex trajectories with maximum intensity and AUC that are lower than early-forming complexes in the same simulation. Although basal negative feedback alters properties such as the sharpness of a trajectory, it operates identically on early and late-forming complexes in the same simulation.

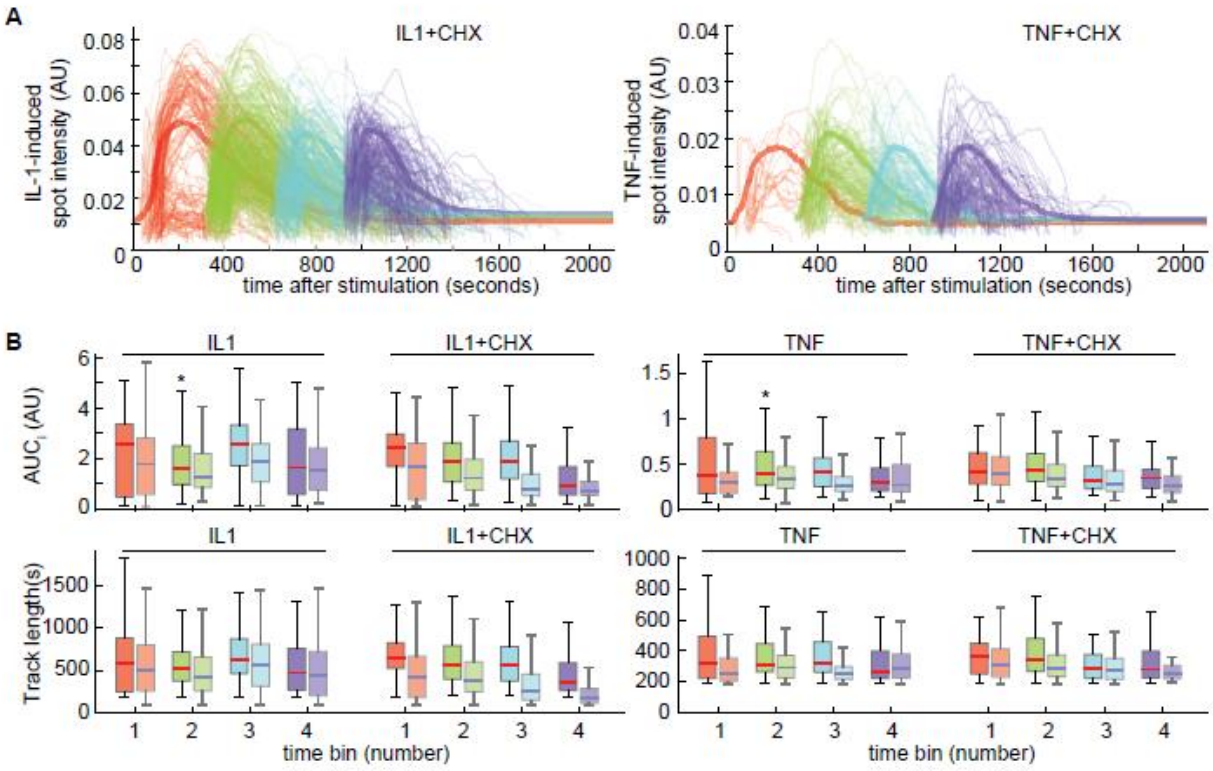

Figure B9: Experiments do not support transcription as the predominant source of negative feedback on NEMO complexes during the primary cytokine response

(A) Reverse time course experiment testing the effect of transcriptional feedback in trajectories of NEMO complexes. U2OS EGFP-NEMO cells were pretreated for 20 minutes with 50 ng/mL CHX and then stimulated with IL-1 (left) or TNF (right). High frequency images were collected with the following delay after stimulation: 0 minutes (red), 5 minutes (green), 10 minutes (cyan), or 15 minutes (purple). Only new spots that formed within the first 2 minutes of imaging were tracked to allow direct comparison between early and later-forming EGFP-NEMO complexes. (B) Boxplots (median and inter-quartile range) of descriptors of EGFP-NEMO complexes trajectories after stimulation with IL-1 (left) or TNF (right) in cells pretreated with DMSO or CHX. Biological replicates are shown side-by-side with transparency. In nearly all comparisons with early forming spots (red bin), later forming spots (green, cyan, and purple bins) do not show

significant increases (p-value >> 0.05, left-handed t-test) as predicted by the model where transcriptional negative feedback is predominant.

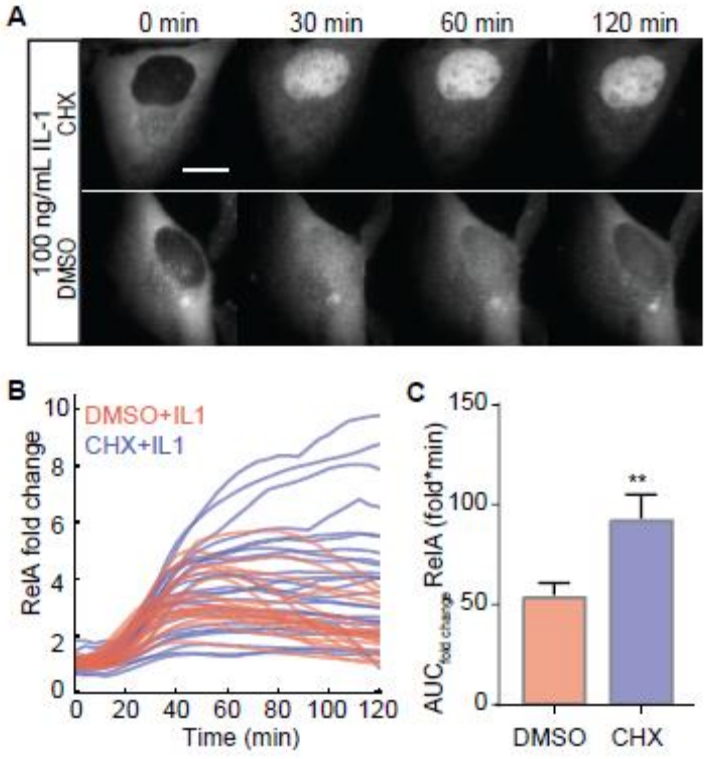

Figure B10: Validation that CHX concentrations are sufficient to inhibit translation.

(A) Representative images of mCh-RelA in cells pretreated with DMSO or CHX (50 ng/mL) for 20 minutes and then stimulated with IL-1. Scale bar represents 20μm. (B) Single cell time courses collected as described in (D). Cells were pretreated with DMSO (peach color) or 50 ng/mL CHX (blue) 20 minutes before stimulation with IL-1. Single-cell time-courses of nuclear RelA do not show appropriate nuclear export in the presence of CHX indicating disruption of IkBα expression. Although IKK trajectories could be measured in cells stimulated with CHX and TNF, all cells would undergo apoptosis between 60- and 120-minutes disrupting NF-κB time courses yet providing further evidence of chemical efficacy for CHX. (C) Bar graphs of AUC_{fold} for trajectories in panel (A) demonstrate that co-stimulation with CHX significantly increases nuclear RelA over the time-course (p-value << 0.05, t-test). These observations are consistent

with previous data (60), and together indicate that the NF-κB inhibitory protein IκBα is not being expressed as part of the normal NF-κB transcriptional response.

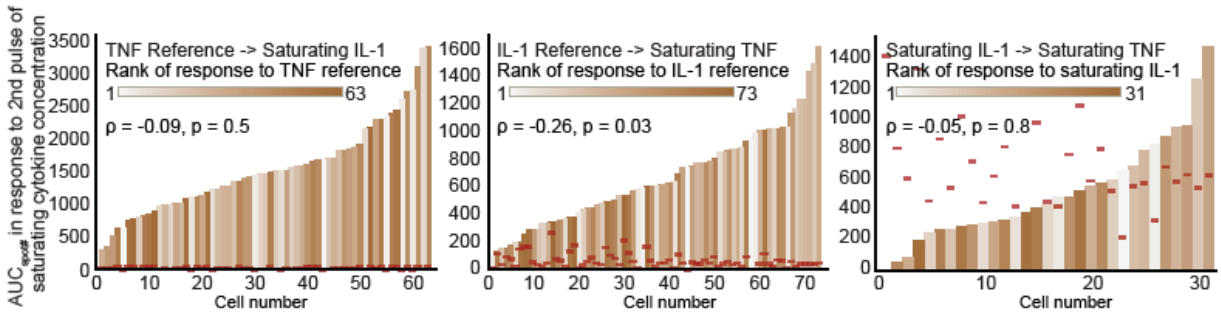

Figure B11: Single cell correlations are weak for cross-pulse stimulation experiments

Single cells were rank-ordered by their response to first cytokine stimulation and correlated with their CImax values for secondary stimulation. Responses to low concentration TNF (left) and IL-1 (middle) followed by a pulse of saturating concentration for the alternate cytokine are shown. Saturating cross-pulses (right) are also shown. Inset numbers indicate comparatively weak Spearman's rank correlation (ρ) and associated p-values.

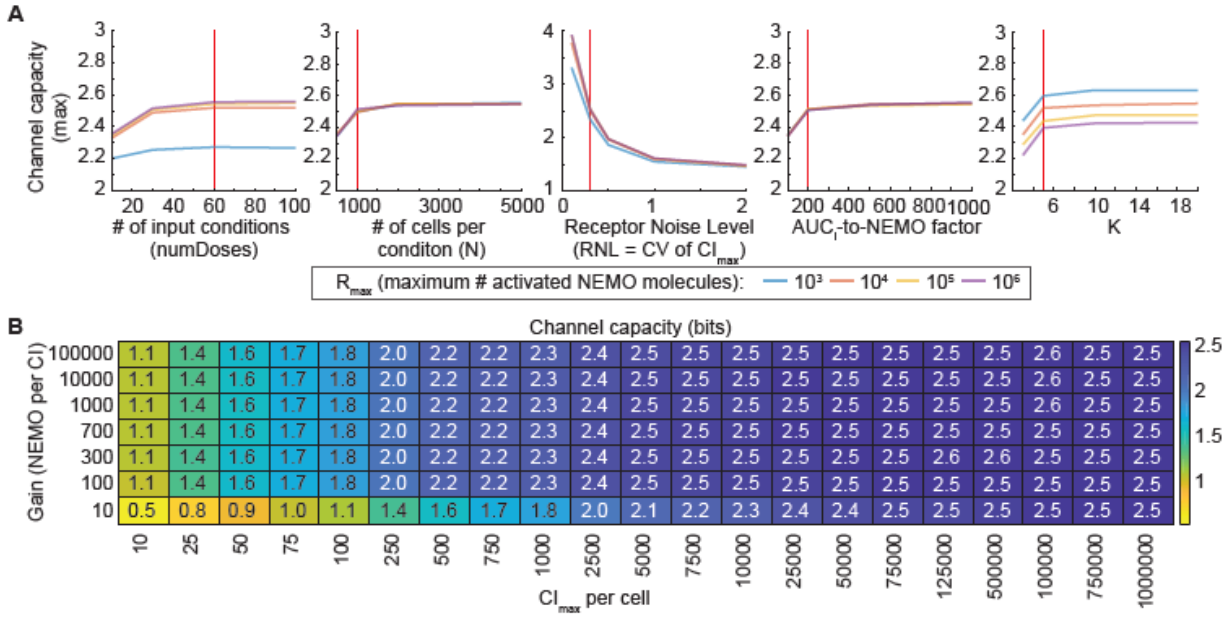

Figure B12: Hyper-parameter tuning for channel capacity calculations from the variable-gain stochastic pooling network model

(A) Variation of maximum channel capacity as a function of different hyperparameters in the VG-SPN model. Values of the five hyper parameters were tuned to avoid technical biases in the channel capacity calculation. Vertical red lines indicate the value of the hyperparameter used for final model simulations. See supplementary methods for more details. (B) Numerical values of channel capacity in bits are presented to accompany Fig. 6E. Although the 'shape' of relationship for different configurations of CImax and gain is consistent between noise models and value of stdR (presented as 'normalized' data in Fig. 6E), the absolute value of the channel capacity in bits is highly dependent on choices for these values. We therefore present bit depth values for reference, but do not contend that the values directly represent capabilities of the biological system.

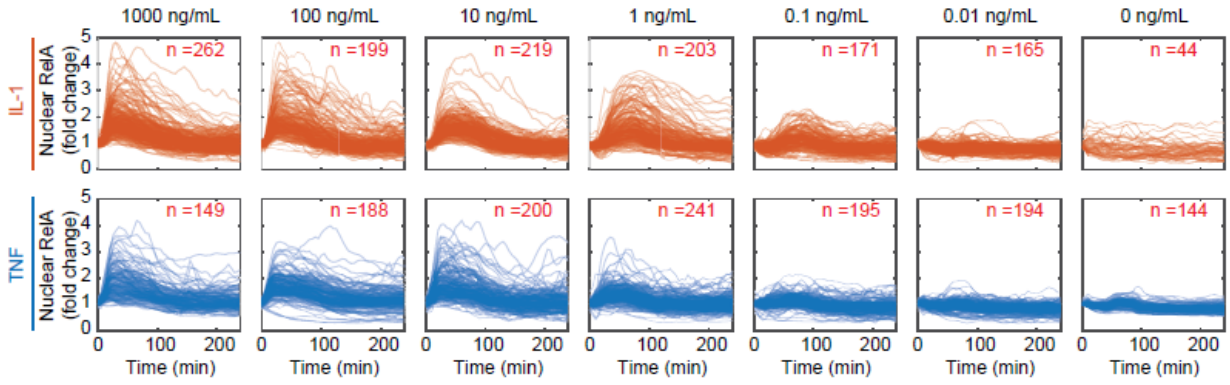

Figure B13. Dose-response of nuclear RelA used for channel capacity calculations

Single-cell time-courses of nuclear RelA in cells treated with indicated concentrations of IL-1 (top) or TNF (bottom). Inset number indicates the number of single cell time-courses in each condition.

Table B 1: Summary of aggregate number of cells and aggregate number of EGFP-NEMO complexed detected

Stimulation	# cells	# puncta
TNF - 0.1 ng/mL	33	3635
TNF - 1 ng/mL	19	20565
TNF - 10 ng/mL	31	36213
TNF - 100 ng/mL	32	80748
TNF - 1000 ng/mL	14	61106
IL-1 - 0.1 ng/mL	37	11899
IL-1 - 1 ng/mL	42	38389
IL-1 - 10 ng/mL	31	87966
IL-1 - 100 ng/mL	35	172138
IL-1 - 1000 ng/mL	23	152105

Table B 2: Summary of aggregate cell numbers for same cell measurements of EGFPNEMO and mCh-RELA

Condition	# cells
Unstimulated	28
TNF - 0.1 ng/mL	23
TNF - 1 ng/mL	19
TNF - 10 ng/mL	18
TNF - 100 ng/mL	21
TNF - 1000 ng/mL	22
IL-1 - 0.1 ng/mL	27
IL-1 - 1 ng/mL	26
IL-1 - 10 ng/mL	21
IL-1 - 100 ng/mL	19
IL-1 - 1000 ng/mL	23

Table B 3: Description of variables used in the HyDeS model for NEMO spot intensity

Variable Name	Description
I_i	Intensity of 'i'th spot, proxy for NEMO recruitment at that spot
X_basal_i	Basal feedback variable corresponding to 'i'th spot, proxy for feedback through basal/local DUB activity
X_trnsxl	Transcriptional feedback variable, proxy for feedback through aggregate activity of all NEMO spots

Table B 4: Description and values for parameters used in the HyDeS model of NEMO spot intensity

Parameter	Description	Default value
P_{form}	Probability that the spot is formed as a function of time. Once formed, the spot is assumed to stay active.	Modeled as uniform distribution i.e. N spots form at regular intervals during the modeling time scale.
P_{bound}	Probably that the ligand stays bound to the receptor and the complex is actively recruiting NEMO.	0.9
K_{growth}	Michaelis-Menton like intrinsic rate of Ub polymerization	$1.12*10^{-7}$
K_{limit}	Michaelis-Menton like kinetic constant to limit intrinsic polymerization with increasing spot intensity	0.1
Kd_{basal}	Rate of basal feedback activity on individual spots	0.032
Kd_{trnsxl}	Rate of transcriptional feedback activity on individual spots	0.08
Kx_{basal}	Rate of activation of basal feedback due to Ub polymerization and DUB recruitment at the given spot	23.3
Kxd_{basal}	Decay rate of basal feedback	$8.7*10^{-4}$
Kx_{trnsxl}	Rate of activation of transcriptional feedback due to collective activity of all NEMO spots	0.08
Kxd_{trnsxl}	Decay rate of transcriptional feedback	$1.5*10^{-5}$

Table B 5: Description of variables used in the VG-SPN model

Variable	Description	Formula
CI_{max}	Maximum number of CI complexes that a cell can form at saturation	Independent variable
Gain	Number of NEMO molecules recruited by a CI complex	Independent variable
CI_{max_j}	CI_{max} corresponding to 'j'th cell	$CI_{max_j} \sim \mathcal{N}(CI_{max}, RNL * CI_{max})$
P_{form}	Probability of complex formation as a function of input dose level S_i	$P_{form} = \frac{(1+0.5) * S_i^3}{0.5 + S_i^3}$
$CI^*_{max_j}$	Number of CI complexes formed in response to a given input dose level in 'j'th cell	$CI^*_{max_j} \sim Binomial\left(CI_{max_j}, P_{form}\right)$
G_k	Gain associated with 'k'th complex within a cell	$G_k \sim \mathcal{N}(Gain, GNL * Gain)$
GNL	Coefficient of variation of Gains associated with different CI complexes within a cell	GNL = 0.495*Gain^2 – 0.096*Gain + 0.05 (where Gain is in terms of AUC_i)

Table B 6: Description and values for hyperparameters used in the VG-SPN model

Hyperparameter	Description	Value
numDoses	Number of discrete input dose levels used to simulate the model response	60
N	Number of cells simulated for each input dose level	1000
RNL	Receptor noise level in terms of coefficient of variation in CI_{max} across cells	0.3
AUC_i_to_NEMO_factor	Factor to convert integrated intensity (AUCi) of observed CI spots into number of NEMO molecules recruited at that complex	200
K	Value of K used for K-nn classification in the framework developed by (2)	5

Bibliography

1. Spencer, S.L., et al., *Non-genetic origins of cell-to-cell variability in TRAIL-induced apoptosis.* Nature, 2009. **459**(7245): p. 428-32.
2. Lee, R.E., et al., *NF-kappaB signalling and cell fate decisions in response to a short pulse of tumour necrosis factor.* Sci Rep, 2016. **6**: p. 39519.
3. Purvis, J.E., et al., *p53 dynamics control cell fate.* Science, 2012. **336**(6087): p. 1440-4.
4. Ryu, H., et al., *Frequency modulation of ERK activation dynamics rewires cell fate.* Mol Syst Biol, 2016. **12**(4): p. 866.
5. Purvis, J.E. and G. Lahav, *Encoding and decoding cellular information through signaling dynamics.* Cell, 2013. **152**(5): p. 945-56.
6. Albeck, J.G., G.B. Mills, and J.S. Brugge, *Frequency-modulated pulses of ERK activity transmit quantitative proliferation signals.* Mol Cell, 2013. **49**(2): p. 249-61.
7. Taniguchi, K. and M. Karin, *NF-kappaB, inflammation, immunity and cancer: coming of age.* Nat Rev Immunol, 2018. **18**(5): p. 309-324.
8. Kim, E.K. and E.J. Choi, *Pathological roles of MAPK signaling pathways in human diseases.* Biochim Biophys Acta, 2010. **1802**(4): p. 396-405.
9. Clevers, H. and R. Nusse, *Wnt/beta-catenin signaling and disease.* Cell, 2012. **149**(6): p. 1192-205.
10. Ashall, L., et al., *Pulsatile stimulation determines timing and specificity of NF-kappaB-dependent transcription.* Science, 2009. **324**(5924): p. 242-6.
11. Fox, Z.R., G. Neuert, and B. Munsky, *Optimal Design of Single-Cell Experiments within Temporally Fluctuating Environments.* Complexity, 2020. **2020**.
12. Jashnsaz, H., et al., *Diverse Cell Stimulation Kinetics Identify Predictive Signal Transduction Models.* iScience, 2020. **23**(10): p. 101565.
13. Jashnsaz, H., et al., *Building predictive signaling models by perturbing yeast cells with time-varying stimulations resulting in distinct signaling responses.* STAR Protoc, 2021. **2**(3): p. 100660.
14. Whitesides, G.M., *The origins and the future of microfluidics.* Nature, 2006. **442**(7101): p. 368-73.
15. Jeon, N.L., et al., *Generation of Solution and Surface Gradients Using Microfluidic Systems.* Langmuir, 2000. **16**(22): p. 8311-8316.
16. Mehling, M. and S. Tay, *Microfluidic cell culture.* Curr Opin Biotechnol, 2014. **25**: p. 95-102.
17. Lee, P.J., T.A. Gaige, and P.J. Hung, *Dynamic cell culture: a microfluidic function generator for live cell microscopy.* Lab Chip, 2009. **9**(1): p. 164-6.

18. Kuczenski, B., P.R. LeDuc, and W.C. Messner, *Pressure-driven spatiotemporal control of the laminar flow interface in a microfluidic network.* Lab Chip, 2007. **7**(5): p. 647-9.

19. Takayama, S., et al., *Selective chemical treatment of cellular microdomains using multiple laminar streams.* Chem Biol, 2003. **10**(2): p. 123-30.

20. Chen, P., et al., *Microfluidic Chemical Function Generator for Probing Dynamic Cell Signaling.* Anal Chem, 2017. **89**(17): p. 9209-9217.

21. Piehler, A., et al., *Universal signal generator for dynamic cell stimulation.* Lab Chip, 2017. **17**(13): p. 2218-2224.

22. Thiemicke, A., et al., *Generating kinetic environments to study dynamic cellular processes in single cells.* Sci Rep, 2019. **9**(1): p. 10129.

23. Kellogg, R.A., et al., *Digital signaling decouples activation probability and population heterogeneity.* Elife, 2015. **4**: p. e08931.

24. Gale, B.K., et al., *A Review of Current Methods in Microfluidic Device Fabrication and Future Commercialization Prospects.* Inventions, 2018. **3**(3): p. 60.

25. Hayden, M.S. and S. Ghosh, *Shared principles in NF-kappaB signaling.* Cell, 2008. **132**(3): p. 344-62.

26. Zhang, Q., M.J. Lenardo, and D. Baltimore, *30 Years of NF-kappaB: A Blossoming of Relevance to Human Pathobiology.* Cell, 2017. **168**(1-2): p. 37-57.

27. Hoffmann, A., et al., *The IkappaB-NF-kappaB signaling module: temporal control and selective gene activation.* Science, 2002. **298**(5596): p. 1241-5.

28. Kearns, J.D., et al., *IkappaBepsilon provides negative feedback to control NF-kappaB oscillations, signaling dynamics, and inflammatory gene expression.* J Cell Biol, 2006. **173**(5): p. 659-64.

29. Micheau, O. and J. Tschopp, *Induction of TNF receptor I-mediated apoptosis via two sequential signaling complexes.* Cell, 2003. **114**(2): p. 181-90.

30. Lin, S.C., Y.C. Lo, and H. Wu, *Helical assembly in the MyD88-IRAK4-IRAK2 complex in TLR/IL-1R signalling.* Nature, 2010. **465**(7300): p. 885-90.

31. Besse, A., et al., *TAK1-dependent signaling requires functional interaction with TAB2/TAB3.* The Journal of Biological Chemistry, 2007. **282**(6): p. 3918-3928.

32. Jackson-Bernitsas, D.G., et al., *Evidence that TNF-TNFR1-TRADD-TRAF2-RIP-TAK1-IKK pathway mediates constitutive NF-kappaB activation and proliferation in human head and neck squamous cell carcinoma.* Oncogene, 2007. **26**(10): p. 1385-1397.

33. Ahmad, R., J. Sylvester, and M. Zafarullah, *MyD88, IRAK1 and TRAF6 knockdown in human chondrocytes inhibits interleukin-1-induced matrix metalloproteinase-13 gene expression and promoter activity by impairing MAP kinase activation.* Cell Signal, 2007. **19**(12): p. 2549-57.

34. Wertz, I.E., et al., *De-ubiquitination and ubiquitin ligase domains of A20 downregulate NF-kappaB signalling.* Nature, 2004. **430**(7000): p. 694-9.

35. Komander, D. and M. Rape, *The ubiquitin code.* Annu Rev Biochem, 2012. **81**: p. 203-29.

36. Tarantino, N., et al., *TNF and IL-1 exhibit distinct ubiquitin requirements for inducing NEMO-IKK supramolecular structures.* J Cell Biol, 2014. **204**(2): p. 231-45.

37. Pabon, N.A., et al., *A network-centric approach to drugging TNF-induced NF-kappaB signaling.* Nat Commun, 2019. **10**(1): p. 860.

38. Hinz, M. and C. Scheidereit, *The IkappaB kinase complex in NF-kappaB regulation and beyond.* EMBO Rep, 2014. **15**(1): p. 46-61.

39. Israel, A., *The IKK complex, a central regulator of NF-kappaB activation.* Cold Spring Harb Perspect Biol, 2010. **2**(3): p. a000158.

40. Ashall, L., et al., *Pulsatile Stimulation Determines Timing and Specificity of NF-kB – Dependent Transcription.* Science, 2009. **324**(April): p. 242-246.

41. Nelson, D.E., et al., *Oscillations in NF-kappaB signaling control the dynamics of gene expression.* Science, 2004. **306**(5696): p. 704-8.

42. Lee, R.E., et al., *Fold change of nuclear NF-kappaB determines TNF-induced transcription in single cells.* Mol Cell, 2014. **53**(6): p. 867-79.

43. Oeckinghaus, A. and S. Ghosh, *The NF-kappaB family of transcription factors and its regulation.* Cold Spring Harb Perspect Biol, 2009. **1**(4): p. a000034.

44. Cheong, R., et al., *Transient IkappaB kinase activity mediates temporal NF-kappaB dynamics in response to a wide range of tumor necrosis factor-alpha doses.* J Biol Chem, 2006. **281**(5): p. 2945-50.

45. Skaug, B., et al., *Direct, noncatalytic mechanism of IKK inhibition by A20.* Mol Cell, 2011. **44**(4): p. 559-71.

46. Mokashi, C.S., et al., *A System for Analog Control of Cell Culture Dynamics to Reveal Capabilities of Signaling Networks.* iScience, 2019. **19**: p. 586-596.

47. Tay, S., et al., *Single-cell NF-kappaB dynamics reveal digital activation and analogue information processing.* Nature, 2010. **466**(7303): p. 267-71.

48. Colombo, F., S. Zambrano, and A. Agresti, *NF-kappaB, the Importance of Being Dynamic: Role and Insights in Cancer.* Biomedicines, 2018. **6**(2).

49. Werner, S.L., D. Barken, and A. Hoffmann, *Stimulus specificity of gene expression programs determined by temporal control of IKK activity.* Science, 2005. **309**(5742): p. 1857-61.

50. Zambrano, S., et al., *NF-kappaB oscillations translate into functionally related patterns of gene expression.* Elife, 2016. **5**: p. e09100.

51. Selimkhanov, J., et al., *Systems biology. Accurate information transmission through dynamic biochemical signaling networks.* Science, 2014. **346**(6215): p. 1370-3.

52. Zhang, Q., et al., *NF-κB Dynamics Discriminate between TNF Doses in Single Cells.* Cell systems, 2017. **5**(6): p. 638-645.e5.

53. Tang, Y., et al., *Quantifying information accumulation encoded in the dynamics of biochemical signaling.* Nat Commun, 2021. **12**(1): p. 1272.

54. Cruz, J.A., et al., *A variable-gain stochastic pooling motif mediates information transfer from receptor assemblies into NF-kappaB.* Sci Adv, 2021. **7**(30).

55. Stringer, C., et al., *Cellpose: a generalist algorithm for cellular segmentation.* Nat Methods, 2021. **18**(1): p. 100-106.

56. Altschuler, S.J. and L.F. Wu, *Cellular heterogeneity: do differences make a difference?* Cell, 2010. **141**(4): p. 559-63.

57. Levchenko, A. and I. Nemenman, *Cellular noise and information transmission.* Curr Opin Biotechnol, 2014. **28**: p. 156-64.

58. Snijder, B. and L. Pelkmans, *Origins of regulated cell-to-cell variability.* Nat Rev Mol Cell Biol, 2011. **12**(2): p. 119-25.

59. Mazzarello, P., *A unifying concept: the history of cell theory.* Nat Cell Biol, 1999. **1**(1): p. E13-5.

60. Perrimon, N., C. Pitsouli, and B.Z. Shilo, *Signaling mechanisms controlling cell fate and embryonic patterning.* Cold Spring Harb Perspect Biol, 2012. **4**(8): p. a005975.

61. Downward, J., *The ins and outs of signalling.* Nature, 2001. **411**(6839): p. 759-62.

62. Sever, R. and J.S. Brugge, *Signal transduction in cancer.* Cold Spring Harb Perspect Med, 2015. **5**(4).

63. Aggarwal, B.B., et al., *Targeting cell signaling pathways for drug discovery: an old lock needs a new key.* J Cell Biochem, 2007. **102**(3): p. 580-92.

64. Eungdamrong, N.J. and R. Iyengar, *Modeling cell signaling networks.* Biol Cell, 2004. **96**(5): p. 355-62.

65. Gunawardena, J., *Signals and Systems: Towards a Systems Biology of Signal Transduction.* Proceedings of the IEEE, 2008. **96**(8): p. 1386-1397.

66. Klipp, E. and W. Liebermeister, *Mathematical modeling of intracellular signaling pathways.* BMC Neurosci, 2006. **7 Suppl 1**: p. S10.

67. Basak, S., M. Behar, and A. Hoffmann, *Lessons from mathematically modeling the NF-kappaB pathway.* Immunol Rev, 2012. **246**(1): p. 221-38.

68. Phair, R.D., *Mechanistic modeling confronts the complexity of molecular cell biology.* Mol Biol Cell, 2014. **25**(22): p. 3494-6.

69. Schmidt, B.J., J.A. Papin, and C.J. Musante, *Mechanistic systems modeling to guide drug discovery and development.* Drug Discov Today, 2013. **18**(3-4): p. 116-27.

70. Baker, R.E., et al., *Mechanistic models versus machine learning, a fight worth fighting for the biological community?* Biol Lett, 2018. **14**(5).

71. Peng, G.C.Y., et al., *Multiscale modeling meets machine learning: What can we learn?* Arch Comput Methods Eng, 2021. **28**(3): p. 1017-1037.

72. Chen, W.W., M. Niepel, and P.K. Sorger, *Classic and contemporary approaches to modeling biochemical reactions.* Genes Dev, 2010. **24**(17): p. 1861-75.

73. Gupta, S., et al. *Evaluation of Parallel Tempering to Accelerate Bayesian Parameter Estimation in Systems Biology*. in *2018 26th Euromicro International Conference on Parallel, Distributed and Network-based Processing (PDP)*. 2018.

74. Gabor, A. and J.R. Banga, *Robust and efficient parameter estimation in dynamic models of biological systems.* BMC Syst Biol, 2015. **9**: p. 74.

75. Williams, R.A., J. Timmis, and E.E. Qwarnstrom, *Computational Models of the NF-KB Signalling Pathway.* Computation, 2014. **2**(4): p. 131-158.

76. O'Dea, E.L., et al., *A homeostatic model of IkappaB metabolism to control constitutive NF-kappaB activity.* Mol Syst Biol, 2007. **3**: p. 111.

77. Lipniacki, T., et al., *Mathematical model of NF-kappaB regulatory module.* J Theor Biol, 2004. **228**(2): p. 195-215.

78. Lipniacki, T. and M. Kimmel, *Deterministic and stochastic models of NFkappaB pathway.* Cardiovasc Toxicol, 2007. **7**(4): p. 215-34.

79. Lipniacki, T., et al., *Single TNFalpha trimers mediating NF-kappaB activation: stochastic robustness of NF-kappaB signaling.* BMC Bioinformatics, 2007. **8**: p. 376.

80. Han, F., et al., *Dopamine D2 receptor modulates Wnt expression and control of cell proliferation.* Sci Rep, 2019. **9**(1): p. 16861.

81. Lee, P.J., et al., *A microfluidic system for dynamic yeast cell imaging.* Biotechniques, 2008. **44**(1): p. 91-5.

82. Gomez-Sjoberg, R., et al., *Versatile, fully automated, microfluidic cell culture system.* Anal Chem, 2007. **79**(22): p. 8557-63.

83. He, L., et al., *An automated programmable platform enabling multiplex dynamic stimuli delivery and cellular response monitoring for high-throughput suspension single-cell signaling studies.* Lab Chip, 2015. **15**(6): p. 1497-507.

84. Kim, S.J., et al., *Constant flow-driven microfluidic oscillator for different duty cycles.* Anal Chem, 2012. **84**(2): p. 1152-6.

85. Bennett, M.R., et al., *Metabolic gene regulation in a dynamically changing environment.* Nature, 2008. **454**(7208): p. 1119-22.

86. Hersen, P., et al., *Signal processing by the HOG MAP kinase pathway.* Proc Natl Acad Sci U S A, 2008. **105**(20): p. 7165-70.

87. Ryu, H., et al., *Integrated Platform for Monitoring Single-cell MAPK Kinetics in Computer-controlled Temporal Stimulations.* Sci Rep, 2018. **8**(1): p. 11126.

88. Ho, C.M., et al., *3D printed microfluidics for biological applications.* Lab Chip, 2015. **15**(18): p. 3627-37.

89. Brimmo, A., et al., *3D Printed Microfluidic Probes.* Sci Rep, 2018. **8**(1): p. 10995.

90. Hsieh, H.J., et al., *Shear-induced endothelial mechanotransduction: the interplay between reactive oxygen species (ROS) and nitric oxide (NO) and the pathophysiological implications.* J Biomed Sci, 2014. **21**: p. 3.

91. Nagel, T., et al., *Vascular endothelial cells respond to spatial gradients in fluid shear stress by enhanced activation of transcription factors.* Arterioscler Thromb Vasc Biol, 1999. **19**(8): p. 1825-34.

92. Mavrogiannis, N., et al., *Microfluidics made easy: A robust low-cost constant pressure flow controller for engineers and cell biologists.* Biomicrofluidics, 2016. **10**(3): p. 034107.

93. Fullerton, J.N. and D.W. Gilroy, *Resolution of inflammation: a new therapeutic frontier.* Nat Rev Drug Discov, 2016. **15**(8): p. 551-67.

94. Kumar, R., et al., *The dynamics of acute inflammation.* J Theor Biol, 2004. **230**(2): p. 145-55.

95. Medzhitov, R., *Origin and physiological roles of inflammation.* Nature, 2008. **454**(7203): p. 428-35.

96. Zhang, Q., et al., *NF-kappaB Dynamics Discriminate between TNF Doses in Single Cells.* Cell Syst, 2017. **5**(6): p. 638-645 e5.

97. Lee, R.E.C., et al., *NF- κ B signalling and cell fate decisions in response to a short pulse of tumour necrosis factor.* Nature Publishing Group, 2016(November): p. 1-12.

98. King, K.R., et al., *Microfluidic flow-encoded switching for parallel control of dynamic cellular microenvironments.* Lab Chip, 2008. **8**(1): p. 107-16.

99. Hansen, M.M.K., et al., *Cytoplasmic Amplification of Transcriptional Noise Generates Substantial Cell-to-Cell Variability.* Cell Syst, 2018. **7**(4): p. 384-397 e6.

100. Wong, V.C., et al., *NF-kappaB-Chromatin Interactions Drive Diverse Phenotypes by Modulating Transcriptional Noise.* Cell Rep, 2018. **22**(3): p. 585-599.

101. Lawrence, C.P. and S.C. Chow, *Suppression of human T cell proliferation by the caspase inhibitors, z-VAD-FMK and z-IETD-FMK is independent of their caspase inhibition properties.* Toxicol Appl Pharmacol, 2012. **265**(1): p. 103-12.

102. Toettcher, J.E., O.D. Weiner, and W.A. Lim, *Using optogenetics to interrogate the dynamic control of signal transmission by the Ras/Erk module.* Cell, 2013. **155**(6): p. 1422-34.

103. Tischer, D. and O.D. Weiner, *Illuminating cell signalling with optogenetic tools.* Nat Rev Mol Cell Biol, 2014. **15**(8): p. 551-8.

104. Smith, R.A. and C. Baglioni, *The active form of tumor necrosis factor is a trimer.* J Biol Chem, 1987. **262**(15): p. 6951-4.

105. Narhi, L.O. and T. Arakawa, *Dissociation of recombinant tumor necrosis factor-alpha studied by gel permeation chromatography.* Biochem Biophys Res Commun, 1987. **147**(2): p. 740-6.

106. Corti, A., et al., *Oligomeric tumour necrosis factor alpha slowly converts into inactive forms at bioactive levels.* Biochem J, 1992. **284 (Pt 3)**: p. 905-10.

107. Krippner-Heidenreich, A., et al., *Single-chain TNF, a TNF derivative with enhanced stability and antitumoral activity.* J Immunol, 2008. **180**(12): p. 8176-83.

108. Hausser, J., et al., *Central dogma rates and the trade-off between precision and economy in gene expression.* Nat Commun, 2019. **10**(1): p. 68.

109. Yan, X., et al., *Dynamics of Translation of Single mRNA Molecules In Vivo.* Cell, 2016. **165**(4): p. 976-89.

110. Gonskikh, Y. and N. Polacek, *Alterations of the translation apparatus during aging and stress response.* Mech Ageing Dev, 2017. **168**: p. 30-36.

111. Adamson, A., et al., *Signal transduction controls heterogeneous NF-kappaB dynamics and target gene expression through cytokine-specific refractory states.* Nat Commun, 2016. **7**: p. 12057.

112. DeFelice, M.M., et al., *NF-kappaB signaling dynamics is controlled by a dose-sensing autoregulatory loop.* Sci Signal, 2019. **12**(579).

113. Harris, J., et al., *Non-plasma bonding of PDMS for inexpensive fabrication of microfluidic devices.* J Vis Exp, 2007(9): p. 410.

114. Cheong, R., et al., *Information transduction capacity of noisy biochemical signaling networks.* Science, 2011. **334**(6054): p. 354-8.

115. Aggarwal, B.B., *Signalling pathways of the TNF superfamily: a double-edged sword.* Nat Rev Immunol, 2003. **3**(9): p. 745-56.

116. Lim, R., G. Barker, and M. Lappas, *TRADD, TRAF2, RIP1 and TAK1 are required for TNF-α-induced pro-labour mediators in human primary myometrial cells.* American Journal of Reproductive Immunology, 2017. **78**(1).

117. Ikeda, F., et al., *SHARPIN forms a linear ubiquitin ligase complex regulating NF-kappaB activity and apoptosis.* Nature, 2011. **471**(7340): p. 637-41.

118. Clague, M.J., S. Urbe, and D. Komander, *Breaking the chains: deubiquitylating enzyme specificity begets function.* Nat Rev Mol Cell Biol, 2019. **20**(6): p. 338-352.

119. Clark, K., S. Nanda, and P. Cohen, *Molecular control of the NEMO family of ubiquitin-binding proteins.* Nat Rev Mol Cell Biol, 2013. **14**(10): p. 673-85.

120. Haas, T.L., et al., *Recruitment of the linear ubiquitin chain assembly complex stabilizes the TNF-R1 signaling complex and is required for TNF-mediated gene induction.* Mol Cell, 2009. **36**(5): p. 831-44.

121. Ea, C.K., et al., *Activation of IKK by TNFalpha requires site-specific ubiquitination of RIP1 and polyubiquitin binding by NEMO.* Mol Cell, 2006. **22**(2): p. 245-57.

122. Scholefield, J., et al., *Super-resolution microscopy reveals a preformed NEMO lattice structure that is collapsed in incontinentia pigmenti.* Nat Commun, 2016. **7**: p. 12629.

123. Alon, U., *An introduction to systems biology : design principles of biological circuits*. Chapman & Hall/CRC mathematical and computational biology series. 2007, Boca Raton, FL: Chapman & Hall/CRC. xvi, 301 p., 4 p. of plates.

124. Pahl, H.L., *Activators and target genes of Rel/NF-kappaB transcription factors.* Oncogene, 1999. **18**(49): p. 6853-66.

125. MacEwan, D.J., *TNF ligands and receptors--a matter of life and death.* Br J Pharmacol, 2002. **135**(4): p. 855-75.

126. Neumann, D., et al., *The membrane form of the type II IL-1 receptor accounts for inhibitory function.* J Immunol, 2000. **165**(6): p. 3350-7.

127. Jupp, O.J., et al., *Type II tumour necrosis factor-alpha receptor (TNFR2) activates c-Jun N-terminal kinase (JNK) but not mitogen-activated protein kinase (MAPK) or p38 MAPK pathways.* Biochem J, 2001. **359**(Pt 3): p. 525-35.

128. Watanabe, N., et al., *Continuous internalization of tumor necrosis factor receptors in a human myosarcoma cell line.* J Biol Chem, 1988. **263**(21): p. 10262-6.

129. Lehmann, V. and W. Droge, *Demonstration of membrane receptors for human natural and recombinant 125I-labeled tumor necrosis factor on HeLa cell clones and their role in tumor cell sensitivity.* Eur J Biochem, 1986. **158**(1): p. 1-5.

130. Dower, S.K., et al., *Detection and characterization of high affinity plasma membrane receptors for human interleukin 1.* The Journal of Experimental Medicine, 1985. **162**(2): p. 501-515.

131. Karathanasis, C., et al., *Single-molecule imaging reveals the oligomeric state of functional TNFα-induced plasma membrane TNFR1 clusters in cells.* Science Signaling, 2020. **13**(614).

132. Kull, F.C., S. Jacobs, and P. Cuatrecasas, *Cellular receptor for 125I-labeled tumor necrosis factor: specific binding, affinity labeling, and relationship to sensitivity.* Proceedings of the National Academy of Sciences of the United States of America, 1985. **82**(17): p. 5756-5760.

133. Rubin, B.Y., et al., *High affinity binding of 125I-labeled human tumor necrosis factor (LuKII) to specific cell surface receptors.* The Journal of Experimental Medicine, 1985. **162**(3): p. 1099-1104.

134. Grell, M., et al., *The type 1 receptor (CD120a) is the high-affinity receptor for soluble tumor necrosis factor.* Proc Natl Acad Sci U S A, 1998. **95**(2): p. 570-5.

135. Hwang, B., et al., *Quantification of cellular NEMO content and its impact on NF-kappaB activation by genotoxic stress.* PLoS One, 2015. **10**(3): p. e0116374.

136. Wang, C., et al., *Real-Time Imaging of Translation on Single mRNA Transcripts in Live Cells.* Cell, 2016. **165**(4): p. 990-1001.

137. Werner, S.L., et al., *Encoding NF-kappaB temporal control in response to TNF: distinct roles for the negative regulators IkappaBalpha and A20.* Genes Dev, 2008. **22**(15): p. 2093-101.

138. Sumit, M., et al., *A Two-Pulse Cellular Stimulation Test Elucidates Variability and Mechanisms in Signaling Pathways.* Biophys J, 2019. **116**(5): p. 962-973.

139. McDonnell, M.D., *Information capacity of stochastic pooling networks is achieved by discrete inputs.* Phys Rev E Stat Nonlin Soft Matter Phys, 2009. **79**(4 Pt 1): p. 041107.

140. Savageau, M.A., *Biochemical systems analysis : a study of function and design in molecular biology*. 1976, Reading, Mass.: Addison-Wesley Pub. Co., Advanced Book Program. xvii, 379 p.

141. Serke, S., A. van Lessen, and D. Huhn, *Quantitative fluorescence flow cytometry: a comparison of the three techniques for direct and indirect immunofluorescence.* Cytometry, 1998. **33**(2): p. 179-87.

142. Bryl, E., et al., *Modulation of CD28 expression with anti-tumor necrosis factor alpha therapy in rheumatoid arthritis.* Arthritis Rheum, 2005. **52**(10): p. 2996-3003.

143. Bebes, A., et al., *Interleukin-1 receptors are differentially expressed in normal and psoriatic T cells.* Mediators of inflammation, 2014. **2014**: p. 472625-472625.

144. Lamprecht, M.R., D.M. Sabatini, and A.E. Carpenter, *CellProfiler: free, versatile software for automated biological image analysis.* Biotechniques, 2007. **42**(1): p. 71-5.

145. Ran, F.A., et al., *Genome engineering using the CRISPR-Cas9 system.* Nat Protoc, 2013. **8**(11): p. 2281-2308.

146. Kowalczyk, G.J., et al., *dNEMO: a tool for quantification of mRNA and punctate structures in time-lapse images of single cells.* Bioinformatics, 2020.

147. Jaqaman, K., et al., *Robust single-particle tracking in live-cell time-lapse sequences.* Nat Methods, 2008. **5**(8): p. 695-702.

148. Ferrell, J.E., Jr., *Perfect and Near-Perfect Adaptation in Cell Signaling.* Cell Syst, 2016. **2**(2): p. 62-7.

149. Khammash, M.H., *Perfect adaptation in biology.* Cell Syst, 2021. **12**(6): p. 509-521.

150. Hacker, H. and M. Karin, *Regulation and function of IKK and IKK-related kinases.* Sci STKE, 2006. **2006**(357): p. re13.

151. Delhase, M., et al., *Positive and negative regulation of IkappaB kinase activity through IKKbeta subunit phosphorylation.* Science, 1999. **284**(5412): p. 309-13.

152. Basak, S., et al., *A fourth IkappaB protein within the NF-kappaB signaling module.* Cell, 2007. **128**(2): p. 369-81.

153. Mitchell, S., J. Vargas, and A. Hoffmann, *Signaling via the NFkappaB system.* Wiley Interdiscip Rev Syst Biol Med, 2016. **8**(3): p. 227-41.

154. Gupta, S., R.E.C. Lee, and J.R. Faeder, *Parallel Tempering with Lasso for model reduction in systems biology.* PLoS Comput Biol, 2020. **16**(3): p. e1007669.

155. Gasse, P., et al., *IL-1R1/MyD88 signaling and the inflammasome are essential in pulmonary inflammation and fibrosis in mice.* J Clin Invest, 2007. **117**(12): p. 3786-99.

156. Wesche, H., et al., *MyD88: an adapter that recruits IRAK to the IL-1 receptor complex.* Immunity, 1997. **7**(6): p. 837-47.

157. Mizel, S.B., et al., *The interleukin 1 receptor. Dynamics of interleukin 1 binding and internalization in T cells and fibroblasts.* J Immunol, 1987. **138**(9): p. 2906-12.

158. Dinarello, C.A., *Biology of interleukin 1.* FASEB J, 1988. **2**(2): p. 108-15.

159. Arend, W.P., et al., *Binding of IL-1 alpha, IL-1 beta, and IL-1 receptor antagonist by soluble IL-1 receptors and levels of soluble IL-1 receptors in synovial fluids.* J Immunol, 1994. **153**(10): p. 4766-74.

160. Lee, M.J., et al., *Sequential application of anticancer drugs enhances cell death by rewiring apoptotic signaling networks.* Cell, 2012. **149**(4): p. 780-94.

161. Xia, X., et al., *Cell-to-cell variability in cell death: can systems biology help us make sense of it all?* Cell death & disease, 2014. **5**(5): p. e1261-e1261.

162. Berg, H.C. and E.M. Purcell, *Physics of chemoreception.* Biophys J, 1977. **20**(2): p. 193-219.

163. McDonnell, M.D. and D. Abbott, *What is stochastic resonance? Definitions, misconceptions, debates, and its relevance to biology.* PLoS Comput Biol, 2009. **5**(5): p. e1000348.